Klinik und Poliklinik für Unfallchirurgie
Fakultät für Medizin

Tissue engineering of the tendon/ligament-to-bone transition

Sònia Font Tellado

Vollständiger Abdruck der von der Fakultät für Medizin der Technischen Universität München zur Erlangung des akademischen Grades eines Doktor der Naturwissenschaften (Dr. rer. nat.) genehmigten Dissertation.

ABSTRACT

The enthesis is a highly specialized interface tissue at the attachment sites of tendons/ligaments to bones. During musculoskeletal motion, a smooth transfer of mechanical stresses between tendons/ligaments (soft tissue) and bones (hard tissue) is possible due to the mechanical and structural gradients that compose the enthesis. Despite that, current surgical treatments for the repair of ruptured tendons and ligaments do not promote enthesis regeneration. This results in poor soft-to-hard tissue integration and high rupture recurrence rates, compromising long term clinical outcome.

The present work proposes a novel strategy for enthesis regeneration based on the development of integrated tissue-engineered tendon/ligament-to-bone constructs (scaffolds). The constructs are composed of a region of anisotropic porosity (mimicking the aligned structure of the tendon/ligament) and a region of isotropic porosity (mimicking the non-aligned structure of bone/cartilage). The impact of fabrication parameters on the structural and mechanical properties of the constructs were evaluated and optimized to maximize pore sizes, mechanical stability, integration between the anisotropic and isotropic parts and biocompatibility.

The tendon/ligament-to-bone constructs were functionalized with heparin to increase their ability to retain and deliver transforming growth factor beta 2 (TGF-β2) and growth/differentiation factor 5 (GDF5). The impact of structural features (pore morphology and alignment) and biological cues (growth factors) on cell behavior was evaluated *in vitro* with human primary adipose-derived mesenchymal stem cells (AdMSCs). Pore alignment influenced the cytoskeletal alignment and gene expression of AdMSCs, resulting in different gene expression patterns in the anisotropic and isotropic regions. In addition, pore alignment influenced the effect of growth factors on cell gene and protein expression. Synergistical effects between growth factors and pore alignment were identified, which selectively promoted the expression of tendon/ligament markers in the anisotropic part of the constructs, cartilage markers in the isotropic part and enthesis markers at the transition.

Altogether, the data presented in this study improves current knowledge on how structural and biochemical cues provided by scaffolds can be tailored to induce specific multi-lineage differentiation of AdMSCs for tendon/ligament-to-bone regeneration.

ZUSAMMENFASSUNG

Bei der Enthese handelt sich um ein hochspezialisiertes Gewebe am Übergang zwischen Sehnen/Bändern zu Knochen. Während der muskuloskelettalen Bewegung ist ein gleichmäßiger Transfer von mechanischen Stressimpulsen zwischen Sehnen/Bändern (Weichgewebe) zu Knochen (Hartgewebe) möglich, weil die Enthese aus bestimmten mechanischen und strukturellen Komponenten besteht. Dennoch unterstützen die gegenwärtig durchführbaren chirurgischen Behandlungsformen für die Wiederherstellung von gerissenen Bändern und Sehnen nicht die Heilung der Enthese. Das führt zu einer schlechten Integration der Übergänge zwischen harten und weichen Geweben und somit zu einer hohen Rate an erneuten Rupturen, die letztendlich das langfristige klinische Outcome beeinträchtigt.

Die vorliegende Arbeit untersucht eine neuartige Strategie für die Regeneration der Enthese auf der Grundlage der Entwicklung von integrierten Sehnen/Bänder zu Knochen Konstrukten (Scaffolds), die mittels Tissue Engineering hergestellt werden. Die Konstrukte bestehen aus einem Teil mit anisotroper Porosität (der die parallel angeordnete Porenstruktur der Sehnen/Bänder imitiert) und einem Teil mit isotroper Porosität (der die zufällig angeordnete Porenstruktur der Knochen/Knorpel imitiert). Der Einfluss der Herstellungsparameter auf die strukturellen und mechanischen Eigenschaften der Konstrukte wurde untersucht und optimiert, um die Porengrößen, die mechanische Stabilität und die Integration zwischen den anisotropen und isotropen Teilen und deren Biokompatibilität zu maximieren.

Die Sehnen/Bänder zu Knochen Konstrukte wurden mit Heparin funktionalisiert, um ihre Fähigkeit zu verbessern, Transforming Growth Factor beta 2 (TGF-β2) und Growth/Differentiation Factor 5 (GDF5) zu speichern und abzugeben. Der Einfluss der strukturellen (Morphologie und Ausrichtung der Poren) und biologischen Eigenschaften (Wachstumsfaktoren) auf das Verhalten der Zellen wurde *in vitro* mittels humaner primärer, mesenchymaler Stammzellen untersucht, die aus dem Fettgewebe gewonnen wurden (AdMSCs). Die Ausrichtung der Poren beeinflusste die zytoskelettale Ausrichtung und die Genexpression der AdMSCs, was unterschiedliche Genexpressionsmuster in den anisotropen und isotropen Teilen zur Folge hatte. Zusätzlich beeinflusste die Ausrichtung der Poren den Effekt der Wachstumsfaktoren auf die Expression von Genen und Proteinen in den Zellen. Wir fanden auch synergistische Effekte zwischen Wachstumsfaktoren und der Ausrichtung der Poren, die gezielt die Expression von Sehnen/Bänder Markern im anisotropen Teil des Konstrukts, von Knorpelmarkern im isotropen Teil und von Enthesemarkern im Übergangsbereich steigerten.

Insgesamt erweitern die durch diese Studie gewonnenen Erkenntnisse das Wissen, wie strukturelle und biochemische Eigenschaften von Scaffolds so maßgeschneidert werden können, dass eine spezifische multipotente Differenzierung von AdMSCs für die Regeneration des Sehnen/Bänder zu Knochen Übergangs erreicht wird.

TABLE OF CONTENTS

1. ABBREVIATIONS

µCT – Micro-computed Tomography

ACL – Anterior Cruciate Ligament

AdMSCs – Adipose-derived Mesenchymal Stem Cells

ALP – Alkaline Phosphatase

ATR – Attenuated Total Reflectance

BMP – Bone Morphogenetic Protein

BMSCs – Bone Marrow-derived Mesenchymal Stem Cells

BSA – Bovine Serum Albumin

CTGF – Connective Tissue Growth Factor

DAPI – 4′,6-diamidino-2-phenylindole

DMEM – Dulbecco's Modified Eagle Medium

ECM – Extracellular Matrix

EDC – 1-ethyl-3-(3-dimethylaminopropyl)carbodiimide hydrochloride

EDTA – Ethylenediaminetetraacetic Acid

FCS – Fetal Calf Serum

FDA – Food and Drug Administration agency

FESEM - Field-Emission Scanning Electron Microscopy

FGF – Fibroblast Growth Factor

FTIR – Fourier Transform Infrared Spectroscopy

GAG – Glycosaminoglycan

GDF – Growth/Differentiation Factor

Gli1 – Glioma-Associated Oncogene homolog 1

Ihh – Indian Hedgehog

LDH – Lactate Dehydrogenase

MeOH – Methanol

MES – 2-(N-morpholino)ethanesulfonic acid

MF – Mineralized Fibrocartilage

MSC – Mesenchymal Stem Cell

MTT – 3-(4,5-Dimethylthiazol-2-yl)-2,5-diphenyltetrazoliumbromide

NF – Non-mineralized Fibrocartilage

NHS - N-hydroxysuccinimide

OD – Optical Density

PI – Propidium Iodide

P/S – Penicillin/Streptomycin

PBS – Phosphate Buffered Saline

PCL – Poly-ε-Caprolactone

PEG – Polyethylene Glycol

PLA – Polylactic Acid

PLGA – polylactic-co-glycolic acid

PP – Polypropylene

PTHrP – Parathyroid Hormone-related Protein

qPCR – Quantitative Polymerase Chain Reaction

RT– Room Temperature

Scx – Scleraxis

SEM – Standard Error of the Mean

Sox9 – SRY(Sex determining Region Y)-box 9

TGF-β – Transforming Growth Factor beta

VEGF – Vascular Endothelial Growth Factor

2. INTRODUCTION

2.1 The tendon/ligament-to-bone interface (enthesis)

Tendon and ligament ruptures are very common in modern society and are of high socioeconomic importance (Rehmann et al. 2016; Leong, Petrigliano, and McAllister 2014). Two clinically relevant examples are the rotator cuff tendon in the shoulder and the anterior cruciate ligament (ACL) in the knee. Alone, ACL ruptures occur in approximately 200,000 people each year in the United States and have high associated treatment costs (Leong, Petrigliano, and McAllister 2014; Paschos and Howell 2016; Satora et al. 2017). Because of the poor self-regeneration capacity of tendons and ligaments, full function can only be restored with suitable replacement (He et al. 2012; Nguyen et al. 2013; Leong, Petrigliano, and McAllister 2014).

Current surgical treatment options for the repair of a ruptured tendon or ligament include autograft or allograft transplantation (Leong, Petrigliano, and McAllister 2014; Satora et al. 2017). In this procedure, the ruptured tendon or ligament is removed and replaced by a tendon graft. The graft is inserted in small drills performed in the bones and mechanically fixed. However, this type of treatment has several associated problems, such as donor site morbidity and, in the case of ligaments, replacement with tendon tissue of suboptimal mechanical properties (He et al. 2012; Leong, Petrigliano, and McAllister 2014). In addition, a main problem is the poor integration between the tendon graft (soft tissue) and the bone (hard tissue) (Shaw and Benjamin 2007). Tendons and ligaments are soft, compliant tissues (tensile modulus ~0.45 GPa) (Rossetti et al. 2017; Wren et al. 2001), which can resist tensile forces, while bone is a stiff, hard tissue (tensile modulus ~20 GPa) (Rossetti et al. 2017; Zelzer et al. 2014) optimized to withstand compression. Suboptimal soft-to-hard tissue integration results in the accumulation of high mechanical stresses at the points of fixation of the graft to the bone (Font Tellado, Balmayor, and Van Griensven 2015; He et al. 2012). As a consequence, there is an increase in the risk of rupture recurrence, chronic pain and decreased muscle strength (Leong, Petrigliano, and McAllister 2014; He et al. 2012). Rupture recurrence rates range between 20 to 94% depending on the severity of the injury (Liu et al. 2011).

Healthy tendons and ligaments attach to bones through a highly specialized tissue interface, the enthesis (Font Tellado, Balmayor, and Van Griensven 2015; Moffat et al. 2009). High mechanical stresses accumulate at the enthesis due to the stiffness mismatch between tendon/ligament and bone tissues. Despite that, ruptures or fractures are more prone to happen at the tendon/ligament

or bone compared to the enthesis (Benjamin et al. 2006; Rossetti et al. 2017). This can be explained by the presence of gradients in structural composition along the enthesis. This compositional gradients result in a gradual change in mechanical properties that increases interface strength and reduces stress concentrations, allowing for a smooth transfer of mechanical stresses from soft to hard tissues (Font Tellado, Balmayor, and Van Griensven 2015; Shaw and Benjamin 2007).

Despite the importance of the enthesis for proper musculoskeletal motion, surgical fixation of soft tissue grafts to bone does not promote enthesis regeneration. Indeed, the enthesis is often not regenerated after surgical fixation of tendon grafts to bone. Instead, a fibrovascular tissue of inferior mechanical properties forms at the attachment site. Promoting enthesis regeneration in the repair of tendon/ligament injuries would improve soft-to-hard tissue integration, tissue functionality and long term clinical outcome. Thus, there is a need to develop new strategies for enthesis regeneration.

2.1.1 Enthesis structure and composition

Histologically, two types of entheses can be distinguished: fibrous and fibrocartilaginous. The present work focuses on fibrocartilaginous entheses. Fibrocartilaginous entheses are found in the rotator cuff and the ACL, and thus are clinically more relevant (Yang and Temenoff 2009). Fibrocartilaginous entheses consist of four different regions: tendon/ligament, non-mineralized fibrocartilage (NF), mineralized fibrocartilage (MF) and bone (figure 1). Extracellular matrix (ECM) composition, cell type and mechanical properties change gradually along the enthesis. Tendons and ligaments consist of highly aligned collagen fibers, predominantly type I, and small amounts of the proteoglycan decorin. Tendons/ligaments are populated by elongated cells called fibroblasts. The NF is composed of high levels of collagen type II and is populated by round cells called fibrochondrocytes. In addition, the NF is rich in proteoglycans, mainly aggrecan, and contains collagen type III. The MF is composed of mineralized collagen type II and contains significant levels of collagen type X and aggrecan. In this region, fibrochondrocytes become hypertrophic. The MF merges into bone tissue, which is composed of non-aligned collagen I fibers and high mineral content, mainly hydroxyapatite. Bone tissue is populated by osteoblasts, osteocytes and osteoclasts (Font Tellado, Balmayor, and Van Griensven 2015; Genin et al. 2009).

Importantly, the different regions of fibrocartilaginous entheses are compositionally distinct but structurally continuous. In fact, collagen molecule alignment increases gradually towards the

tendon/ligament, whereas mineral content increases gradually towards the bone (Genin et al. 2009). These structural and ECM composition gradients allow for a gradual change of mechanical properties along the enthesis and facilitate the transfer of mechanical stresses from soft to hard tissue. Thus, the structure of the enthesis is essential for its function (Shaw and Benjamin 2007; Genin et al. 2009; Font Tellado, Balmayor, and Van Griensven 2015). This close structure-function relationship highlights the importance to preserve native structural features when aiming to regenerate tissues.
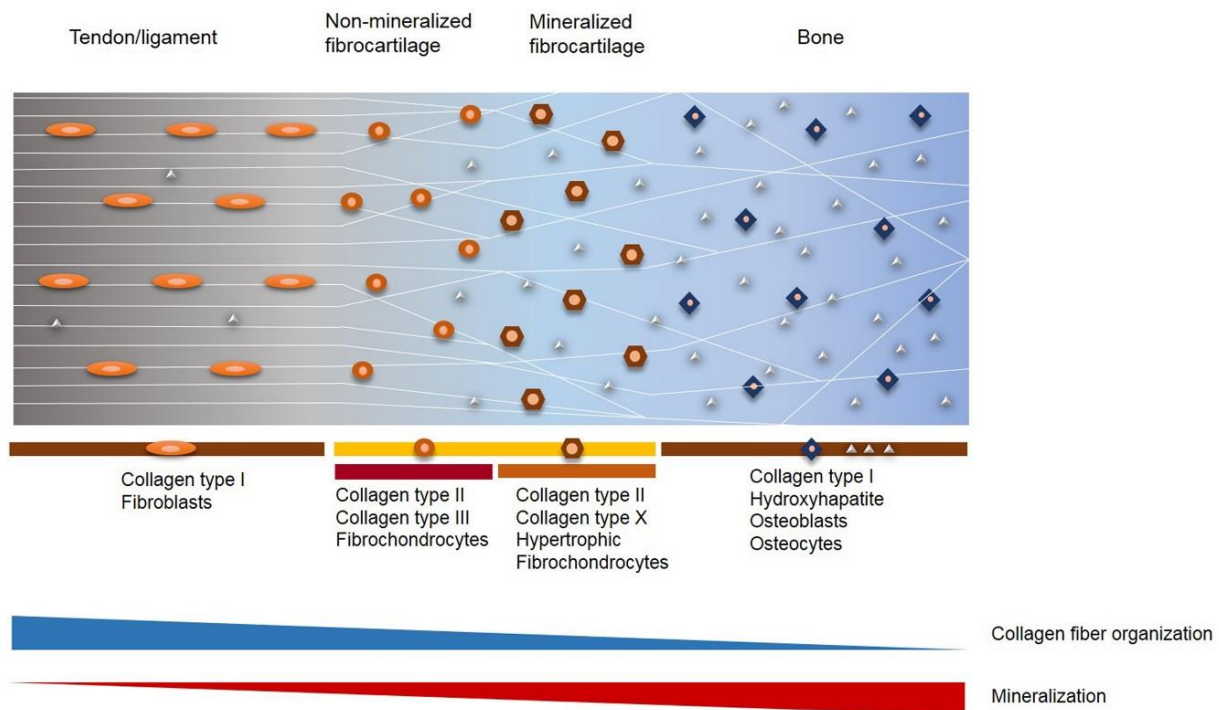
Figure 1. Schematic representation of fibrocartilaginous tendon/ligament-to-bone interfaces
Fibrocartilaginous entheses consist of four regions: tendon/ligament, non-mineralized fibrocartilage, mineralized fibrocartilage and bone. Each region is composed of different extracellular matrix molecules and cell types. Of note, there are two opposite structural gradients along the insertion: a gradient in collagen molecule alignment which increases towards the tendon/ligament and a gradient in mineral content which increases towards the bone. Figure from (Font Tellado, Balmayor, and Van Griensven 2015)

2.1.2 Enthesis development

The mechanisms driving the development of complex tissue interfaces such as the enthesis are still poorly understood (Zelzer et al. 2014). According to recent studies in mice, enthesis development happens in close coordination with tendon/ligament and cartilage development, and

follows similar patterns to the growth plate. Indeed, the similarity in tissue composition between fibrocartilage and articular cartilage reminds the enthesis of an arrested growth plate (Schwartz, Long, and Thomopoulos 2015).The formation of the tendon/ligament-to-bone attachment unit starts during embryonic development and finishes postnatally. It has been proposed that enthesis development happens in a modular fashion and starts with the specification of a pool of enthesis progenitors (Blitz et al. 2013; Blitz et al. 2009). This cell population is located between tendon/ligament and cartilage progenitors and expresses scleraxis (Scx), SRY(sex-determining Region Y)-box 9 (Sox9), growth/differentiation factor 5 (GDF5) and Glioma-Associated Oncogene homolog 1 (Gli1) (Blitz et al. 2013; Dyment et al. 2015; Sugimoto et al. 2013). Scx is a basic helix-loop-helix transcription factor that is expressed in tendon/ligament tissues throughout development. Sox9 is considered the master transcription factor for chondrogenesis and is one of the first upregulated markers at the starting of chondrogenic differentiation. Interestingly, the initial pool of scx+/sox9+ progenitors decreases in size as development proceeds and cells differentiate into scx+ ligament/tendon fibroblasts or sox9+ chondrocytes (Blitz et al. 2013; Sugimoto et al. 2013) (figure 2).
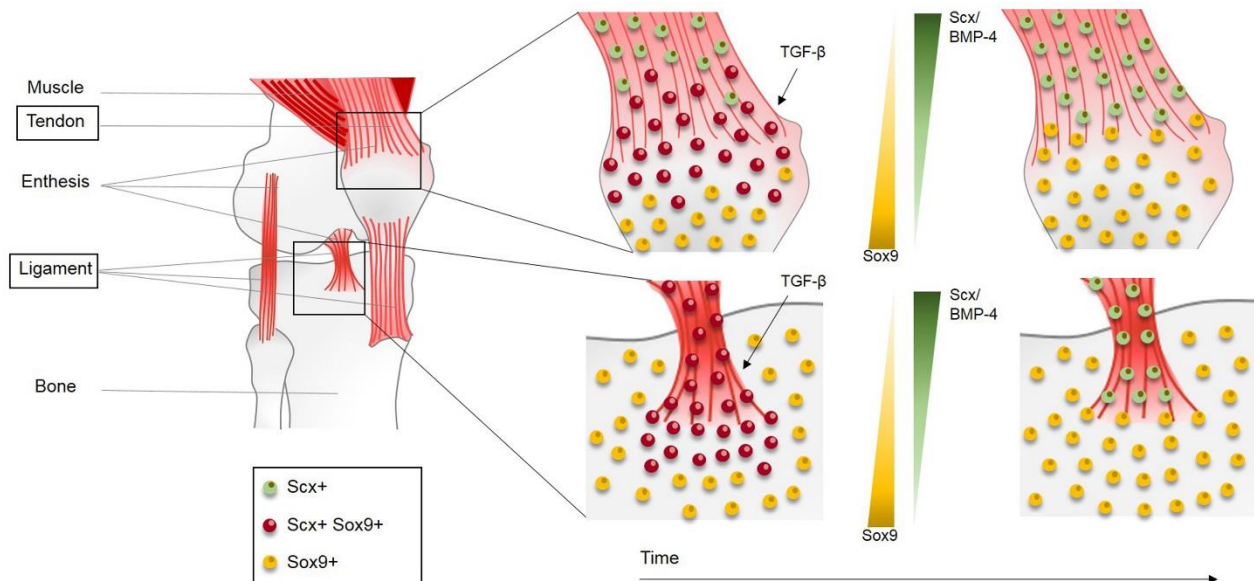
Figure 2. Role of transforming growth factor beta II (TGF-βII) receptor, bone morphogenetic protein 4 (BMP4) and scx+/SRY(sex-determining region Y)-box 9 (sox9)+ fibrochondrocyte progenitors on enthesis development. Progenitor cells that give rise to fibrochondrocytes express scx and sox9. As development proceeds, the population of scx+/sox9+ progenitors reduces in size as cells differentiate into scx+ tenocytes/ligamentocytes or sox9+ chondrocytes. It has been proposed that TGF-βII receptor signaling is necessary for progenitor cell specification, while BMP4/scx signaling regulates progenitor cell differentiation. Figure from (Font Tellado, Balmayor, and Van Griensven 2015)

Dyment et al. (2015) proposed a spatiotemporal sequence of events happening from the specification of enthesis progenitors until enthesis maturation. Enthesis progenitor cells proliferate and expand in columns, similar to chondrocytes of the growth plate, and contribute to enthesis growth. These cells start to synthesize a collagen I template that attaches to primary cartilage. As progenitors mature to fibrochondrocytes, they start producing proteoglycans and expressing collagen type II. The most mature cells located closer to primary cartilage start expressing collagen X and alkaline phosphatase (ALP). Finally, the onset of fibrocartilage mineralization happens postnatally and coincides with the point of formation of the secondary ossification center in the growth plate. Gli1 expression in fibrochondrocytes indicates responsiveness to hedgehog signaling, particularly Indian hedgehog (Ihh) and parathyroid hormone-related protein (PTHrP) (Dyment et al. 2015; Schwartz, Long, and Thomopoulos 2015; Schwartz, Galatz, and Thomopoulos 2017). In the growth plate, chondrocyte hypertrophy and mineralization is regulated by an Ihh/PTHrP negative feedback loop (van Donkelaar and Huiskes 2007). The detection of Ihh and PTHrP at the enthesis suggests that Ihh/PTHrP could induce appositional fibrocartilage mineralization in a similar manner (Dyment et al. 2015; Schwartz, Galatz, and Thomopoulos 2017). Interestingly, it has been suggested that the start of mineralization in response to hedgehog signaling is triggered by mechanical stimuli (Schwartz et al. 2013; Schwartz, Long, and Thomopoulos 2015; Thomopoulos et al. 2007). Schwartz et al. (2013) showed that muscular contraction is necessary for postnatal interface maturation and mineralization, but not for the proliferation and differentiation of enthesis progenitor cells. These data suggest that biochemical signals are important for the specification and expansion of the tendon/ligament-to-bone attachment unit (embryonically), while biophysical/mechanical signals are necessary for its maturation (postnatally). However, the specific mechanisms regulating the interplay between Ihh/PTHrP, mechanical load and enthesis mineralization are still unclear.

Although mouse models have improved current understanding on the cellular origin of fibrochondrocytes, less is known about the driving mechanisms behind their specification and differentiation. It has been proposed that growth factors from the transforming growth factor β (TGF-β) family play important roles (Zelzer et al. 2014; Blitz et al. 2009). TGF-β family members (including bone morphogenetic proteins, BMPs) regulate multiple stages of musculoskeletal development in tendon/ligament, cartilage and bone tissues. The specific roles of TGF-β growth factors on musculoskeletal development are difficult to determine because of their redundancy, interplay between multiple factors and the influence of the cellular microenvironment. However, studies in mice embryos suggest that TGF-β receptor II signaling regulates the specification of enthesis progenitors, while BMP4 controls their differentiation (Blitz et al. 2009) (figure 2). BMP4

signaling has been shown to originate from scx+ cells in the tendon, suggesting that BMP4 is a key mediator of tendon-specific signaling for enthesis development (Blitz et al. 2009). Other BMPs and members of the fibroblast growth factor (FGF) family have been also suggested to play key roles. It is likely that a coordinated action of multiple factors and cellular crosstalk is necessary for the development of complex tissues such as the tendon/ligament-to-bone attachment.

2.1.3 Mechanical properties of the enthesis

Tissue stiffness changes along the enthesis from ~0.45 GPa in the tendon/ligament to ~20 GPa in the bone, nearly two orders of magnitude of stiffness mismatch (Genin et al. 2009). Surprisingly, recent studies have revealed that the enthesis is more compliant (less stiff) than both tendon/ligament and bone tissues (Rossetti et al. 2017). This can be explained by the microstructure of the enthesis. The main factors determining tissue stiffness at the tendon/ligament-to-bone insertion are collagen fiber alignment and mineral content at the micro scale. As described in section 2.1.1, mineral content increases gradually and continuously from the tendon/ligament towards the bone, while collagen molecule alignment increases gradually towards the tendon/ligament. At the enthesis, collagen fibers are less aligned compared to the tendon/ligament. Decrease in collagen molecule alignment results in a decrease of stiffness (Genin et al. 2009). On the other hand, mineral content at the insertion is greater than in the tendon/ligament. However, an increase in stiffness due to mineral content depends on the interconnectivity between mineral particles. Only when the amount of mineral particles in collagen fibers is enough to create contact between the particles, stresses can be transferred through the mineral phase (Genin et al. 2009). Thus, in regions of low mineralization at the enthesis, stiffness is mostly regulated by the degree of collagen molecule alignment. Hence, the region is more compliant compared to highly aligned tendon/ligament. On the other hand, as mineral content increases along the insertion, mineral particles act like an interconnected network. When this mineralization threshold has been reached, tissue stiffness is mainly dominated by mineralization (Genin et al. 2009). Thus, the opposite gradients in mineral content and collagen alignment at the enthesis result in a gradual increase in stiffness along the transition and towards the bone region.

A compliant insertion site may seem more likely to rupture due to the greater mismatch in tissue stiffness and thus higher accumulation of mechanical stresses. However, stress concentrations do not only depend on tissue stiffness, but also on other material properties such as Poisson ratios and shear moduli. Indeed, mathematical models of the rotator cuff insertion suggest that a

compliant attachment can lead to stress reductions when assuming orthotropy and graded properties of the tendon (Rossetti et al. 2017).

2.2 Strategies to engineer the tendon/ligament-to-bone interface

Enthesis regeneration is of clinical significance for soft tissue repair given the importance of preserving its native structure to ensure tissue functionality (Benjamin et al. 2006; Font Tellado, Balmayor, and Van Griensven 2015; Shaw and Benjamin 2007). Tissue engineering is an attractive strategy for enthesis regeneration. Tissue engineering uses biocompatible materials (scaffolds) to provide mechanical support and to actively promote tissue regeneration. Scaffolds are often used in combination with cells and/or biological cues, such as growth factors. In the last years, tissue engineering has made an important progress in developing new approaches for bone, cartilage and tendon/ligament regeneration. However, engineering of complex tissue interfaces such as the enthesis remains a challenge (Moffat et al. 2009). Because of the problems associated with the fixation of soft grafts to hard tissue, new treatment strategies may benefit from the development of integrated tendon/ligament-to-bone constructs that replicate native tissue features (Moffat et al. 2008; Shaw and Benjamin 2007; Smith et al. 2012). It is likely that tissue engineering strategies will require a combination of biophysical, biochemical and/or mechanical cues to replicate the structural and cellular heterogeneity of the native enthesis (Moffat et al. 2009; Font Tellado, Balmayor, and Van Griensven 2015). The next sections will describe important parameters for enthesis tissue engineering including biomaterial properties, scaffold design, cell source and biochemical cues.

2.2.1 Biomaterials and scaffolds

A scaffold is an engineered replacement of a tissue's ECM that supports mechanical loads, facilitates cell adhesion and proliferation, and guides new tissue formation. Scaffolds are fabricated using biomaterials and can be composed of a single type of biomaterial or a composite of different biomaterials.

Scaffold composition, structure, biochemical and mechanical properties are influenced by the type of biomaterial and the method used for scaffold fabrication. Biomaterial choice is mainly influenced by the needs and characteristics of the tissue to be regenerated. In general, biomaterials for musculoskeletal tissue engineering should be biocompatible, biodegradable, facilitate cell

attachment and proliferation and be able to sustain mechanical loads (Dhandayuthapani et al. 2011). A wide variety of biomaterials have been used for musculoskeletal tissue engineering purposes, including artificial polymers such as poly-ε-caprolactone (PCL), polylactic acid (PLA) and derivatives (Poh et al. 2016; Mohammadkhah et al. 2015; Baykan et al. 2014; Lou et al. 2014; Xie et al. 2015), natural polymers such as collagen, silk fibroin, hyaluronic acid and chitosan (Park et al. 2016; Teuschl et al. 2016; Li et al. 2016; Foss et al. 2013; Islam et al. 2016; Bi et al. 2015; Kane et al. 2015; Foss, Migliaresi, and Motta 2013; Malafaya et al. 2005), and minerals such as calcium phosphates and bioactive glasses (Mohammadkhah et al. 2015; Lu et al. 2014; Poh et al. 2016; Poh et al. 2013). In addition, different scaffold formats can be produced from a same biomaterial depending on the fabrication method, including films, gels, fibers and porous scaffolds. Thus, a wide range of scaffold features can be tuned depending on biomaterial selection and fabrication parameters.

2.2.1.1 Silk fibroin

In the present work, silk fibroin was the biomaterial of choice for scaffold fabrication. Silk fibroin is an attractive biomaterial for tendon/ligament-to-bone tissue engineering because of its excellent biocompatibility, slow proteolytic degradation and mechanical properties similar to human ligament (Li et al. 2016; Vepari and Kaplan 2007). Silk fibroin has been used for decades as a suturing material and is approved by the Food and Drug Administration agency (FDA) for clinical use (Augst et al. 2008). Silk-based biomaterials have been proposed for the regeneration of ligament (Fan et al. 2009; Teuschl et al. 2016), cartilage (Foss et al. 2013) and musculoskeletal interfaces (Li et al. 2016; Ding et al. 2014; Li et al. 2015; He et al. 2012) in previous studies. The most commonly used type of silk fibroin is produced by *Bombyx mori* silkworms. Native *Bombyx mori* silk fibers are composed of two proteins: fibroin light chain (~26 kDa) and fibroin heavy chain (~390 kDa), which are present in a 1:1 ratio and linked by a disulfide bond (Vepari and Kaplan 2007). Fibroins are coated by hydrophilic proteins called sericins. Sericins are known to elicit immunogenic reactions but can be easily removed by boiling silk fibers in alkaline solutions (degumming) (Teuschl, van Griensven, and Redl 2014). After degumming, silk fibroin can be processed in mild, aqueous conditions to produce biomaterials in a variety of formats (Rockwood et al. 2011; Vepari and Kaplan 2007). In most cases (except after gelation), fibroin processed for scaffold fabrication in aqueous solution has a random coil structure (silk I), which is water soluble. Thus, fabrication of fibroin materials commonly involves a post-treatment with heat or methanol to induce a conformational change to the water insoluble (silk II) protein conformation, composed

mainly of β-sheets (Vepari and Kaplan 2007). Fibroin concentration in solution, scaffold fabrication method and post-treatment determine the structural and mechanical characteristics of scaffolds and can be adjusted to meet target tissue needs (Rockwood et al. 2011).

2.2.1.2 *Scaffold design*

Scaffolds for interface tissue engineering should be designed to mimic native structural and mechanical features to support tissue functionality. Stratified scaffolds consisting of different phases may better recapitulate the structural and compositional heterogeneity of native interfaces (Font Tellado, Balmayor, and Van Griensven 2015; Lu and Thomopoulos 2013; Spalazzi, Doty, et al. 2006; Soo Kim et al. 2014). However, the different phases should be interconnected and integrated with each other to support the deposition of compositionally distinct yet structurally integrated tissue regions (Lu and Thomopoulos 2013). Because of the close structure-function relationship in native interfaces, regeneration of complex tissues such as the enthesis poses significant challenges for scaffold design.

The gradients in collagen molecule alignment and mineral content present at the native enthesis are key for its functionality. Thus, scaffolds for enthesis tissue engineering should aim at replicating these features (Spalazzi, Doty, et al. 2006; Font Tellado et al. 2017). In the present work, porous scaffolds fabricated with silk fibroin were designed to replicate the change in collagen molecule alignment of the native enthesis. Biphasic scaffolds were designed to have aligned (anisotropic) pores in the tendon/ligament-like region and non-aligned (isotropic) pores in the cartilage/bone-like region. The anisotropic and isotropic regions were expected to integrate with each other in a transition area (enthesis-like) with a gradual change in pore alignment.

In addition, structural features of scaffolds also define the microenvironment to which cells are exposed. Structural parameters such as scaffold porosity and pore size determine nutrient and oxygen diffusion, cell density, cell-material and cell-cell interactions, and thus have a high impact on cell behavior (Oh et al. 2010). Surface topographical features have been shown to significantly affect cell attachment, proliferation, gene expression and protein secretion, a phenomenon known as contact guidance (Font Tellado et al. 2017; Bettinger, Langer, and Borenstein 2009; Mozdzen et al. 2016; Islam et al. 2016; Criscenti et al. 2016). For those reasons, scaffold designs should take into account both the characteristics of native tissues and the effects of structural parameters at the cellular level.

In addition to scaffold structure and topography, control over the spatial localization of cell populations and biologic factors is another key design parameter to be considered (Lu and Thomopoulos 2013). Given the complexity of the native enthesis, it is likely that a combination of structural, biochemical and/or mechanical cues will be required to induce functional tissue regeneration. Cell seeding on scaffolds and the incorporation of biochemical cues on scaffold matrices will be discussed in the next sections.

2.2.2 Cells

Seeding of scaffolds with cells prior to implantation has been shown to improve tissue regeneration compared to empty scaffolds (Choi et al. 2014; He et al. 2014; Prosecka et al. 2015). Two main strategies can be distinguished: seeding of mature cell phenotypes of the tissue of interest (example: fibroblasts for tendon/ligament) or seeding of stem cells. For interface tissue engineering, the first strategy would require seeding of multiple cell types in spatially restricted regions. Although co-culture and cell interaction have been shown to positively enhance tissue-specific ECM deposition and promote tissue regeneration (Wang et al. 2007; Spalazzi et al. 2008; He et al. 2012), enough yield of autologous mature cells such as fibroblasts and chondrocytes are difficult to obtain. In addition, the regenerative capacity of terminally differentiated cells is inferior compared to that of stem cells. Thus, mesenchymal stem cells may be clinically more relevant because of their ease of expansion, regeneration capacity and multipotency (Font Tellado, Balmayor, and Van Griensven 2015).

The most common mesenchymal stem cell (MSC) sources used in tissue engineering are bone marrow-derived mesenchymal stem cells (BMSCs) and adipose-derived mesenchymal stem cells (AdMSCs) (Kern et al. 2006). Both have the capacity to differentiate into the multiple cell types present along the tendon/ligament-to-bone interface, including fibroblasts, fibrochondrocytes, chondrocytes and osteoblasts (Rothrauff and Tuan 2014). From a clinical point of view, AdMSCs present several advantages over BMSCs. AdMSCs can be easily obtained from fat tissue and expanded to high cell numbers (Schneider et al. 2017; Zhu et al. 2008). On the other hand, the process of harvesting BMSCs from bone marrow is more invasive and painful, and lower cell yields are obtained (Izadpanah et al. 2006; Kern et al. 2006).

The use of stem cells for interface tissue engineering implies the need of spatially controlling cell differentiation and ECM deposition to promote the regeneration of different tissue compartments.

Spatial control of cell differentiation to obtain a continuous change in cell phenotypes from a single cell source remains a challenge for tissue engineers.

2.2.3 Biochemical cues: growth factors

Biochemical cues, including growth factors, peptides, DNA and small molecules can be incorporated in scaffolds with the objective to elicit specific cell responses that promote tissue regeneration. Growth factors are potent tools to regulate cell behavior and have been shown to improve tissue regeneration in both *in vitro* and *in vivo* models (Hutton et al. 2013; Manning et al. 2011; James et al. 2011; Lee, Silva, and Mooney 2011; Younesi et al. 2017).

Multiple studies have addressed the effect of growth factors on stem cell differentiation for cartilage and bone tissue engineering applications (Cicione et al. 2015; Della Porta et al. 2015; Yilgor et al. 2009; Handorf and Li 2014; Weiss et al. 2010; Wang et al. 2009). On the other hand, the effects of growth factors on tendon/ligament and fibrocartilage differentiation have been less studied. Given the close relationship between tendon/ligament, cartilage and enthesis development, it is likely that tenogenic/ligamentogenic and chondrogenic factors are involved in fibrochondrogenic differentiation of MSCs (Lu and Thomopoulos 2013).

2.2.3.1 Growth factors of the TGF-β family

Growth factors of the TGF-β family have been widely investigated given their key role on musculoskeletal development. TGF-β 1-3 are key regulators of tendon/ligament and cartilage development (Lorda-Diez et al. 2009). TGF-β 1-3 signal by binding to TGF-β type I and II serine/threonine kinase transmembrane cell receptors (Guo and Wang 2009). Upon binding of TGF-β ligands to their receptors, Smad 2 and 3 are phosphorylated and translocated to the nucleus, where they act as transcriptional regulators (Guo and Wang 2009). TGF-βs have both pro-tenogenic and pro-chondrogenic effects (Demoor et al. 2014; Lorda-Diez et al. 2009). During embryonic development, TGF-β1 initiates MSC condensation, promotes early chondrogenic differentiation and maintains cartilage phenotype by preventing chondrocyte hypertrophy (Demoor et al. 2014). In addition, studies in mice embryos have shown that TGF-β2 and 3 signaling is necessary for tendon development, since TGF-β2/3$^{-/-}$ double mutants do not develop tendons (Lorda-Diez et al. 2009). In *in vitro* differentiation protocols, TGF-β1 and 3 are commonly used to

induce chondrogenesis of MSCs, while TGF-β2 has been less studied (Yin et al. 2015; Handorf and Li 2014). The discrepant effects of TGF-β family growth factors seem to depend on the molecular background and stage of differentiation of the cells (Lorda-Diez et al. 2009).

BMPs are also members of the TGF-β family. BMPs bind to type I and II TGF-β receptors, but signal via Smads 1, 5 and 8 (Guo and Wang 2009). BMP2, 6 and 7 can promote both cartilage and bone formation. Studies with skeletal progenitor cells suggest that BMP treatment promotes chondrogenesis in early culture stages, while at later stages it promotes chondrocyte hypertrophy and osteogenesis (Lorda-Diez et al. 2009; Hildner et al. 2010). In addition, the chondrogenic effects of BMPs take place only after the chondrogenic differentiation of MSCs has been induced by TGF-βs (Demoor et al. 2014). In *in vitro* differentiation protocols with MSCs, BMP2 and 7 are commonly used to induce bone formation (Bei et al. 2012; Bandyopadhyay et al. 2006; Beederman et al. 2013; Bais et al. 2009).

A subset of BMPs, in particular BMP13 (growth/differentiation factor 5, GDF5) and BMP12 (GDF7), have been shown to have pro-chondrogenic as well as pro-tenogenic/ligamentogenic effects (Lorda-Diez et al. 2009). *In vitro*, GDF5 has been shown to induce collagen II and GAG deposition by chondrocytes without enhancing the production of collagen X, a marker for cartilage hypertrophy (Enochson et al. 2014; Ayerst et al. 2017). Interestingly, GDF5 has been shown to play an important role during enthesis development and is expressed by enthesis progenitors (Dyment et al. 2015). The pro-tenogenic/ligamentogenic effects of GDF5/7 seem to happen only at late phases of tendon development (Lorda-Diez et al. 2009).

The complex interplay between growth factors and their interdependent effects on cell behavior highlight the need to explore their combined and sequential administration in *in vitro* differentiation protocols. In the present study, the chondrogenic, tenogenic/ligamentogenic and fibrochondrogenic effects of the growth factors TGF-β2 and GDF5 on AdMSCs will be analyzed both using single and combined administration.

2.2.3.2   Growth factor delivery

Clinical use of growth factors has been hindered by the lack of appropriate delivery systems. Growth factors have typically short half-lives, and therefore supraphysiological doses and repeated administration are required to obtain biological effects (Mitchell et al. 2016). This results in undesired side effects and increases the amount of protein needed and the associated costs.

Thus, one of the current challenges for tissue engineering applications is to develop delivery platforms that allow for a local and continued delivery of low doses of growth factors (Rambhia and Ma 2015).

Scaffolds can be used as platforms for growth factor delivery directly at the injury site. The mechanisms of incorporation of growth factors on scaffolds depend on the type of matrix and include protein entrapment, adsorption, surface immobilization and encapsulation into micro- or nanoparticles (Lee, Silva, and Mooney 2011; King and Krebsbach 2012; Wang et al. 2009; Bessa, Balmayor, Azevedo, et al. 2010; Bessa, Balmayor, Hartinger, et al. 2010). Recently, the ECM has become a source of inspiration for new growth factor delivery strategies. In native tissues, growth factors are stored in the ECM and are released in response to specific signals (Martino et al. 2015). Thus, the ECM tightly controls growth factor availability, spatial localization and diffusion (Martino et al. 2015; Silva et al. 2017).

The sulfated GAGs heparin and heparan sulfate have the ability to bind and release growth factors and thereby protect them from proteolysis. Heparin and heparan sulfate are very similar in structure but differ in their localization and grade of sulfation. Heparin is more sulfated and therefore more negatively charged, and is found exclusively in mast cells. Heparan sulfate is naturally present as a proteoglycan in the ECM of various tissues including cartilage. Heparin is approved for clinical use by the FDA and has been previously used in tissue engineering applications to control the delivery of various growth factors including BMP2, FGF2, vascular endothelial growth factor (VEGF) and GDF5 (Koo et al. 2013; Jeon et al. 2007; Jeon et al. 2006; Zieris et al. 2011). Binding of growth factors to heparin happens electrostatically through specific protein domains on the growth factors termed "heparin binding domains". Binding to heparin increases growth factor's half-lives by protecting them from proteolytic degradation and can increase their biological activity by facilitating their binding to cell surface receptors (Rider and Mulloy 2017; McCaffrey et al. 1989).

2.2.4 State of the art on tendon/ligament-to-bone tissue engineering

To date, few studies have explored the fabrication of tendon/ligament-to-bone constructs when compared to other musculoskeletal tissues, such as cartilage, bone or the osteochondral interface. Most tissue engineering approaches for enthesis regeneration have focused on the fabrication of stratified scaffolds (composed of two or more phases) that aim at mimicking the different tissue regions of native entheses.

One approach for enthesis tissue engineering consists on the fabrication of scaffolds composed of aligned and non-aligned fibers that mimic the change in collagen I orientation at the native interface (Criscenti et al. 2016; Xie et al. 2010). Criscenti et al. (2016) fabricated a triphasic scaffold composed of aligned polylactic-co-glycolic acid (PLGA) fibers electrospun on top of 3D-printed PCL with a 0-90° layer configuration. The aligned PLGA layer alone corresponded to the tendon/ligament part, the PCL to the bone part, and the PLGA on top of the PCL to the transition area. Each part of the construct had different porosities and mechanical properties, resulting in differential metabolic and ALP activity of BMSCs seeded on each part of the scaffolds. Liu et al. (2014) reported the fabrication of an aligned electrospun PLGA scaffold incorporating a mineral gradient to mimic both collagen alignment and mineral content of the native enthesis. This scaffold was tested *in vivo* in a rat model (Lipner et al. 2015), but healing was poor and dominated by the formation of scar tissue.

Despite their interesting characteristics, poor cell infiltration and nutrient transport are an issue of fibrous scaffolds, especially in the case of nanofibers (Nerurkar et al. 2011; Bhattacharjee et al. 2012). Thus, porous scaffolds may be more suitable for tendon/ligament-to-bone tissue engineering because their open structure facilitates cell infiltration and more closely replicates the 3D architecture of native tissues. Mozdzen et al. (2016) fabricated a collagen-GAG porous scaffold composed of two regions: a non-mineralized zone with aligned pores (tendon-like) and a mineralized zone with non-aligned pores (bone-like). Pore alignment and applied strain were found to influence the morphology of BMSCs, but their effects on other cell differentiation or tissue regeneration markers were not reported. Li et al. (2016) proposed an interesting approach consisting of the fabrication of microporous silk fibroin sponges integrated into a knitted silk fibroin mesh. These scaffolds showed promising results and improved ACL healing in a rabbit model.

Together, these studies provide new insights into the influence of scaffolds' structural and compositional characteristics on cell behavior and enthesis regeneration. However, the regeneration of a mature enthesis has not been yet achieved. Further research is needed to improve current understanding about relevant parameters for tendon/ligament-to-bone tissue engineering.

2.3 Evaluation of tissue engineered tendon/ligament-to-bone constructs

Characterization of a tissue engineered construct after *in vitro* culture or *in vivo* implantation is essential to evaluate tissue regeneration outcome and identify ways of improvement. Typically,

scaffolds are first tested *in vitro* for their ability to support cell viability and proliferation. Then, tissue regeneration is evaluated using specific indicators. For *in vitro* applications, the main used indicators to evaluate tissue engineering outcome are cell phenotype (morphology, gene and protein expression), ECM composition and mechanical properties. The present work focuses on *in vitro* evaluation only.

2.3.1 Markers of cell phenotype and tissue-specific ECM

In stem cell-based tissue engineering strategies, it is necessary to evaluate the degree of stem cell differentiation towards the cell phenotype of interest. Cell morphology, gene and protein expression patterns are indicators of cell phenotype, which change over time during the process of cell differentiation and maturation. In the present work, cell phenotypes of interest are tenocytes/ligamentocytes, fibrochondrocytes and chondrocytes.

ECM composition is a key determinant of tissue properties, such as stiffness and water content. Furthermore, cell-matrix interactions are key regulators of cell behavior. Analysis of ECM composition and deposition by the cells is essential to evaluate tissue regeneration and can be used as an indirect indicator of cell phenotype. This is particularly important in tendon/ligament and cartilage tissues, which have very low cell/matrix ratios (cells represent only 1-2% of the total volume) (Demoor et al. 2014; Subramanian and Schilling 2015). For interface tissue engineering, evaluation of ECM composition is crucial given the presence of specific and distinct ECM components in each tissue region (see section 2.1.1).

The next sections will deal with the phenotypic and ECM markers used to evaluate AdMSCs tenogenesis/ligamentogenesis, chondrogenesis and fibrochondrogenesis over time.

2.3.1.1 *Markers of tenogenesis/ligamentogenesis*

Tenocytes/ligamentocytes are elongated, spindle-shaped cells. The proliferation rate and metabolic activity of terminally differentiated tenocytes and ligamentocytes is typically low. During embryonic development, tenogenesis/ligamentogenesis is characterized by the upregulation of the transcription factors scx and mohawk (Liu, Zhu, et al. 2014; Ito et al. 2010; Liu et al. 2012; Subramanian and Schilling 2015). Scx is considered the master transcription factor for tendon/ligament development and is upregulated at early stages of tendon/ligament commitment.

mohawk is upregulated shortly after and independently of scx (Subramanian and Schilling 2015). Scx or mohawk overexpression *in vitro* is enough to transform MSCs into tenocytes (Subramanian and Schilling 2015). Scx and mohawk induce the expression of genes coding for tendon/ligament ECM matrix proteins, such as collagen I. Other components of the ECM of tendons and ligaments are the glycoproteins tenascin C and tenomodulin (Subramanian and Schilling 2015; Screen et al. 2015).

In the present work, the selected markers to evaluate tenogenic/ligamentogenic differentiation of AdMSCs at the gene level were therefore scx, mohawk, collagen I and tenascin C. ECM composition at the protein level was evaluated by the presence of collagen I.

2.3.1.2 Markers of chondrogenesis

Chondrocytes are round cells with very low proliferation rates and a hypoxic metabolism. Chondrocytes are embedded in a dense ECM with high water content and rich in collagen type II and proteoglycans, mainly aggrecan (Demoor et al. 2014). Chondrocytes are responsible for the regulation of ECM turnover and the synthesis of ECM components. The start of chondrogenic differentiation in embryonic development is marked by MSC condensation and the upregulation of sox9, the master transcription factor for chondrogenesis. Sox9 promotes the expression of further chondrogenic genes including collagen II and aggrecan (Quintana, zur Nieden, and Semino 2009). At later stages, chondrocytes of the growth plate become hypertrophic and finally apoptotic, leading to bone formation. Chondrocyte hypertrophy is characterized by the upregulation of collagen X and ALP (Quintana, zur Nieden, and Semino 2009; Kronenberg 2003).

In the present work, the markers used to evaluate chondrogenic differentiation of AdMSCs at the gene level are sox9, collagen II and aggrecan. At the protein level, ECM composition was analyzed by the presence of collagen II.

2.3.1.3 Markers of fibrochondrogenesis

Fibrochondrocytes are poorly characterized in comparison to tenocytes/ligamentocytes and chondrocytes. To date, there is a lack of specific markers to characterize fibrochondrogenesis. Based on developmental studies, it seems that both scx and sox9 are required for fibrochondrocyte commitment (Killian and Thomopoulos 2016; Sugimoto et al. 2013; Blitz et al.

2013) (see section 2.1.2). In addition, collagen II, collagen III and aggrecan are found in the enthesis ECM (Font Tellado, Balmayor, and Van Griensven 2015; Shaw and Benjamin 2007). Similar to chondrocytes, fibrochondrocyte hypertrophy is characterized by an increase in collagen X and ALP expression (Dyment et al. 2015). For those reasons, the gene markers selected to evaluate fibrochondrogenic differentiation were scx, sox9, collagen II, collagen III and aggrecan. At the protein level, the presence of collagen II and collagen III in the ECM were analyzed.

2.3.2 Mechanical parameters

Characterization of mechanical properties in tissue engineered tendon/ligament-to-bone constructs is essential to evaluate tissue functionality. Although it is not clear which are the minimal mechanical requirements to guarantee tissue function, mechanical properties should be comparable to those of native tissue. Two significant mechanical parameters are the response to tensile and compressive strains. Tissue elastic modulus in response to mechanical loads (stress/strain curves) can be evaluated in whole constructs using mechanical testing devices. The local distribution of stresses along the different tissue regions is more difficult to evaluate, but can be measured by ultrasound elastography or mechanical testing coupled to high resolution imaging (Rossetti et al. 2017; Spalazzi, Gallina, et al. 2006). In the present work, the Young's modulus of tendon/ligament-to-bone constructs was evaluated by subjecting the constructs to tensile stresses.

2.4 Aims and experimental approach

The main aim of this project was the fabrication, characterization and *in vitro* evaluation of integrated tendon/ligament-to-bone constructs for enthesis regeneration. Given the tight structure-function relationship at the native enthesis, we aimed at fabricating biomimetic scaffolds mimicking enthesis structural features. In particular, our objective was to fabricate biphasic constructs consisting of a region with anisotropic porosity (tendon/ligament-like) and a region with isotropic porosity (cartilage/bone-like) that recapitulate the change in collagen molecule alignment of the native enthesis. The anisotropic and isotropic regions were expected to integrate with each other in a transition region (enthesis-like) with a gradual change in pore alingment.

The first part of the project focused on 1) the fabrication and characterization of biphasic silk fibroin scaffolds for tendon/ligament-to-bone tissue engineering, 2) the comparison of two different

protocols for the fabrication of biphasic scaffolds and 3) the evaluation of the impact of scaffold's structural features on human AdMSCs. We hypothesize that scaffolds containing integrated regions of anisotropic and isotropic porosity can be fabricated using silk fibroin and combining the methodologies of directional freezing, solvent casting/particulate leaching and freeze-drying. We aimed at testing different fabrication parameters and analyzing their effects on scaffold structural characteristics. The criteria for scaffold evaluation were the integration between the anisotropic and isotropic parts, the mechanical integrity of the scaffold and the effect of scaffold structural features on AdMSCs. We hypothesize that different pore alignment in the anisotropic and isotropic parts of the scaffolds will result in different gene expression and cytoskeletal alignment of AdMSCs cultured on the scaffolds.

As discussed in the previous sections, tissue engineering strategies for enthesis regeneration will likely require a combination of structural, biochemical and/or mechanical cues to induce functional tissue regeneration. Thus, in the second part of the project we aimed at functionalizing biphasic silk fibroin scaffolds with heparin to incorporate biochemical cues in the form of growth factors. Focus points were 1) the functionalization of biphasic silk fibroin scaffolds with heparin for increased growth factor retention, 2) the analysis of growth factor incorporation and release kinetics from scaffolds, 3) the analysis of the combined effects of structural (scaffold pore morphology and alignment) and biochemical (TGF-β2 and GDF5 growth factors) cues on AdMSCs and 4) the identification of synergistic structural and biochemical parameters to promote spatially controlled tenogenesis/ligamentogenesis, fibrochondrogenesis and chondrogenesis of AdMSCs. We hypothesize that scaffold functionalization with heparin will increase growth factor retention on the scaffold matrix and reduce burst-like release kinetics. In addition, we expect the effects of growth factors on gene and protein expression of AdMSCs to vary depending on pore alignment.

This study follows a developmental paradigm in which the focus is put on structural and biochemical signals to generate an *in vitro* model of enthesis regeneration. Our model aims at replicating early stages of enthesis development to study enthesis regeneration. Mineralization and mechanical loads, which happen postnatally, were not evaluated. During development, tendons/ligaments attach to primary cartilage through the enthesis. Cartilage tissue is further remodeled into bone at later developmental stages (endochondral ossification). As described in section 2.1.2, the enthesis develops in close coordination with tendon/ligament and cartilage following a pattern that reminds of the growth plate. For this reason, biphasic silk fibroin scaffolds were evaluated for their capacity to induce stem cell tenogenesis/ligamentogenesis, fibrochondrogenesis and chondrogenesis rather than osteogenesis. Previous studies have reported that implanted cartilage can be remodeled into bone *in vivo* (Thompson et al. 2015).

3 MATERIALS & METHODS

All materials were purchased from Sigma-Aldrich (USA) unless otherwise stated.

3.1 Silk fibroin extraction and processing

Silk fibroin was extracted from *bombyx mori* cocoons (Chul Thai Silk Company, Thailand). The cocoons were delaminated and cut in small pieces. Next, the cocoon's pieces were submerged in two consecutive alkaline baths (1.5h in each bath) at 98°C containing 1.1 and 0.4 g/L Na_2CO_3, respectively, to remove immunogenic sericine. Next, fibroin fibers were washed with ddH_2O and dried overnight under the fume hood. Dry fibroin fibers were weighed to confirm sericin removal. Typically, between 25 to 30% of weight is lost during degumming.
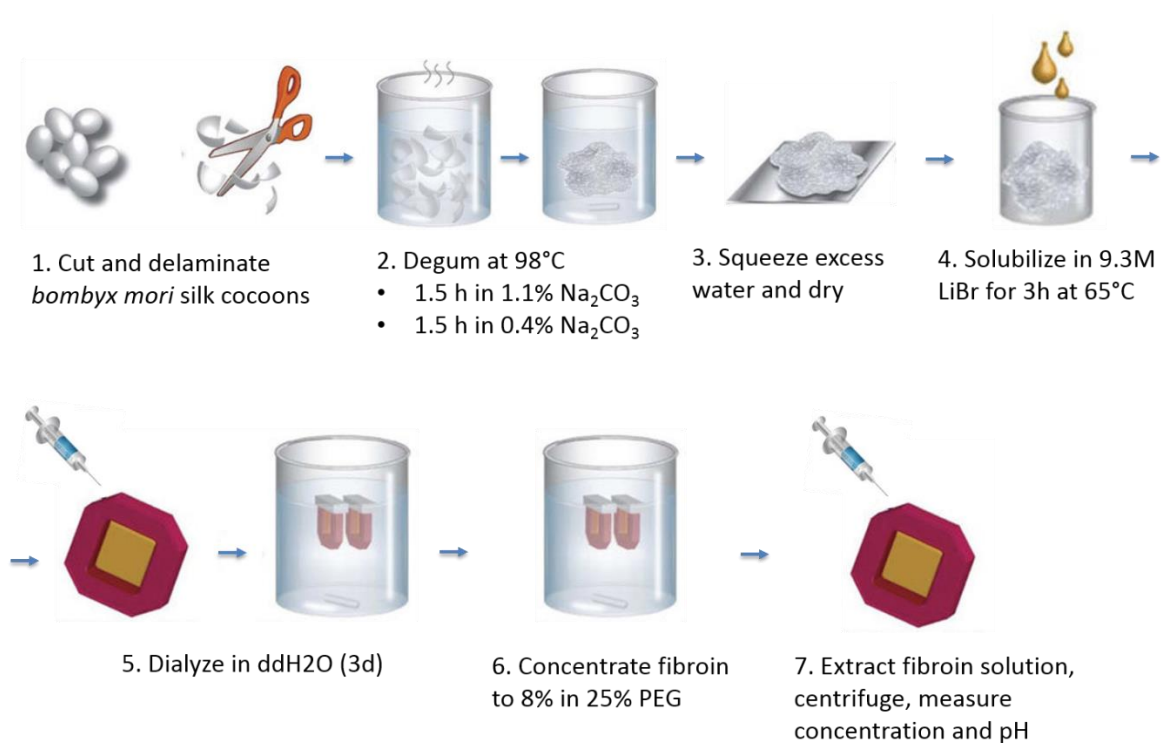
Figure 3. Silk fibroin extraction and processing. Workflow of silk fibroin processing from silk cocoons to aqueous silk fibroin solution. First, silk cocoons are cut in small pieces and delaminated. Next, cocoon's pieces are boiled at 98°C in two consecutive alkaline baths to remove immunogenic sericine (degumming) and dried overnight under the fume hood. Degummed fibroin is solubilized in lithium bromide (LiBr) for 3h at 65°C and dialyzed against ddH_2O for 3d. Subsequently, silk fibroin solution is concentrated to 8% using 25% poly-ethilene-glycol (PEG). Finally, fibroin solution is extracted and centrifuged to remove impurities. The pH of the solution is measured for quality control. Adapted from (Rockwood et al. 2011).

Degummed fibroin fibers were solubilized in 9.3M LiBr solution for 3h at 65°C. The obtained fibroin solution was dialyzed against ddH$_2$O for 3 days using 3500 MWCO Slide-A-Lyzer dialysis cassettes (Thermo Fisher Scientific, USA). After dialysis, the cassettes were immersed in 25% polyethylene glycol (PEG) (molecular weight = 10kDa) until a fibroin concentration of 8% was obtained. Protein concentration was measured with NanoDrop (NanoDrop tech, USA). To remove impurities, fibroin solution was centrifuged at 12700g (Eppendorf 5810R, Eppendorf, Germany) for 20min at 4°C. 8% fibroin solution (pH = 5-6) was used for scaffold fabrication right after extraction. The process of silk fibroin extraction and processing is summarized in figure 3.

3.2 Fabrication of anisotropic scaffolds

Silk fibroin scaffolds with anisotropic porosity were fabricated by directional freezing and freeze-drying (figure 4). Freezing temperature and silk fibroin solution concentration were experimentally optimized to maximize pore sizes without compromising pore alignment. Freezing temperatures tested were -20°C and -50°C. Silk fibroin concentrations tested were 5% and 8%. The conditions selected were: -20°C and 8% fibroin solution (see section 4.1).

Cylindrical polypropylene (PP) molds (Braun, Germany) of 8mm diameter x 50mm length were filled with 800μl of 8% silk fibroin solution and press-fit in a polystyrene foam. The molds were frozen inside the foams at -20°C for 24h. The polystyrene acted as a heat insulator along the lateral surface of the PP cylinder, generating a temperature gradient that induced the formation of vertically-oriented ice crystals in the fibroin solution (Deville et al. 2006). After freezing, the PP cylinders were removed from the polystyrene and lyophilized using an Alpha 1-2 LDplus freeze-dryer (Martin Christ, Germany) for 48h. Sublimation of the ice crystals during freeze-drying resulted in the formation of vertically-oriented (anisotropic) pores. Subsequently, scaffolds were treated with 80% methanol for 30min to induce a conformational change from silk I (water soluble) to silk II (water insoluble) protein conformation. After treatment, the scaffolds were extensively washed with ddH$_2$O and subjected to a second freezing and freeze-drying cycle. The process of fabrication of anisotropic scaffolds is summarized in figure 4.
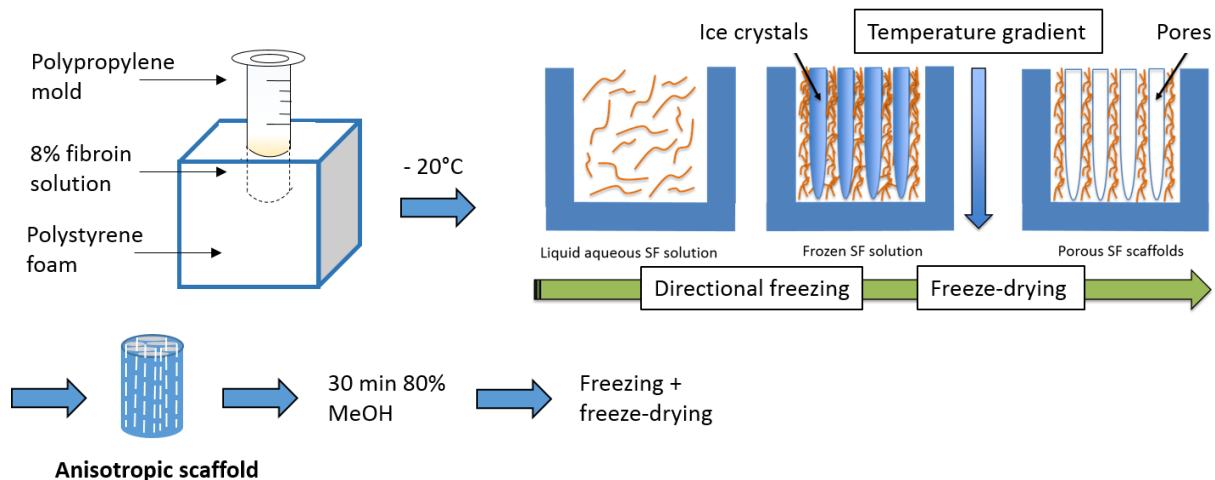
Figure 4. Fabrication of anisotropic silk fibroin scaffolds. Schematic representation of the process of fabrication of anisotropic silk fibroin (SF) scaffolds. 8% fibroin solution is frozen at -20°C in a polypropylene (PP) mold press-fitted in a polystyrene foam for 24h. The polystyrene foam acts as a heat insulator and creates a temperature gradient that induces the formation of vertically-oriented ice crystals in the fibroin solution. Samples are freeze-dried for 24h to induce the sublimation of ice crystals. The obtained scaffolds are treated with 80% methanol (MeOH) to induce a protein conformational from the silk I to the silk II structure. After treatment, scaffolds are subjected to another freezing and freeze-drying cycle and stored at room temperature until use. Adapted from (Font Tellado et al. 2017).

3.3 Fabrication of isotropic scaffolds

Silk fibroin scaffolds with isotropic pores were fabricated by solvent casting/particulate leaching and freeze-drying. NaCl crystals of size 400 – 800µm were used as a porogen. Particle size was selected to obtain pores of sizes 200 - 300µm. 0.2g of NaCl crystals were poured and pressed in a PP mold of 8mm diameter x 30mm length. Next, 200µl of 8% silk fibroin solution were poured on top of the NaCl crystals. Samples were left at room temperature (RT) for 48h to allow for fibroin gelation. Next, NaCl particles were leached by incubating the samples for 3 days in ddH$_2$O under shaking. The obtained scaffolds were frozen at -20°C and freeze-dried for 24h. The process of fabrication of isotropic scaffolds is summarized in figure 5.
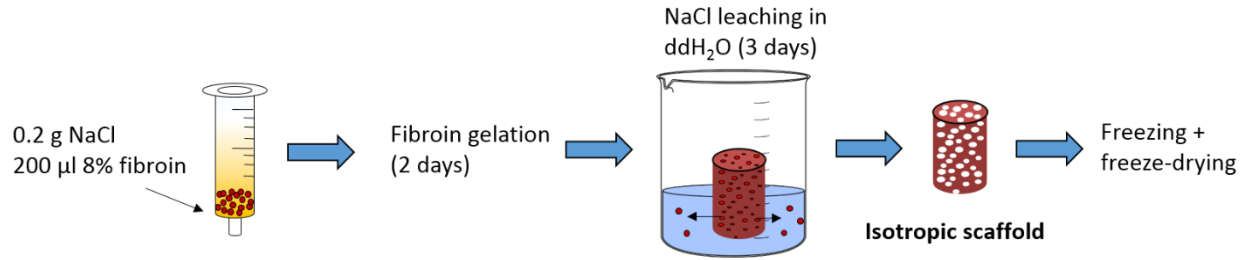
Figure 5. Fabrication of isotropic silk fibroin scaffolds. Schematic representation of the process of fabrication of isotropic silk fibroin scaffolds. Sodium chloride (NaCl) particles of size 400 – 800µm are placed in a polypropylene (PP) mold and 8% fibroin solution is poured on top. Samples are left under the fume hood for 48h to allow for fibroin gelation. Next, NaCl particles are leached out of silk fibroin scaffolds in ddH$_2$O for 3d under shaking. The obtained scaffolds are subjected to a freezing (-20°C) and freeze-drying cycle. Adapted from (Font Tellado et al. 2017).

3.4 Fabrication of biphasic scaffolds

Biphasic silk fibroin scaffolds with anisotropic and isotropic pores were fabricated following two-step protocols (protocol A or B). The process of fabrication of biphasic scaffolds is summarized in figure 6.

Protocol A. In the first step, scaffolds with anisotropic porosity were produced as described in section 3.2. In the second step, 0.2g of NaCl particles (400 – 800 µm) were pressed at the bottom of cylindrical PP molds (8mm diameter x 30mm length) and 200µl 8% fibroin solution were poured on top. Next, scaffolds with anisotropic porosity (size 8mm diameter x 5mm length) were placed on top of the mixture, in direct contact with the fibroin solution. Solvent casting/particulate leaching, freezing and freeze-drying were performed as described for isotropic scaffolds (section 3.3). The obtained scaffolds are hereafter termed "Type A scaffolds". Scaffold dimensions were 8mm diameter x 10mm length.

Protocol B. In the first step, scaffolds with isotropic porosity were produced as described in section 3.3. In the second step, isotropic scaffolds were wetted with ddH$_2$O and placed at the bottom of cylindrical PP cylinders (8mm diameter x 50mm length). 800µl 8% fibroin solution were poured on top. Next, the PP cylinders were press-fit in a polystyrene foam and frozen at -20°C for 24h. Freeze-drying and methanol treatment were performed as described for anisotropic scaffolds (section 3.2). The obtained scaffolds are hereafter termed "Type B scaffolds". Scaffold dimensions were 8mm diameter x 10mm length.
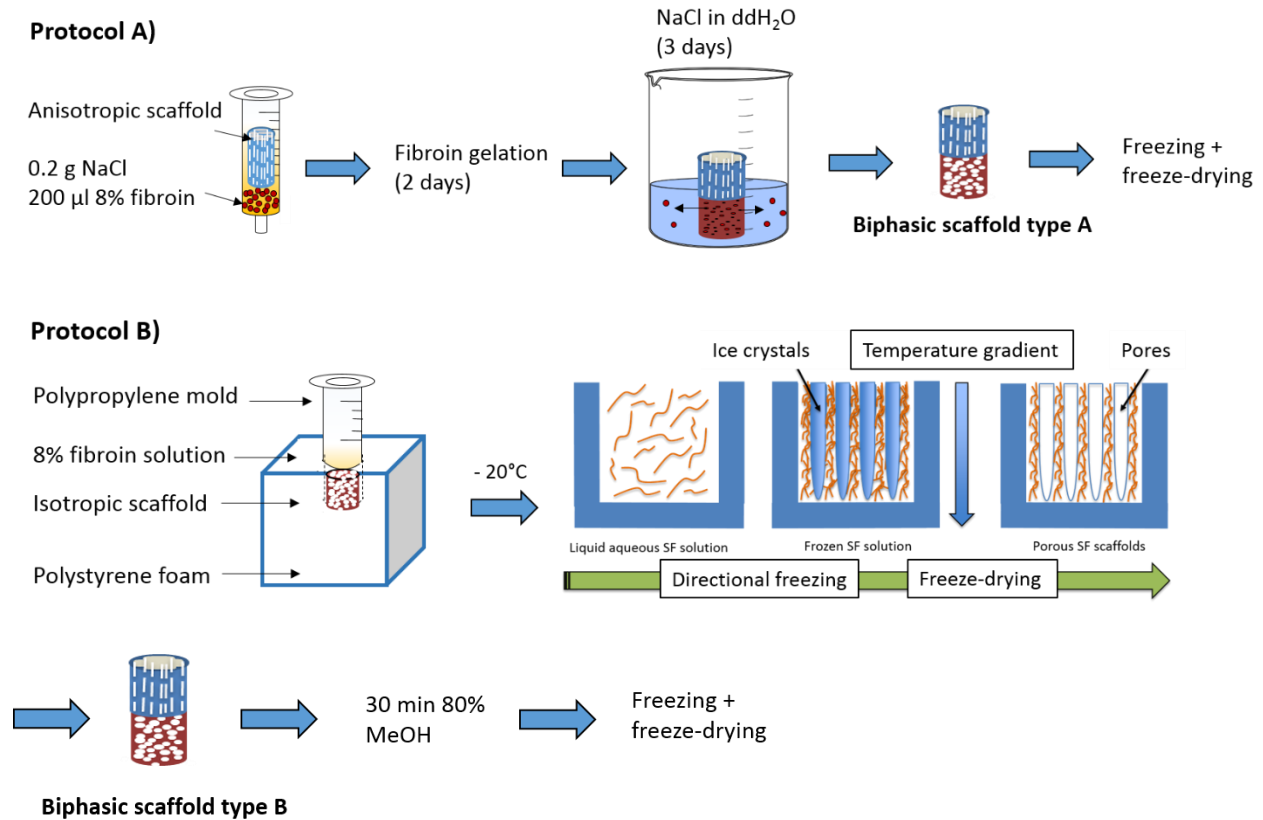
Figure 6. Fabrication of biphasic silk fibroin scaffolds. Schematic representation of the process of fabrication of biphasic silk fibroin (SF) scaffolds. Two step protocols were followed (A or B). *Protocol A*. Anisotropic scaffolds were produced first and placed on top of a mixture of 8% silk fibroin solution and sodium chloride (NaCl) particles (size 400 – 800µm) in a PP mold. Fibroin gelation, NaCl particle leaching, freezing and freeze-drying were performed as described for isotropic scaffolds (section 3.3, figure 5). *Protocol B*. Isotropic scaffolds were produced first, soaked in ddH$_2$O and placed in PP molds. The PP molds were press-fit in a polystyrene foam. 8% silk fibroin solution was poured on top of the isotropic scaffolds. Samples were immediately frozen at -20°C for 24h (directional freezing). Freeze-drying and post-treatment with methanol (MeOH) were performed as described for anisotropic scaffolds (section 3.2, figure 4). Adapted from (Font Tellado et al. 2017).

3.5 Scaffold characterization

3.5.1 Fourier transform infrared spectroscopy (FTIR)

Secondary protein structures in fibroin were analyzed by FTIR in attenuate total reflectance (ATR) mode. The spectrophotometer used was a PerkinElmer Spectrum One (Perking Elmer, Waltham, MA, USA) equipped with Zinc Selenide crystal on ATR. Anisotropic and isotropic silk fibroin

scaffolds were analyzed in dry conditions. Over 64 scans were averaged to obtain sample spectra, ranging from 650 to 4000 cm^{-1} at a resolution of 4 cm^{-1}.

3.5.2 Digital light microscopy

The morphology of type A and B biphasic scaffolds was analyzed by digital light microscopy. The microscope used was a Keyence VHX 6000 (Keyence, Japan). Scaffold transversal sections (2mm thickness) were used to image the surface and inner regions. Fully focused images of 3D scaffolds were obtained by scanning through the focal range of a sample and compiling images at different focal frames using the Keyence VHX 6000 software.

3.5.3 Field-Emission Scanning electron microscopy (FESEM)

The morphology and pore alignment of silk fibroin scaffolds was characterized by FESEM. Scaffold transversal or cross-sections were used. Prior to imaging, scaffolds were placed in adequate metallic supports and coated with Pt/Pd alloy (80/20) using a Q150R sputter coater (LOT-Quantum Design, Germany). The microscope used was a Zeiss Supra 40 (Carl Zeiss, Germany). Samples were imaged at 4 kV.

3.5.4 Micro-computed tomography (μCT)

The morphology, porosity and pore size of biphasic silk fibroin scaffolds were analyzed by μCT. The equipment used was a Skyscan1176 μCT (Bruker, USA). Scaffolds of 8mm diameter x 10mm length (n=4 of each type, A or B) were scanned at a voxel size of 9μm. 3D images were created using μCT scans with the Skyscan CTRecon software (Bruker, USA) using a built-in algorithm. Analysis of scaffold porosity and pore size distribution was done on 3D reconstructed images with the Skyscan CTanalysis software (Bruker, USA) using a built-in algorithm. Scaffold porosity was analyzed on whole scaffolds and on its separate parts (anisotropic, isotropic, and transition between the anisotropic and isotropic parts). The different parts were visually clustered along the Z axis of the scaffolds. Areas with aligned porosity only were defined as the anisotropic region. Areas with non-aligned porosity only were defined as the isotropic region. Areas were both types of porosity could be appreciated were defined as the transition region. In addition, 2D scans were grouped in sections of 1mm thickness x 8mm diameter along the Z axis of the scaffolds to analyze the distribution of porosity along the Z axis.

3.5.5 Permeability

The permeability of anisotropic, type A and type B scaffolds (n=5) was analyzed using an in-house built bioreactor equipped with a pressure controller. The pump used was an Arthrex continuous wave II AR6450 (Arthrex, USA). Scaffolds were press-fit in cylindrical steal inserts (8mm diameter) and placed in the bioreactor. Phosphate buffered saline (PBS) at 20% flow was pumped through the scaffolds at a specific pressure ranging from 5 to 16 kPa. The time needed for 5ml of PBS to go through a scaffold was measured and the fluid flow rate (Q) (m^3/s) was calculated using the formula $Q = v/t$, where v is the liquid volume in m^3 and t the time in s. Scaffold permeability (K) (darcy) was calculated using the formula $K = Ql\eta/\varDelta pA$ where Q is the flow rate in m^3/s, l is the specimen length, η is the viscosity of flowing liquid, Δp is the pressure difference from the top to the bottom of the specimen and A is the cross-sectional area. The cross-sectional area of cylindrical scaffolds was calculated as πr^2, where r is the radius (porosity was not included in the calculation).

3.5.6 Mechanical testing

Type A and B biphasic scaffolds and anisotropic scaffolds (n=5 for each group) were subjected to tensile strain using a zwicki1120 uniaxial test system (Zwick/Roell, Germany) equipped with a 2.5 kN load cell (KAF-Z 2.5 kN, class 0.05, A.S.T, Germany). A mechanical compensation unit was integrated between the traverse and the load cells to avoid shear and torsional forces. Prior to testing, the scaffolds were glued to polyamide cubes (Technoplast, Germany) to provide standardized loading. The cubes were fixed in the testing equipment with compression clamps. Biphasic scaffolds were placed with the isotropic part on the bottom and pulled from the anisotropic part up. The mechanical testing setup is shown in figure 7. All scaffolds were tested in wet conditions (soaked in PBS) at an elongation rate of 1mm/min. Young's modulus was calculated from the linear part of the stress-strain curve (2-5% strain) by linear regression. Maximum applied strain was 15%. Isotropic scaffolds were not evaluated due to their small size and high penetration of the glue inside the scaffold's pores.

3.6 Functionalization of biphasic silk fibroin scaffolds with heparin

Type B biphasic silk fibroin scaffolds were functionalized using heparin sodium salt from porcine intestinal mucosa. Covalent binding between carboxyl groups in heparin and primary amines in

fibroin was performed with carbodiimide chemistry. The crosslinkers used were 1-ethyl-3-(3-dimethylaminopropyl)carbodiimide hydrochloride (EDC) and N-hydroxysuccinimide (NHS) (Carl Roth, Germany). First, scaffolds were incubated in 0.1M 2-(N-morpholino)ethanesulfonic acid (MES) buffer (pH 5.8) for 30min at RT under shaking. Next, heparin was dissolved to a final concentration of 3% in MES buffer and sterile filtered using 0.2µm filters (Sarstedt, Germany). EDC and NHS were added at a final concentration of 0.25M and 0.125M, respectively, to activate carboxyl groups in heparin molecules. The reaction was conducted for 15min at RT under shaking and quenched with 0.2M 2-mercaptoethanol. Subsequently, each scaffold reacted with 1ml of 3% activated heparin solution for 4h at RT under shaking. Scaffolds having reacted with activated heparin are hereafter termed "scaffolds crosslinked with heparin" or "heparin-crosslinked scaffolds". Naked scaffolds (termed "unmodified scaffolds") and scaffolds having reacted with 3% non-activated heparin solution (without EDC/NHS, termed "scaffolds non-crosslinked with heparin" or "non-crosslinked scaffolds") were used as controls. All scaffolds were washed 5 times with MES buffer and 3 times with ddH$_2$O to remove excess heparin. Scaffolds used for growth factor loading and cell culture were additionally incubated for 3 days in ddH$_2$O to ensure complete removal of unbound heparin. All reactions and washing steps were performed in sterile conditions.
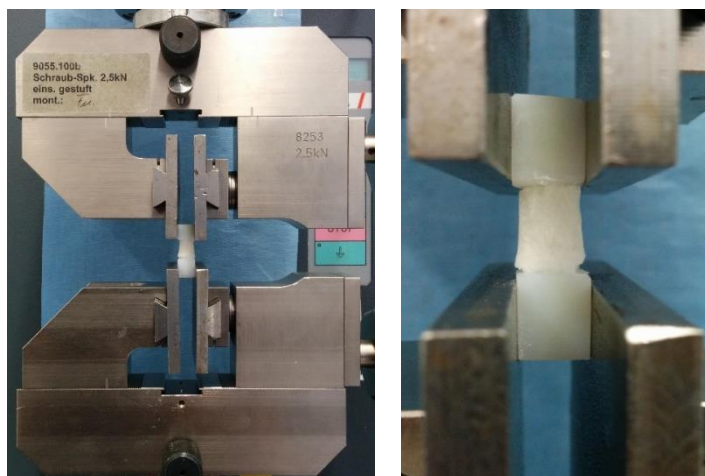
Figure 7. Mechanical testing setup. The image depicts an anisotropic scaffold placed in the mechanical tensile testing device. The left image shows an overview of the device and the position of the scaffold and the fixation clamps. The right image shows in more detail how the scaffold is attached to polyamide cubes in the top and bottom parts, and how the polyamide cubes are fixed to the clamps. Adapted from (Font Tellado et al. 2017).

3.6.1 Quantification of heparin binding efficiency and release

Heparin release was quantified after washing with MES buffer and ddH$_2$O. Each scaffold was incubated in 1ml of ddH$_2$O and 100µl were taken after 1h, 3h, 1d, 3d and 7d for quantification. 100µl fresh ddH$_2$O were replenished at every measuring point.

Heparin quantification was done using a Blyscan Sulfated Glycosaminoglycan (GAG) assay (Bicolor, United Kingdom) according to the manufacturer's instructions. Heparin binding efficiency and release were quantified in non-crosslinked and heparin-crosslinked type B scaffolds (n=6 for each group). Heparin binding efficiency was determined indirectly by measuring the amount of unreacted heparin in MES buffer after the conjugation reaction (before washing).

The amount of heparin released after 3 days was used to estimate the amount of heparin remaining bound to scaffolds used for growth factor binding and cell culture after 3 days washing. This was done by subtracting the heparin released at 3 days from the total heparin incorporated after conjugation.

3.7 TGF-β2/GDF5 binding to biphasic silk fibroin scaffolds

TGF-β2 and GDF5 (Peprotech, USA) were added to type B silk fibroin scaffolds (unmodified, non-crosslinked with heparin and crosslinked with heparin) (n=3 for each group). Growth factor loading was performed by incubating the scaffolds in 500µl of a PBS solution containing 200ng/ml of TGF-β2 or GDF5 (single growth factor loading) or 100ng/ml TGF-β2 + 100ng/ml GDF5 (double growth factor loading). The reaction was performed at RT for 3h under shaking.

3.7.1 Quantification of TGF-β2/GDF5 binding efficiency and release

Binding efficiency and release prolife of TGF-β2/GDF5 from type B biphasic silk fibroin scaffolds (unmodified, non-crosslinked with heparin or crosslinked with heparin) (n=3 for each group) were quantified by ELISA. Growth factor release was quantified by incubating each scaffold in 1ml Dulbecco's Modified Eagles Medium (DMEM) supplemented with 2% fetal calf serum (FCS) and 1% Penicillin/Streptomycin (P/S) at 37°C to simulate cell culture conditions. 100µl of medium were taken for quantification after 1h, 3h, 1d, 3d, 7d or 14d and replenished with 100µl fresh medium. TGF-β2 was quantified using a TGF-β2 ELISA kit (Diaclone, France) and GDF5 using a DuoSet DY853 GDF ELISA kit (R&D, USA) following the manufacturer's instructions. Binding efficiency

was calculated indirectly by quantifying the amount of unbound TGF-β2/GDF5 in PBS after the conjugation reaction.

3.8 Adipose-derived mesenchymal stem cells (AdMSCs) isolation and expansion

Human adipose tissue was obtained from healthy donors after written informed patient's consent according to the guidelines of the Local Ethics Committee of ''Klinikum Rechts der Isar'' at the Technical University of Munich, Germany. AdMSCs isolation was performed as described in (Schneider et al. 2017). Briefly, fat tissue was cut in small pieces ranging 1-1.5mm, washed with PBS and centrifuged twice at 430g for 5min to separate the stromal fraction. Next, fat tissue was digested with 1.45% collagenase solution (Merck Millipore, USA) at 37°C for 1h and centrifuged at 600g for 5min to obtain a cell pellet. Cells were cultured in 175cm^2 cell culture flasks (Eppendorf, Germany) at 37°C and 5% CO_2 in a humidified atmosphere. Culture medium consisted of high glucose DMEM supplemented with 10% FCS and 1% P/S (AdMSCs growth medium) and was changed twice a week. Cells were passaged at 80% confluence and used between passages 2 and 4 for cell culture experiments.

3.8.1 AdMSCs culture on biphasic silk fibroin scaffolds

Biphasic silk fibroin scaffolds were punched to a final dimension of 4mm diameter x 8mm length using disposable biopsy punches (Integra Miltex, USA). Prior to cell culture, scaffolds were sterilized with 70% ethanol, washed with PBS and incubated in growth medium overnight at 37°C to improve cell attachment. AdMSCs were seeded on the scaffolds at a density of 4 x 10^5 cells/scaffold. Seeding was performed in a small volume (60 µl) to improve seeding efficiency. To ensure homogenous cell distribution on the scaffolds, seeding was performed on both scaffold sides (anisotropic and isotropic, 30µl on each side). After seeding, scaffolds were incubated for 2h at 37°C to facilitate cell attachment. Cells were cultured either in growth medium or in high glucose DMEM containing 2% FCS and 1% P/S (AdMSCs low serum medium). In the first part of the project, cells were cultured on growth medium to analyze scaffold biocompatibility and effect of structural cues on morphology and gene expression. The second part of the project was more focused on evaluating AdMSCs differentiation, and thus low serum medium was used to promote differentiation over proliferation. Medium was changed every 2 days.

3.8.2 Metabolic activity and seeding efficiency

The metabolic activity and seeding efficiency of AdMSCs on biphasic silk fibroin scaffolds was quantified by 3-(4,5-Dimethylthiazol-2-yl)-2,5-diphenyltetrazoliumbromid (MTT) assay after 1, 3 or 7 days of culture in low serum medium (N=3, n=9). The scaffolds tested were type B biphasic scaffolds unmodified, crosslinked with heparin without growth factors (unloaded) or crosslinked with heparin and loaded with TGF-β2/GDF5. Samples were washed with PBS and incubated for 2h at 37°C with 0.012M MTT solution. Blue precipitates appeared on the scaffolds as a consequence of MTT processing to formazan by metabolically active cells. Next, samples were incubated for 1h in isopropanol at RT under shaking to dissolve the precipitates. Optical density (OD) at 570 and 690 nm was measured using a FLUOstar Omega photometer (Labtech, Germany). Metabolic activity of AdMSCs on heparin-crosslinked scaffolds unloaded or loaded with TGF-β2/GDF5 was expressed as percentage relative to metabolic activity of AdMSCs on unmodified scaffolds. Seeding efficiency was calculated 24h after seeding as the ratio between the OD of cells attached to the scaffold and the OD of total cells seeded.

3.9 Cytotoxicity and viability

Cytotoxity was quantified by measuring the release of lactate dehydrogenase (LDH) to the cell culture supernatant. AdMSCs (N=3, n=9) were cultured on biphasic silk fibroin scaffolds with growth medium for 1, 3 or 7 days. LDH was quantified using a Fluitest LDH-L kit (Analyticon, Germany) following the manufacturer's instructions. OD at 340 nm was measured.

Viability and cytotoxicity were also qualitatively analyzed by live/dead staining after 7 days of culture on growth medium. Samples were washed with PBS and stained with 0.05% Calcein AM, 0.2% propidium iodide and 0.01% hoechst (in PBS) for 15min at 37°C. Sample imaging was performed using a Keyence B7-9000 fluorescent microscope (Keyence, Japan). Cell viability and distribution on the scaffold were qualitatively evaluated.

3.10 Proliferation

The proliferation of AdMSCs (N=3, n=9) on biphasic silk fibroin scaffolds was measured by dsDNA quantification. After 3, 7 or 14 days of culture in growth medium, scaffolds were washed in PBS and cut in small pieces. Scaffold pieces were stored in ddH$_2$O and subjected to 2 freeze-thaw

cycles (at -80 and 37°C) to induce cell lysis. dsDNA was quantified using the Quant-iT™ PicoGreen dsDNA assay kit (Life Technologies, USA) according to the manufacturer's instructions. Briefly, samples were diluted in a buffer containing 200mM Tris-HCl and 20mM Ethylenediaminetetraacetic acid (EDTA) in PBS. Next, samples were incubated for 5min in the Quant-iT™ PicoGreen reagent and OD at 520 nm was measured. The obtained values were compared to a standard curve of known dsDNA concentration to calculate the amount of dsDNA in test samples.

3.11 Immunofluorescence and confocal microscopy

The morphology and pore alignment of anisotropic silk fibroin scaffolds was analyzed by staining with green fluorescent dye Rhodamine 123 solution (0.2mg/ml) for 15min at RT. In addition, the pore morphology of both anisotropic and isotropic silk fibroin scaffolds was observed by staining with DAPI (4′,6-diamidino-2-phenylindole) following the manufacturer's instructions.

AdMSCs morphology, cytoskeletal alignment and distribution on type A and B biphasic silk fibroin scaffolds was analyzed by immunofluorescence staining. After 14 days of culture on the scaffolds in growth medium, cells were fixed with 4% formaldehyde in PBS for 30min at RT and permeabilized with 0.2% Triton X-100 in PBS for 20min at RT. Next, cells were stained with Oregon Green 488 Phalloidin (Thermo Fisher Scientific, USA) and DAPI following the manufacturer's instructions.

The presence of collagen types I, II and III was analyzed in type B silk fibroin scaffolds crosslinked with heparin and unloaded or loaded with TGF-β2/GDF5. The following antibodies were used (Abcam, Germany). Primary: collagen I (ab34710, 1:500), collagen II (ab34712, 1:200) and collagen III (ab7778, 1:200). Secondary: IgG goat anti-rabbit, conjugated with Alexa Fluor 488 (ab150077, 1:1000). All antibodies were diluted in 1% bovine serum albumin (BSA) in PBS. After 14 days of culture on scaffolds in low serum medium, AdMSCs were fixated with 4% formaldehyde in PBS for 30min at RT and permeabilized with 0.2% Triton X-100 in PBS for 20min at RT. Next, scaffolds were incubated in 1% BSA in PBS for 1h at RT. Subsequently, scaffolds were cut in transversal sections (2mm thickness) and stained with primary antibodies overnight at 4°C. Next, samples were washed 3 times in PBS and stained with secondary antibody at RT for 1h. Finally, scaffolds were washed with PBS and stained with Alexa Fluor 594 Phalloidin (Thermo Fisher Scientific, USA) and DAPI following the manufacturer's instructions.

All samples were imaged using a Nikon A1 confocal microscope (Nikon Instruments, The Netherlands). Imaging of whole scaffolds was performed by taking pictures at multiple Z stacks (10-15 stacks, 50µm each) and generating a 2D projection image containing information from all Z stacks.

3.12 Gene expression

Gene expression of tendon/ligament, enthesis and cartilage differentiation markers was analyzed in type A and B biphasic silk fibroin scaffolds. AdMSCs (N=3, n=9) were cultured for 7 or 14 days on the scaffolds in growth medium (unmodified scaffolds type A and B) or low serum medium (scaffolds type B crosslinked with heparin unloaded or loaded with TGF-β2/GDF5). Next, the scaffolds were washed in PBS and cut in 3 parts (anisotropic, transition, isotropic) to analyze gene expression in each region separately. The change from anisotropic to isotropic porosity can be distinguished with the naked eye (see figure 11). The transition was defined as the region 0.5mm up and 0.5mm down from the detectable porosity change. Each part was cut in small pieces and stored at -80°C in TRIreagent for at least 24h. Next, RNA isolation in TRI reagent was performed by chloroform extraction following the manufacturer's instructions. RNA quantity and quality was measured with NanoDrop. Reverse-transcription to cDNA was performed using a first strand cDNA synthesis kit (Thermo Scientific, USA) according to the manufacturer's instructions. The thermocycler used was a C1000 Touch Thermal Cycler (Eppendorf, Germany).
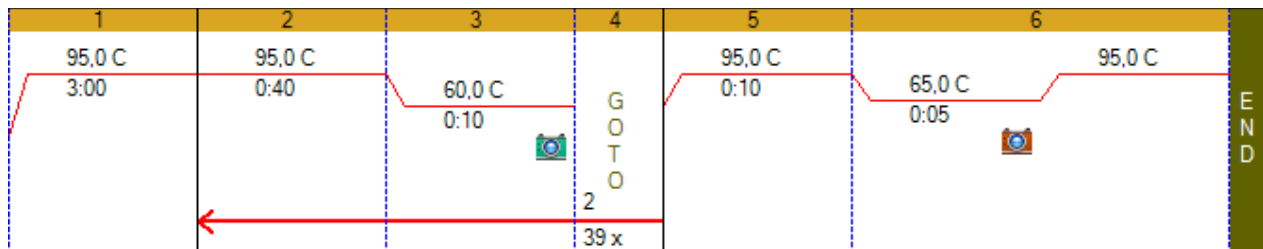

Figure 8. qPCR run protocol. Protocol used for qPCR. A starting denaturation cycle was performed at 95°C for 3min. Next, a short denaturation cycle (40s at 95 °C) followed by a hybridization/elongation cycle (10s at 60°C) was performed 40 times (total of 40 cycles). After the 40 cycles, a short denaturation cycle (10s at 95°C) followed by an increase in temperature from 65°C to 95°C in 5s was performed to measure melting curves. The cameras indicate the points were fluorescence was measured.

Quantitative analysis of gene expression was performed by quantitative polymerase chain reaction (qPCR). 30ng of sample cDNA were used per reaction. The thermocycler used was a CFX96 Real Time System thermocycler (BioRad, USA). Sso Fast EvaGreen supermix (BioRad, USA) was used as a detection reagent. The qPCR run protocol used is shown in figure 8. The primers used and their sequences are shown in table 1. Results from unmodified type A and B scaffolds were expressed as fold change relative to the housekeeper gene β-Tubulin ($2^{-\Delta Ct}$). Results from heparin-crosslinked type B scaffolds were expressed as fold change relative to the housekeeper and to unloaded scaffolds (heparin-crosslinked without growth factors) ($2^{-\Delta\Delta Ct}$).

Target gene	Forward (5' → 3')	Reverse (5' → 3')
Aggrecan	TCGAGGACAGCGAGGCC	TCGAGGGTGTAGCGTGTAGAGA
β-Tubulin	GAGGGCGAGGACGAGGCTTA	TCTAACAGAGGCAAAACTGAGCACC
Collagen I A1	AGCGGACGCTAACCCCCTCC	CAGACGGGACAGCACTCGCC
Collagen II	AACCAGATTGAGAGCATCCG	ACCTTCATGGCGTCCAAG
Collagen III	TACTTCTCGCTCTGCTTCATCC	GAACGGATCCTGAGTCACAGAC
Mohawk	TGGTTTGCTAATGCAAGACG	CCTTCGTTCATGTGGGTTCT
Scleraxis	CAGCCCAAACAGATCTGCACCTT	CTGTCTTTCTGTCGCGGTCCTT
Sox9	GAGCCGAAAGCGGAGCTGGAA	ACAGCTGCCCGCTCCAAGTG

Table 1. Primers used for qPCR. Primer sequences used for quantitative polymerase chain reaction (qPCR). β-Tubulin was used as a housekeeper.

3.13 Statistical analysis

Statistical analysis of quantitative data was performed using GraphPad Prism version 5.00 (GraphPad software, USA). Statistical significance was considered at $p < 0.05$. Data were analyzed with One-way Anova and Tukey's correction (Gaussian distribution, n>2), Kruskal-Wallis and Dunn's correction (non-Gaussian distribution, n>2) or two-tailed Student's T-test (n=2). For permeability analysis (section 4.7), statistical analysis of linear regressions (R^2) was performed by comparing the intercept points at the Y axis.

4 RESULTS

4.1 Optimization of fabrication conditions for anisotropic scaffolds

Anisotropic scaffolds were fabricated by directional freezing and freeze-drying. Four different combinations of freezing temperatures (-20°C and -50°C) and silk fibroin solution concentrations (5% and 8% in ddH$_2$O) were tested. The effect of freezing temperature and silk fibroin concentration on pore size and morphology was evaluated. Lower freezing temperatures (-50°C) resulted in smaller pore spaces and thinner pore walls compared to higher temperatures (-20°C) (figure 9). Qualitatively, silk fibroin solution concentration did not seem to affect pore sizes. Based on these results, the temperature selected for anisotropic scaffold fabrication was -20°C. The selected silk fibroin solution concentration was 8% to increase matrix stiffness (see discussion).
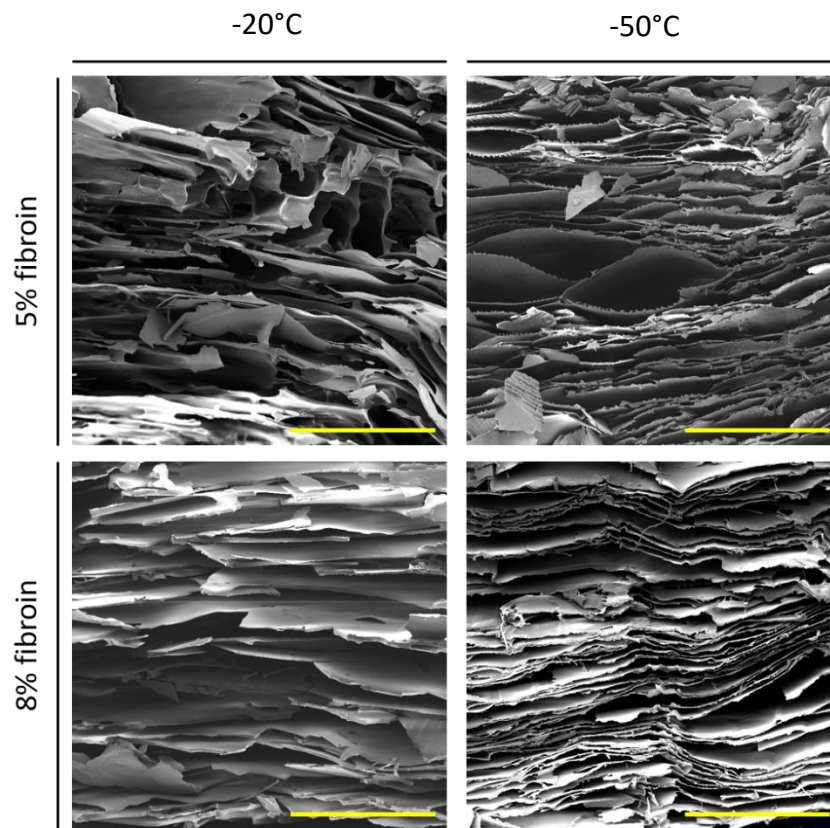
Figure 9. Effect of freezing temperature and silk fibroin solution concentration on the pore sizes of anisotropic scaffolds. Transversal sections of anisotropic scaffolds fabricated by directional freezing and freeze drying at -20 or -50°C using 5% or 8% silk fibroin solution. Images were taken after treatment with 80% methanol for 30min. Scale bars = 400µm.

4.2 Characterization of anisotropic scaffolds

FTIR characterization of anisotropic scaffolds before methanol treatment shows that fibroin presented a silk I random coil protein conformation, as indicated by the peaks at 1652 cm^{-1} and 1540 cm^{-1} and the absence of a shoulder at 1266 cm^{-1} (figure 10A). After methanol treatment, the peaks shifted to 1625 cm^{-1} (corresponding to the amide I of antiparallel beta sheet) and 1520 cm^{-1}. In addition, shoulders at 1265 cm^{-1} and 1700 cm^{-1} (characteristic of beta bends and turns) were detected. These data indicate a conformational change from the silk I to the silk II protein conformation as a consequence of methanol treatment.

Pore alignment and morphology of anisotropic scaffolds is shown in figures 10B (left panels) and 10C. The μCT 3D volume reconstruction shows an overview of pore alignment in anisotropic scaffolds (figure 10B, left, bottom panel). Pores align in the Z axis from the top to the bottom of the scaffold. The aligned pores have a lamellar-like morphology (figure 10B, top and middle panels). In the scaffold's transversal sections, it can be appreciated that pore alignment is homogeneous along the Z axis (all pores align in the same direction). In the scaffold cross-section, it can be appreciated that pore alignment in the x-y axis is less homogeneous (pores align in 2 to 3 different orientations). Figure 10C shows 3D reconstructions performed with confocal microscopy scans. Those images show the morphology and alignment of lamellar pores in more detail, until a depth of 200μm. The lamellar pore walls align parallel to each other and their thickness is <100μm.

4.3 Characterization of isotropic scaffolds

Silk fibroin scaffolds with isotropic pores were fabricated by solvent casting/particulate leaching, freezing and freeze-drying. FTIR spectra shows a peak at 1625 cm^{-1}, indicating that fibroin gelation during scaffold fabrication resulted in a silk II protein conformation (figure 10A). FESEM transversal and cross-sections show that isotropic scaffolds have round pores with rough pore walls and a highly interconnected pore architecture (figure 10B, right top/middle panels). An overview of scaffold morphology and pore distribution is shown in the μCT 3D volume reconstruction of figure 10B (right, bottom panel).
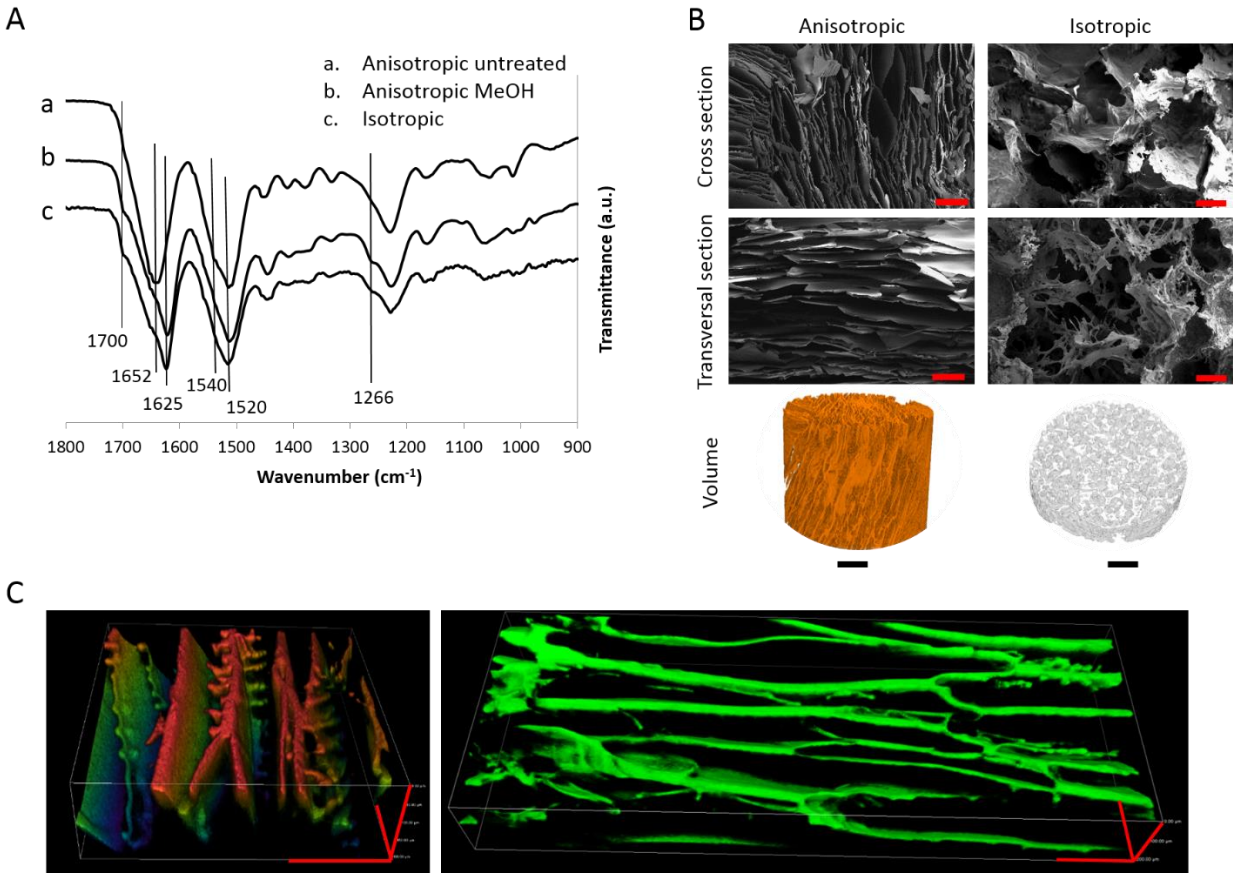
Figure 10. Characterization of silk fibroin anisotropic and isotropic scaffolds. **A)** Fourier transform infrared spectroscopy spectra of untreated anisotropic scaffolds, methanol (MeOH) treated anisotropic scaffolds and isotropic scaffolds. **B)** *Top and middle panels*: field-emission scanning electron microscopy images of transversal or cross-sections of anisotropic and isotropic scaffolds showing pore morphology and alignment. Scale bars = 200µm. *Bottom panel*: µCT 3D volume reconstructions of anisotropic and isotropic scaffolds showing an overview of scaffold and pore morphology. Scale bars = 500µm. **C)** 3D reconstructions of confocal microscopy scans showing the morphology and alignment of lamellar pores in anisotropic scaffolds. Left panel: depicted area = 600µm x 600µm x 200µm (x–y–z axis). The color code indicates the depth scale. Red corresponds to the surface and blue to the inside. Right panel: depicted area = 1700µm x 600µm x 200µm (x–y–z axis) (rhodamine staining); scale bars = 200µm. Figure from (Font Tellado et al. 2017).

4.4 Morphology of biphasic scaffolds

Biphasic silk fibroin scaffolds with anisotropic and isotropic porosity were produced following two different protocols: A and B. Figure 11 shows the appearance of type A and B biphasic scaffolds imaged with digital light microscopy. Images correspond, from left to right, to whole scaffolds (left),

scaffold transversal sections at low magnification (middle) and scaffold transversal sections at high magnification (right). In the low magnification images, it can be appreciated that the scaffolds have two different regions: the top area corresponds to the anisotropic region, while the bottom area corresponds to the isotropic region. The volume ratio between the anisotropic and isotropic areas is 1:4. The change between the anisotropic and isotropic areas can be distinguished with the naked eye. The transition between the anisotropic and isotropic areas is shown in the high magnification images. The change in porosity appears different in each type of scaffold. In scaffold A, the change between the anisotropic and anisotropic regions is sharp, while in scaffold B the two regions seem to be more integrated.
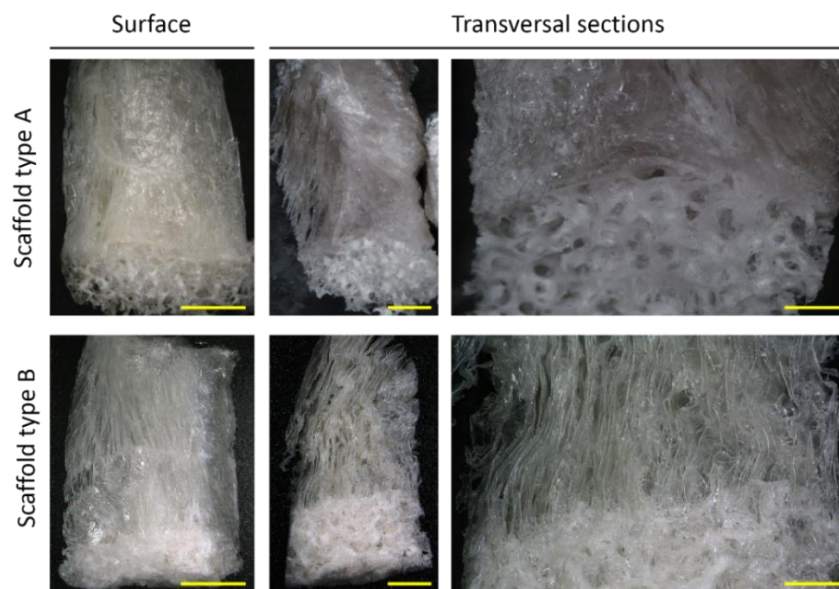

Figure 11. Morphology of biphasic scaffolds. Appearance and morphology of type A and B biphasic scaffolds shown by light microscopy. Left panels show whole scaffolds, scale bars = 2 cm. Middle panels show scaffold transversal sections (2mm thickness), scale bars = 1 cm. Right panels show transversal sections (2mm thickness) at higher magnification, scale bars = 0.5 cm. All scaffolds are positioned with the anisotropic part on the top and the isotropic part on the bottom. On the right panels the transition between the anisotropic and isotropic parts can be appreciated.

4.5 Structure and pore alignment of biphasic scaffolds

A and B fabrication protocols resulted in scaffolds with different structural characteristics, especially at the transition area between the anisotropic and the isotropic regions (figure 12). An overview of scaffold morphology and pore alignment is shown in µCT 3D volume reconstructions depicting type A and B biphasic scaffolds from different perspectives (figure 12A). The left and

middle images show scaffold and pore morphology in the anisotropic, transition and isotropic regions from different perspectives. The right image is a cross-section at the transition area.

Figure 12B shows pore morphology and alignment in more detail. In figures 12A and B it can be appreciated that the anisotropic region is similar in both types of biphasic scaffolds and consists on lamellar and vertically aligned pores, as shown for anisotropic scaffolds. On the other hand, the transition and isotropic areas present differences between scaffolds. In type A scaffolds, the isotropic area is composed of round, open pores, as shown for isotropic scaffolds. The transition between the anisotropic and isotropic areas is sharp and occupies a very thin proportion of the scaffold. In figure 12B it can be appreciated that a thin layer of solid fibroin formed at the transition point between the anisotropic and isotropic regions of type A scaffolds. On the other hand, the change from anisotropic to isotropic porosity is more progressive in scaffolds type B. Figure 12B shows how the lamellar pores of the anisotropic region of type B scaffolds penetrate the isotropic region to a certain extent, generating an extensive area of mixed porosity at the transition. As a consequence, both types of porosity are present in the transition area (figures 12A and 12B).

4.6 Porosity and pore sizes of biphasic scaffolds

Total porosity and pore sizes of type A and B biphasic scaffolds were measured in whole scaffolds or the anisotropic, transition and isotropic regions (figure 13). Each region was visually clustered along the Z axis of the scaffolds using µCT scans. Scaffold's total porosity was higher in type A scaffolds (59 ± 4%) compared to type B scaffolds (49 ± 7%) (figure 13A) (differences not statistically significant). Type A scaffolds also presented a higher proportion of big pores (18 ± 5% of pores between 301 and >500µm) compared to type B scaffolds (4.5 ± 3% of pores between 301 and >500µm) (figure 13B). Conversely, the proportion of small pores was lower in type A scaffolds (30.5 ± 6% of pores ranging <100 – 300µm) compared to type B scaffolds (45.5 ± 8% of pores ranging <100 – 300µm). Looking at the individual scaffold regions, total porosity was the highest in the isotropic part of type A scaffolds (80 ± 1.5%) (figure 13A). Accordingly, this was also the region with bigger pores (44 ± 6% of pores >500µm) (figure 13B). Total porosity in the transition and anisotropic regions of type A scaffolds as well as in all regions of type B scaffolds was similar and averaged 50% (figure 13A). Pore size distribution was also similar in those areas. On average, 80-90% of the pores ranged between <100 – 300µm, while the proportion of pores between 301 to >500µm was 10-20% (figure 13B). A statistical analysis of differences in the size and distribution of pores between type A and B scaffolds was not performed since the objective was to morphologically describe the scaffolds.
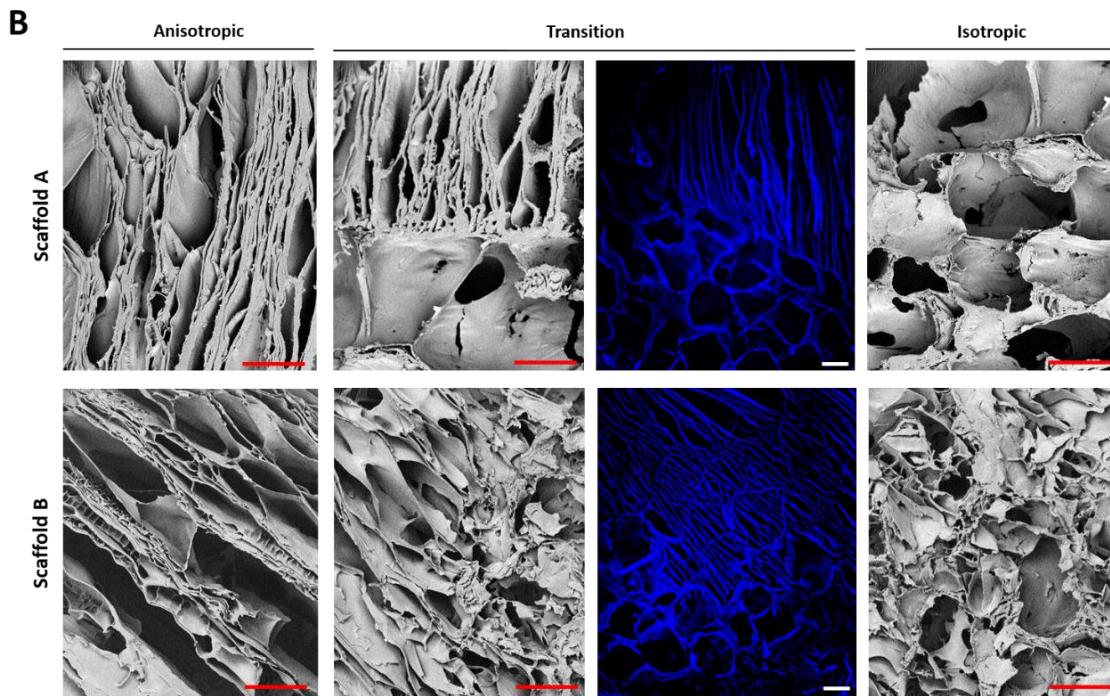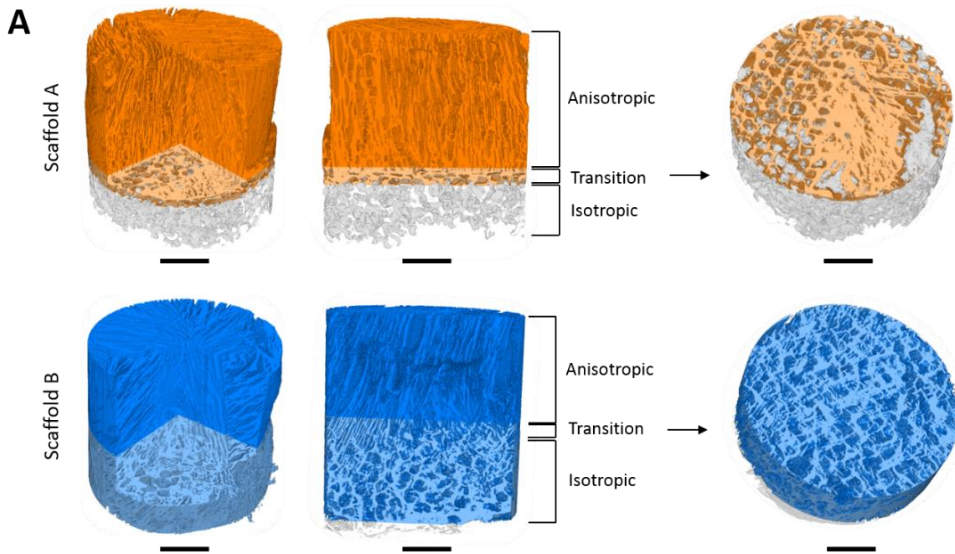
Figure 12. Characterization of silk fibroin biphasic scaffolds. **A)** µCT 3D volume reconstructions of type A and B biphasic scaffolds. The areas with anisotropic porosity are shown orange in type A scaffolds and blue in type B scaffolds. The areas with isotropic pores are shown white in A and B scaffolds. Areas with the two types of porosity (transition region) acquire a mild tone. Images correspond to (left) a whole scaffold volume with a view in the core, (middle) a long section and (right) a cross-section at the transition region. Scale bars = 500µm. **B)** Scanning electron microscopy (first, second and fourth panels) and fluorescence microscopy (third panel, DAPI staining) images of type A and B biphasic scaffolds showing pore morphology and alignment in each scaffold region (anisotropic, transition and isotropic). Scale bars = 300µm. Figure from (Font Tellado et al. 2017).

For a more accurate characterization of the distribution of porosity in biphasic scaffolds, total porosity was calculated in 1mm thick sections along the Z axis of the scaffolds using μCT (figure 13C). Type A scaffolds showed two opposite porosity gradients along the Z axis: one decreasing from the isotropic to the transition region and another one increasing from the transition to the anisotropic area. Porosity was the lowest at the transition (section 3-4 of figure 13C, scaffold A). On the contrary, porosity was more to constant along the Z axis of type B scaffolds, with values averaging 50%. The region with lowest porosity was 4 – 5 (transition area), with porosity 44 ± 8%. The regions with highest porosity was 6-7 (anisotropic area), with porosity 54 ± 10%.
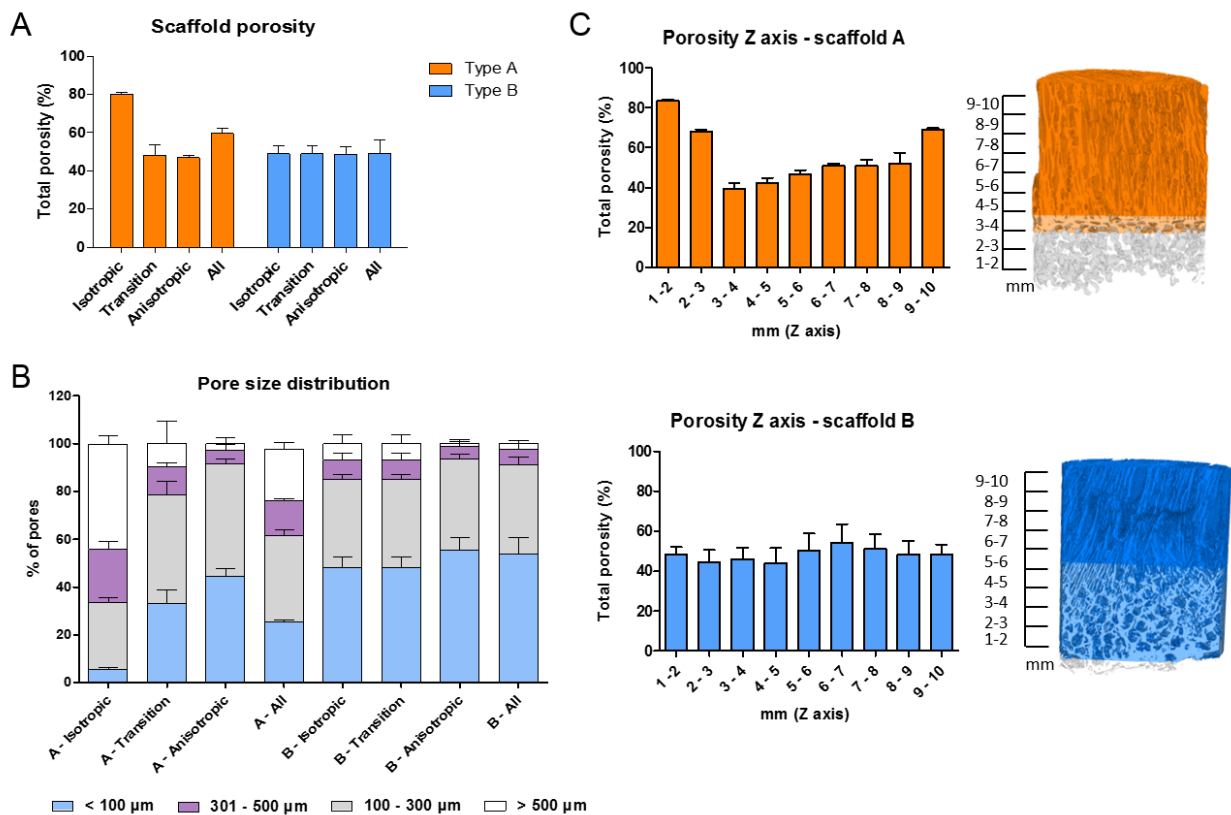

Figure 13. Porosity and pore size distribution of biphasic silk fibroin scaffolds. **A)** Total porosity of type A and B biphasic scaffolds expressed as percentage relative to the whole scaffold volume ("all") or to its separate parts (anisotropic, transition and isotropic). n=4, mean ± SEM. **B)** Distribution of pore sizes on biphasic scaffolds expressed as % of pores in a particular size range. Measurements were performed on whole scaffolds ("all") or each of its parts. n=4, mean ± SEM. **C)** Distribution of porosity along the Z axis of biphasic scaffolds. Porosity was calculated in sections of 1mm height x 7mm diameter, starting at the isotropic region. The equivalence between each section and its position in the scaffold is indicated in the images next to the bar graphs**.** n=4, mean ± SEM. Figure from (Font Tellado et al. 2017). SEM = standard error of the mean.

4.7 Permeability of biphasic scaffolds

Figure 14A shows the flow rate (Q) of PBS passing through anisotropic, type A and type B scaffolds at increasing pressure. The relationship between flow rate and pressure was linear, as indicated by the high R^2 coefficient of the linear regression (figure 14A). Scaffold permeability (K) was calculated based on flow rate and pressure (as described in section 3.9 of materials and methods) and is shown in figure 14B. All three scaffolds where permeable, allowing liquid to flow from the top to the bottom of the scaffold. Permeability was not dependent on pressure, as shown by the near-flat slope of the linear regression in figure 14B. Permeability was higher in anisotropic scaffolds compared to type A (p<0.01) and type B (p<0.001) biphasic scaffolds. Permeability of type A scaffolds was significantly higher than that of type B scaffolds (p<0.001).
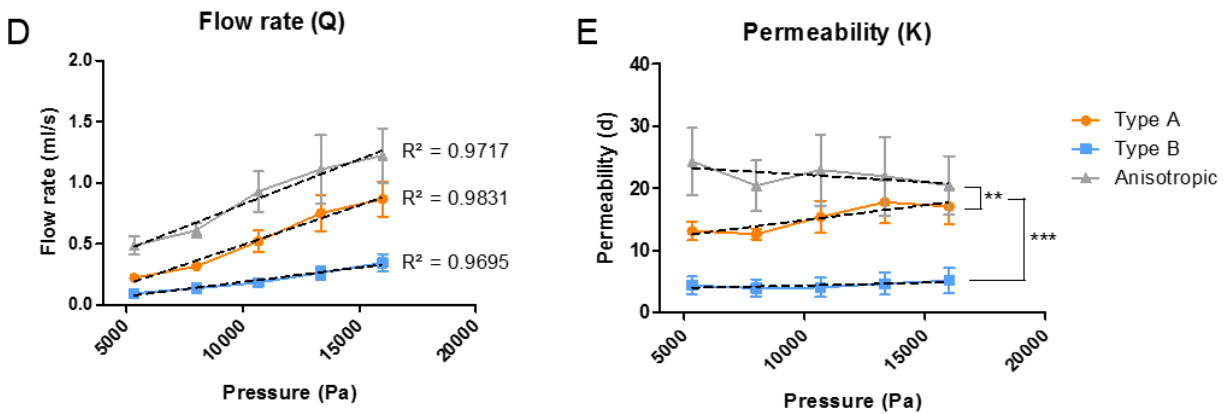
Figure 14. Flow rate and permeability of anisotropic and biphasic scaffolds. **A)** Flow rate (Q) in ml/s of PBS flowing through type A, type B or anisotropic scaffolds at increasing pressure. A linear regression was performed for each group and the correlation coefficient (R^2) is shown next to its corresponding set of values. Mean ± SEM, n=4. **B)** Permeability of type A, type B and anisotropic scaffolds at increasing pressure, expressed in darcys (d). Mean ± SEM, n=4. Statistical significance is indicated with an asterisk (**p<0.01, ***p<0.001).

4.8 Mechanical characterization of biphasic scaffolds

Anisotropic, type A and type B biphasic scaffolds were subjected to uniaxial tensile strain. The Young's modulus was calculated from the linear proportion of stress/strain curves, corresponding to values between 2-5% of strain (figure 15A). Type A scaffolds had a significantly lower Young's

modulus than type B and anisotropic scaffolds (p=0.011) (figure 15B). The Young's modulus of type B and anisotropic scaffolds was statistically not significantly different. Figure 15C shows a series of pictures of an anisotropic scaffold during the application of tensile forces. All scaffolds maintained its integrity up to 15% of strain (figures 15A and 15C). Small breaks were detected at the isotropic region in 4 out of 8 type A scaffolds. No breaks affected the transition and anisotropic areas
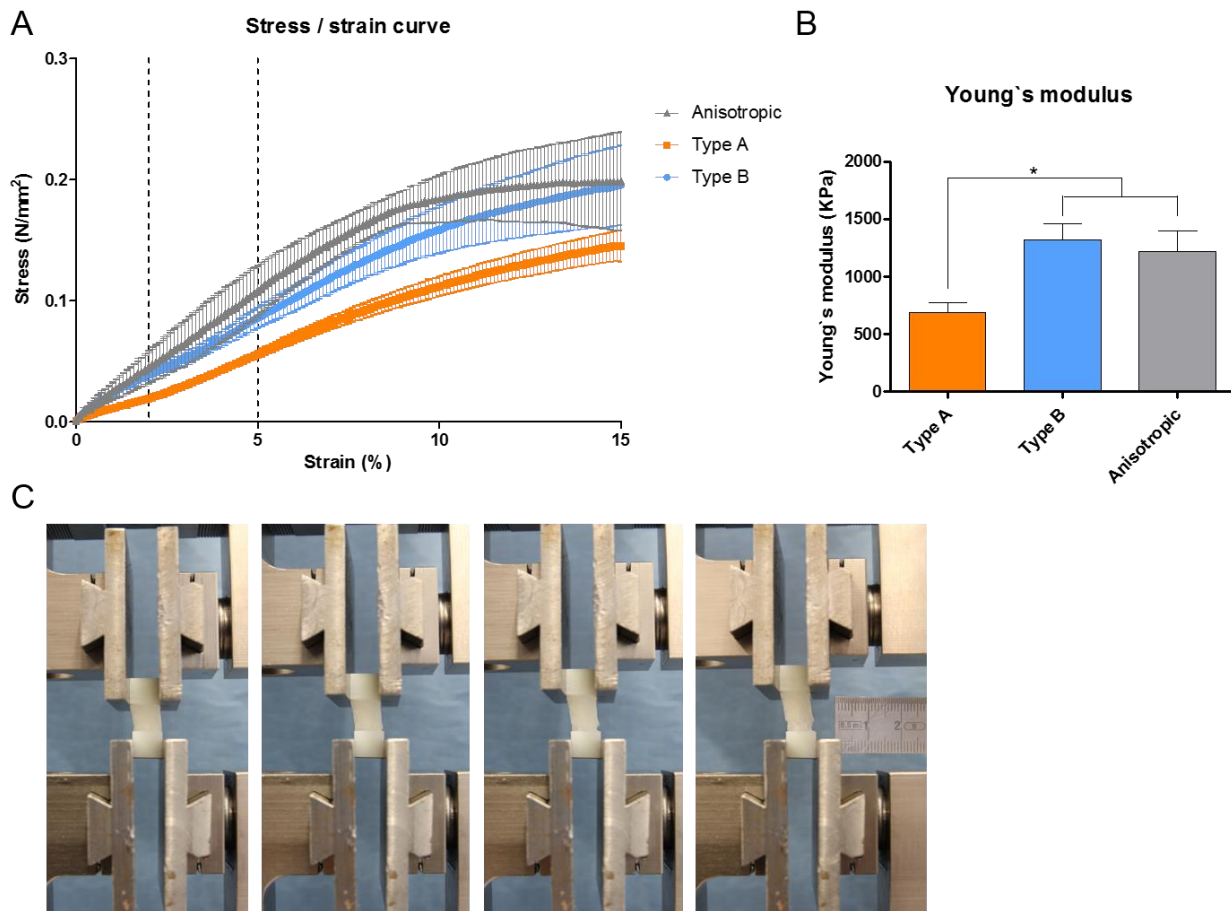

Figure 15. Tensile testing of anisotropic and biphasic scaffolds. **A)** Stress/strain curves of anisotropic, type A and type B scaffolds until a maximum of 15% strain. The linear proportion of the curves used to calculate the Young's modulus is indicated with dashed lines (2 - 5% strain). n=5, mean ± SEM. **B)** Young's modulus of anisotropic, type A and type B scaffolds. Statistical significance is indicated with an asterisk *p<0.05. n=5, mean ± SEM. **C)** Sequential images showing the elongation of an anisotropic scaffold during tensile testing from 1% to 15% of strain. Adapted from (Font Tellado et al. 2017)

4.9   Viability/cytotoxicity and proliferation of AdMSCs on biphasic scaffolds

Type A and B biphasic scaffolds did not have cytotoxic effects on AdMSCs according to LDH quantification (figure 16A) and calcein AM/hoechst staining (figure 16C). LDH values were similar for both types of biphasic scaffolds and tended to decrease over time (p<0.01) (figure 15A). An increase in LDH values between 7 and 14 days was observed for both scaffolds, but was not statistically significant. Live/dead staining corroborates these results as shown by the presence of live cells (stained green) on both types of biphasic scaffolds (figure 16C). Hoechst and Propidium Iodide (PI) staining of cells could not be detected due to high absorption of the dyes by the scaffold matrix, as shown for hoechst (figure 16C). Biphasic scaffolds did not promote cell proliferation according to dsDNA quantification data (figure 16B). dsDNA content was similar in both A and B scaffolds and stayed constant from 3 to 14 days.
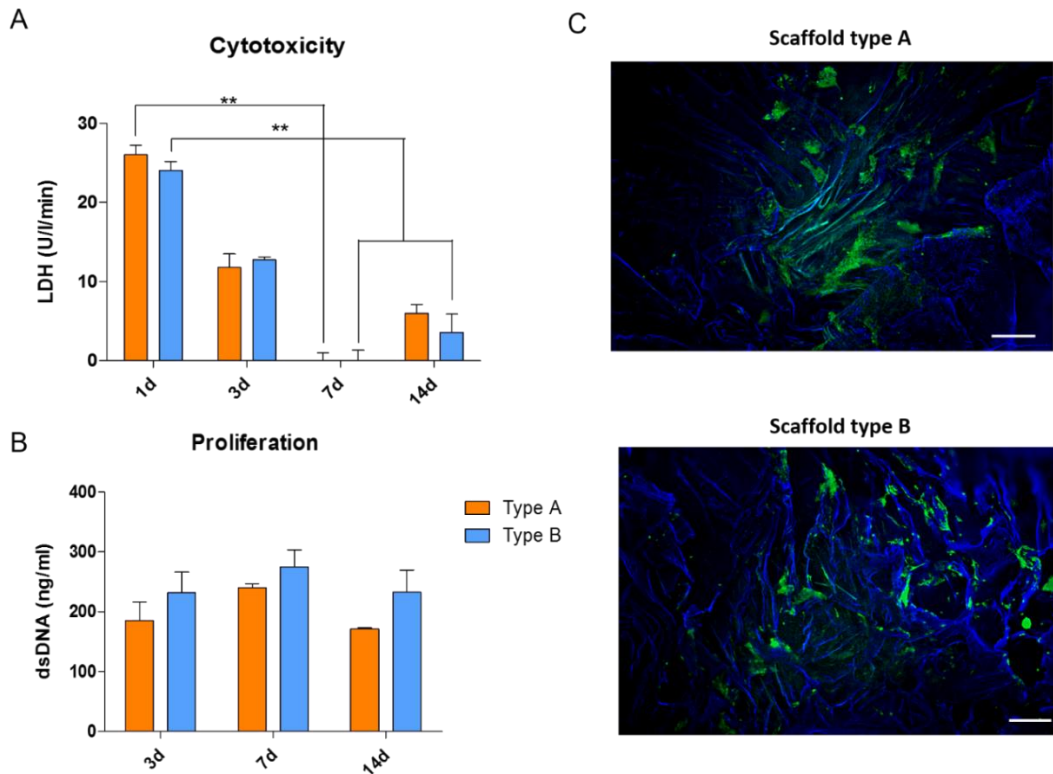

Figure 16. Cytotoxicity/viability and proliferation of AdMSCs on biphasic scaffolds. A) LDH released in the cell culture supernatant after 1, 3, 7 or 14d of culture. Statistical significance is indicated with an asterisk **p<0.01. N=3, n=9, mean ± SEM. **B)** Cell proliferation on biphasic scaffolds measured by dsDNA quantification after 3, 7 or 14d of culture. N=3, n=9, mean ± SEM. **C)** Fluorescence microscopy images showing calcein AM/hoechst staining of scaffold transversal sections after 7 days of culture. Live cells are stained green and the scaffold structure is stained blue. Scale bars = 300µm. Adapted from (Font Tellado et al. 2017).
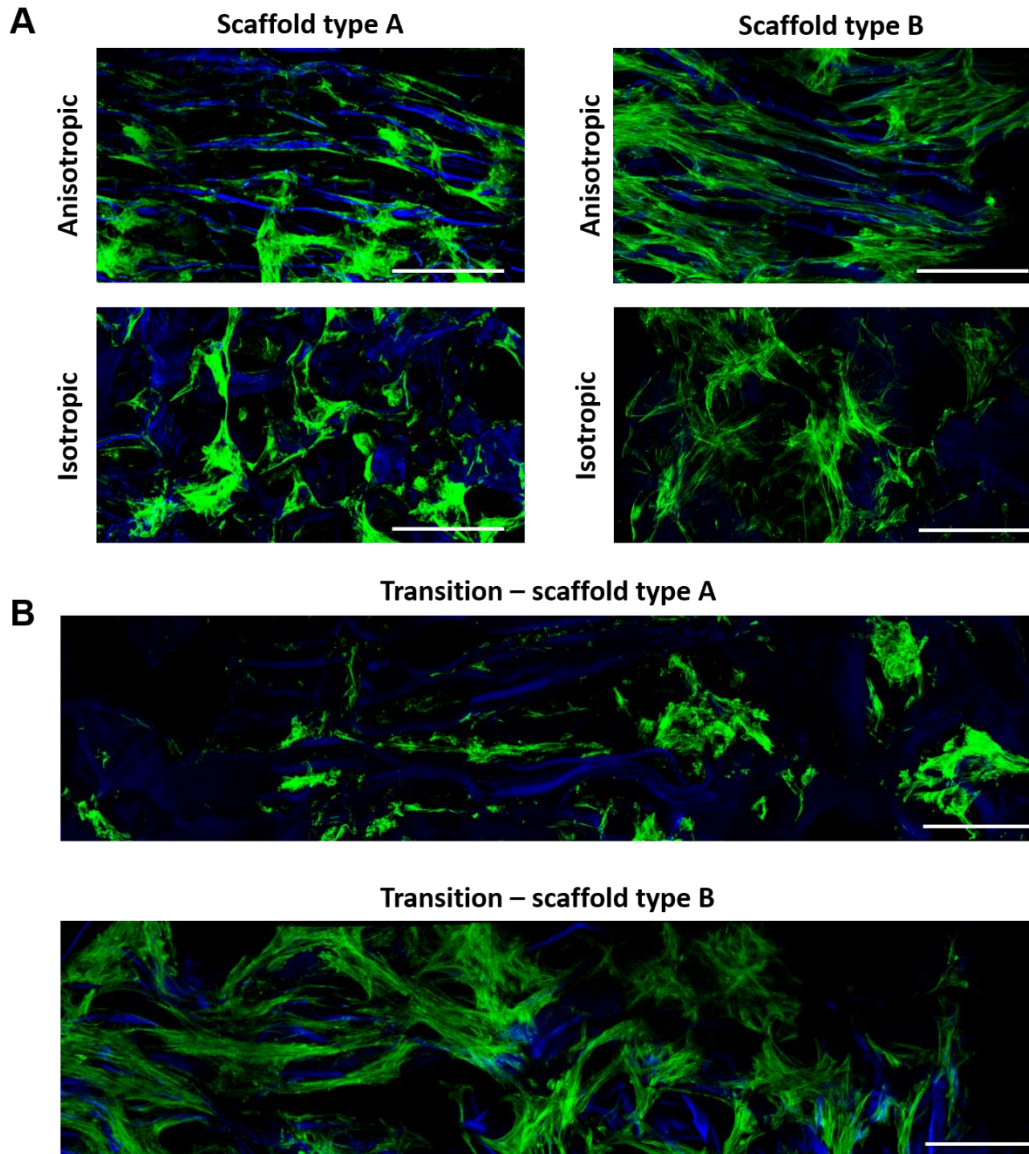
Figure 17. Morphology and cytoskeletal alignment of AdMSCs on biphasic scaffolds. Confocal microscopy images showing the actin cytoskeleton stained green (phalloidin) and the scaffold structure stained blue (DAPI). Scale bars = 300µm. **A)** Anisotropic and isotropic regions of type A and B biphasic scaffolds. In the anisotropic region cells align parallel to the scaffold's pores. In the isotropic region, cells show a spread morphology. **B)** Transition regions of type A and B scaffolds. The change in cell morphology and cytoskeleton alignment along the transition can be appreciated, especially in type B scaffolds. Adapted from (Font Tellado et al. 2017).

4.10 Morphology and cytoskeletal alignment of AdMSCs on biphasic scaffolds

The actin cytoskeleton (shown green, phalloidin staining) aligned in the direction of the scaffolds pores (figure 16). Aligned cells were observed in the anisotropic regions of type A and B scaffolds, whereas no apparent alignment was observed in the isotropic region (figure 17A). Qualitatively, cytoskeleton alignment in the anisotropic region of type B scaffolds was more pronounced compared to type A scaffolds, where some of the cells at the anisotropic region were not clearly aligned. Figure 17B shows the transition regions of type A and B scaffolds. It can be appreciated how cell morphology changes along the transition area, from aligned in the anisotropic area to non-aligned in the isotropic area. In scaffolds type B, cells populated the whole scaffold, including the transition region, where the change in cytoskeleton alignment can be appreciated. On the other hand, less cells populated the transition area of type A scaffolds, where it is more difficult to appreciate the change in cytoskeleton alignment.

4.11 Gene expression of tendon/ligament, enthesis and cartilage markers on biphasic scaffolds

AdMSCs gene expression was influenced by scaffold pore alignment in both types of biphasic scaffolds. In general, gene expression tended to increase either towards the anisotropic or the isotropic regions, with intermediate values at the transition (figure 17).

In scaffolds type A, scx expression at 7 days showed a graded pattern of expression increasing towards the isotropic region (figure 18A). Conversely, scx expression in scaffolds type B tended to increase towards the anisotropic region. Expression levels at the transition were intermediate. Scx expression levels decreased from 7 to 14 days and became similar in all regions of both type A and B scaffolds.

Collagen I (figure 18B) and collagen III (figure 18C) showed similar expression patterns. In both type A and B scaffolds, collagen I and III expression increased towards the isotropic regions at both 7 and 14 days ($p < 0.05$ in type A scaffolds). At 7 days, higher levels of collagen I and III expression were observed in type B compared to type A scaffolds, although differences were not statistically significant. At 14 days, collagen I expression tended to be higher in type B scaffolds, whereas collagen III expression tended to be higher in type A scaffolds.
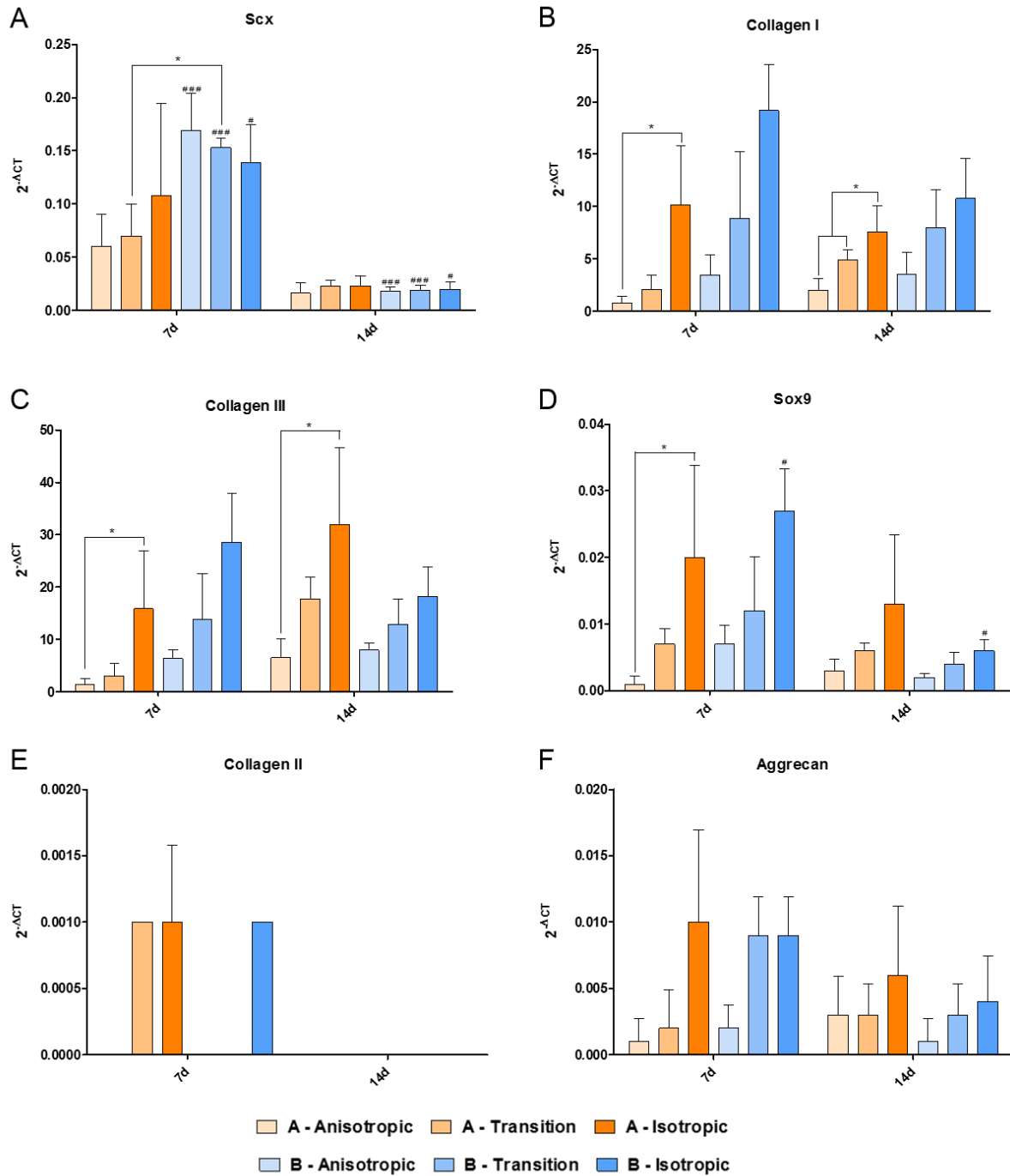
Figure 18. AdMSCs gene expression on biphasic scaffolds. Gene expression of **A)** scx, **B)** collagen I, **C)** collagen III, **D)** SRY (Sex-determining region Y)-box 9 (sox9), **E)** collagen II and **F)** aggrecan. Data is expressed as fold change respect to the housekeeper ($2^{-\Delta CT}$). N=3, n=9, mean ± SEM. Statistical significance between scaffold types (A and B) and parts of the scaffolds (anisotropic, transition, isotropic) is indicated with an asterisk *p<0.05. When comparing the 7 and 14d of a single scaffold region, statistical significance is indicated with a number symbol in top of the 7 and 14d bars #p<0.05, ###p<0.01. Adapted from (Font Tellado et al. 2017).

Sox9 expression increased towards the isotropic regions in both type A and B scaffolds ($p < 0.05$ in type A scaffolds) (figure 18D). Expression levels decreased with time from 7 to 14 days ($p < 0.05$ in type B scaffolds). Sox9 expression was higher in type B scaffolds at 7 days, whereas at 14 days it was higher in type A scaffolds (differences not statistically significant). However, expression levels in all conditions were low. Collagen II expression levels were very low and even undetectable in some scaffold regions (figure 18E). Aggrecan expression showed a similar pattern to sox9. In general, aggrecan expression tended to increase towards the isotropic regions of type A and B scaffolds (figure 18F). However, expression levels at the transition were as high as in the isotropic region of type B scaffolds at 7 days. Aggrecan expression tended to decrease from 7 to 14 days for both scaffolds in all scaffold regions.

4.12 Functionalization of type B biphasic scaffolds with heparin

Heparin was incorporated in type B biphasic silk fibroin scaffolds in the presence (heparin-crosslinked) or absence (non-crosslinked) of EDC/NHS crosslinkers. Heparin binding on scaffolds significantly increased with the use of EDC/NHS crosslinkers (figure 19A). The percentage of bound heparin was $6.0 \pm 2.3\%$ in non-crosslinked scaffolds and $29.5 \pm 4.4\%$ in crosslinked scaffolds ($p < 0.001$). After washing the scaffolds for 3 days in ddH_2O, the amount of heparin remaining bound to the scaffolds was $5.5 \pm 2.1\%$ in non-crosslinked scaffolds (corresponding to 1.6 ± 0.03mg heparin/scaffold) and $26.6 \pm 4\%$ in crosslinked scaffolds (corresponding to 8.0 ± 0.3mg heparin/scaffold) ($p < 0.001$).

Figure 19B shows heparin release in ddH_2O from non-crosslinked and heparin-crosslinked scaffolds, expressed as percentage respect to the amount of bound heparin (before washing). The amount of heparin released after 3 days averaged 9 - 10% for both heparin-crosslinked and non-crosslinked scaffolds. However, release was faster in non-crosslinked scaffolds, in which 8% of incorporated heparin was already released after 3h, compared to 6% in crosslinked scaffolds. Differences were not statistically significant. Heparin release between 3 and 7 days was negligible. Based on this result, scaffolds used for growth factor incorporation and cell culture were washed for 3 days in water to ensure complete removal of unbound heparin.
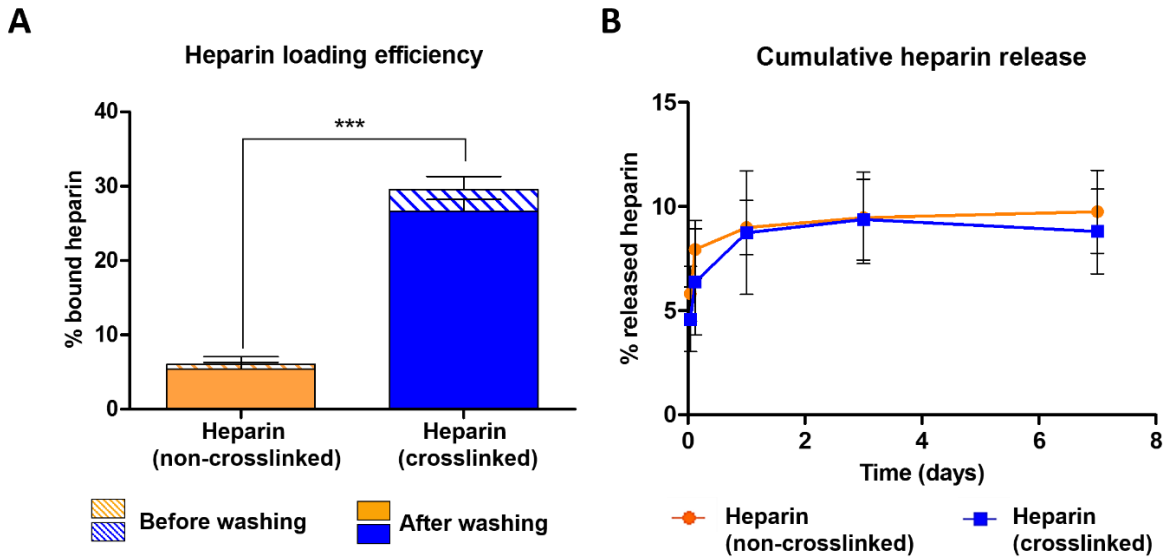
Figure 19. Heparin incorporation and release on type B biphasic scaffolds. **A)** Heparin incorporation on type B biphasic scaffolds in the presence (crosslinked) or absence (non-crosslinked) of EDC/NHS crosslinkers. The amount of incorporated heparin is shown before (patterned bars) or after (plain bars) washing the scaffolds for 3 days washing in ddH$_2$O. Data is expressed as percentage of bound heparin respect to the total heparin used for conjugation (30mg/ml). n=6, mean ± SEM. **B)** Cumulative heparin release from crosslinked and non-crosslinked scaffolds after 1h, 3h, 1d, 3d and 7d of incubation in ddH$_2$O. Data is expressed as percentage of released heparin respect to the amount of bound heparin after conjugation (before washing). n=6, mean ± SEM.

4.13 Incorporation and release of TGF-β2 and GDF5 from type B biphasic scaffolds

TGF-β2 and GDF5 were incorporated with high efficiency (>90%) on unmodified, non-crosslinked and heparin-crosslinked silk fibroin scaffolds (figures 20A and C). Incorporation efficiency of TGF-β2 averaged 94% in untreated scaffolds, 92% in non-crosslinked scaffolds and 96% in heparin-crosslinked scaffolds (figure 20A). The amount of incorporated GDF5 averaged 96% in unmodified scaffolds, 92% in non-crosslinked scaffolds and 94% in heparin-crosslinked scaffolds (figure 20C). There were no significant differences between groups.

On the other hand, growth factor release kinetics were different between groups. A higher percentage of growth factors were released from unmodified and non-crosslinked scaffolds compared to heparin-crosslinked scaffolds. 40 to 47% of TGF-β2 was released after 24h from unmodified and non-crosslinked scaffolds, whereas only 21% was released from heparin-crosslinked scaffolds (p<0.001) (figure 20B). After 14 days, up to 58% TGF-β2 was released from

58

unmodified or non-crosslinked scaffolds, while up to 26% was released from heparin-crosslinked scaffolds (p<0.001). GDF5 release followed a similar behavior, but the differences between groups were more pronounced (figure 20D). In unmodified and non-crosslinked scaffolds, up to 80% GDF5 was released after 24h. In heparin-crosslinked scaffolds, release at 24h decreased to 10% on average (p<0.001). After 14 days, up to 92% of GDF5 was released from unmodified and non-crosslinked scaffolds, whereas only 18% GDF5 was released from heparin-crosslinked scaffolds (p<0.001).
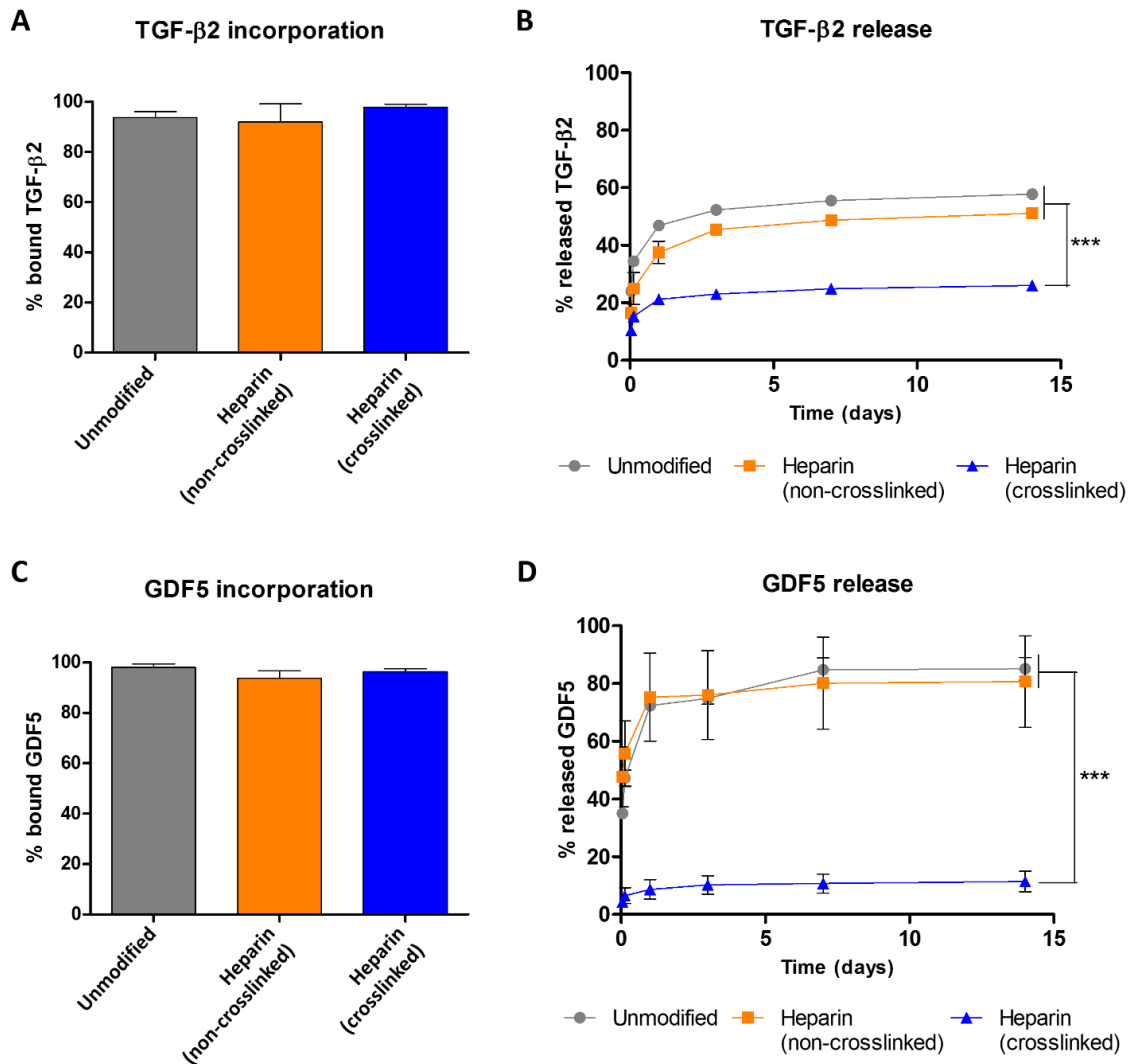

Figure 20. TGF-β2 and GDF5 incorporation and release on type B biphasic scaffolds. **A)**, **C)** Amount of TGF-β2 **(A)** and GDF5 **(C)** bound to type B biphasic scaffolds. Data is expressed as percentage of growth factor bound to the scaffolds respect to total growth factor loaded (100ng/scaffold). n=3, mean ± SEM. **B), D)** Cumulative release of TGF-β2 **(B)** and GDF5 **(D)** from type B biphasic scaffolds after 1h, 3h, 1d, 3d, 7d or 14d of incubation in AdMSCs growth medium. Data is expressed as percentage of growth factor released respect to total growth factor loaded on scaffolds for conjugation (100ng/scaffold). n=3, mean ± SEM.

4.14 Seeding efficiency and metabolic activity on heparin-functionalized and non-functionalized type B biphasic silk fibroin scaffolds

Heparin functionalization and growth factor loading did not have significant effects on the seeding efficiency of AdMSCs on type B scaffolds (figure 21A). Seeding efficiency ranged between 75 – 92% in all sorts of type B biphasic silk fibroin scaffolds (unmodified, crosslinked with heparin unloaded, or crosslinked with heparin and loaded with TGF-β2/GDF5). There were no statistically significant differences between groups. Similarly, AdMSCs metabolic activity was not significantly different in scaffolds containing heparin and/or growth factors compared to unmodified scaffolds up to 7 days of culture (figure 21B). At 3 days, AdMSCs cultured on scaffolds crosslinked with heparin (unloaded or loaded with growth factors) tended to show higher metabolic activity compared to AdMSCs cultured on unmodified scaffolds. However, differences were not statistically significant.
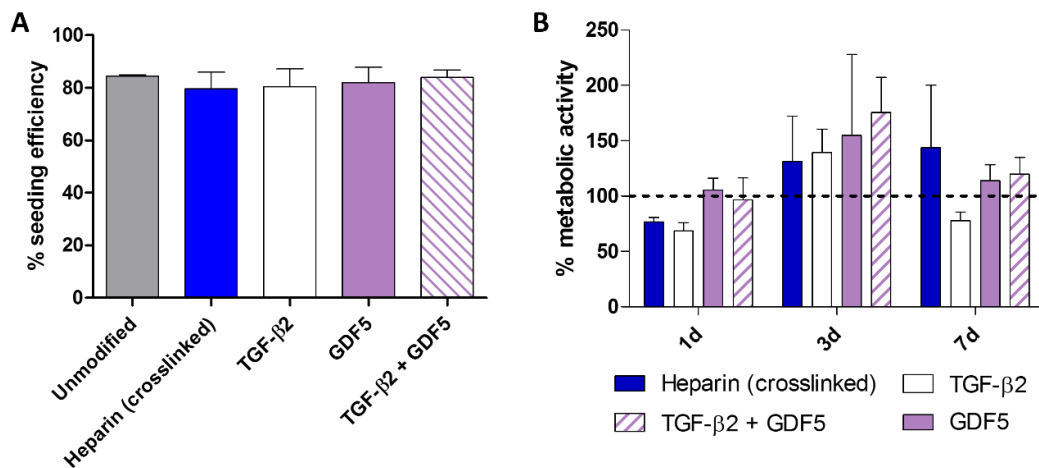

Figure 21. AdMSCs seeding efficiency and metabolic activity on type B biphasic scaffolds. **A)** Seeding efficiency of AdMSCs on type B scaffolds unmodified, crosslinked with heparin without growth factors (unloaded) or crosslinked with heparin and loaded with TGF-β2/GDF5. Data is expressed as percent metabolic activity of cells attached to the scaffolds respect to metabolic activity of total cells seeded. Metabolic activity was quantified 24h after seeding. N=3, n=9, mean ± SEM. **B)** Metabolic activity of AdMSCs grown on heparin-crosslinked scaffolds (unloaded or loaded with growth factors) expressed as percentage respect to the metabolic activity of AdMSCs grown on unmodified scaffolds. N=3, n=9, mean ± SEM.

4.15 Gene expression on heparin-functionalized type B biphasic scaffolds

AdMSCs gene expression was analyzed in type B heparin-crosslinked scaffolds unloaded or loaded with TGF-β2, GDF5 or their combination. Each scaffold region (anisotropic, transition and

isotropic) was analyzed individually. Gene expression data from growth factor-loaded scaffolds was expressed as fold change respect to unloaded scaffolds for each scaffold region.

Scx expression was not significantly different in scaffolds loaded with TGF-β2/GDF5compared to unloaded scaffolds (figure 22A). The highest upregulation (4-fold) was seen in the isotropic region of scaffolds loaded with TGF-β2 and GDF5 at 7 days compared to unloaded scaffolds.

Sox9 expression in growth factor-loaded scaffolds showed similar levels to unloaded scaffolds in most of the conditions and scaffold regions (figure 22B). At 7 days, sox9 was 3-fold upregulated in the isotropic region of scaffolds loaded with TGF-β2 and GDF5. At 14 days, sox9 was 3- to 4-fold upregulated in the anisotropic region of scaffolds loaded with TGF-β2 or with TGF-β2 and GDF5 compared to unloaded scaffolds. These differences were not statistically significant. The highest upregulation of sox9 expression happened in the transition region of scaffolds containing both TGF-β2 and GDF5 at 14 days in comparison to unloaded scaffolds (p<0.05).

Collagen I expression tended to be downregulated in growth factor-loaded compared to unloaded scaffolds at 7 days, although differences were not statistically significant (figure 22C). At 14 days, collagen I expression was 12-fold upregulated in the anisotropic region of scaffolds containing TGF-β2 compared to the same region in unloaded scaffolds. In addition, loading of scaffolds with TGF-β2 and GDF5 resulted in a significantly downregulated collagen I expression in the isotropic compared to the anisotropic and transition regions of the scaffolds (p<0.05). In the transition region of scaffolds loaded with GDF5, collagen I expression was significantly lower than in unloaded scaffolds (p<0.05).

Collagen II expression was 3-fold upregulated at 7 and 14 days in the isotropic region of scaffolds loaded with TGF-β2 and GDF5 compared to the same region in unloaded scaffolds (figure 22D). In addition, collagen II expression was upregulated in the anisotropic area of scaffolds loaded with GDF5 or TGF-β2 and GDF5 (p<0.05). Collagen II expression at 14 days was also 3-fold upregulated in the transition region of scaffolds loaded with TGF-β2.

Mohawk expression showed a similar pattern to collagen I. Mohawk expression in growth factor-loaded scaffolds at 7 days was either downregulated or similar to unloaded scaffolds. At 14 days, mohawk was 3-fold upregulated in the anisotropic region of scaffolds containing TGF-β2 and 6-fold upregulated in the transition region of scaffolds containing TGF-β2 and GDF5 (figure 22E). In addition, mohawk expression was downregulated in the isotropic region of scaffolds loaded with TGF-β2 and GDF5 at 7 and 14 days. Differences were not statistically significant.
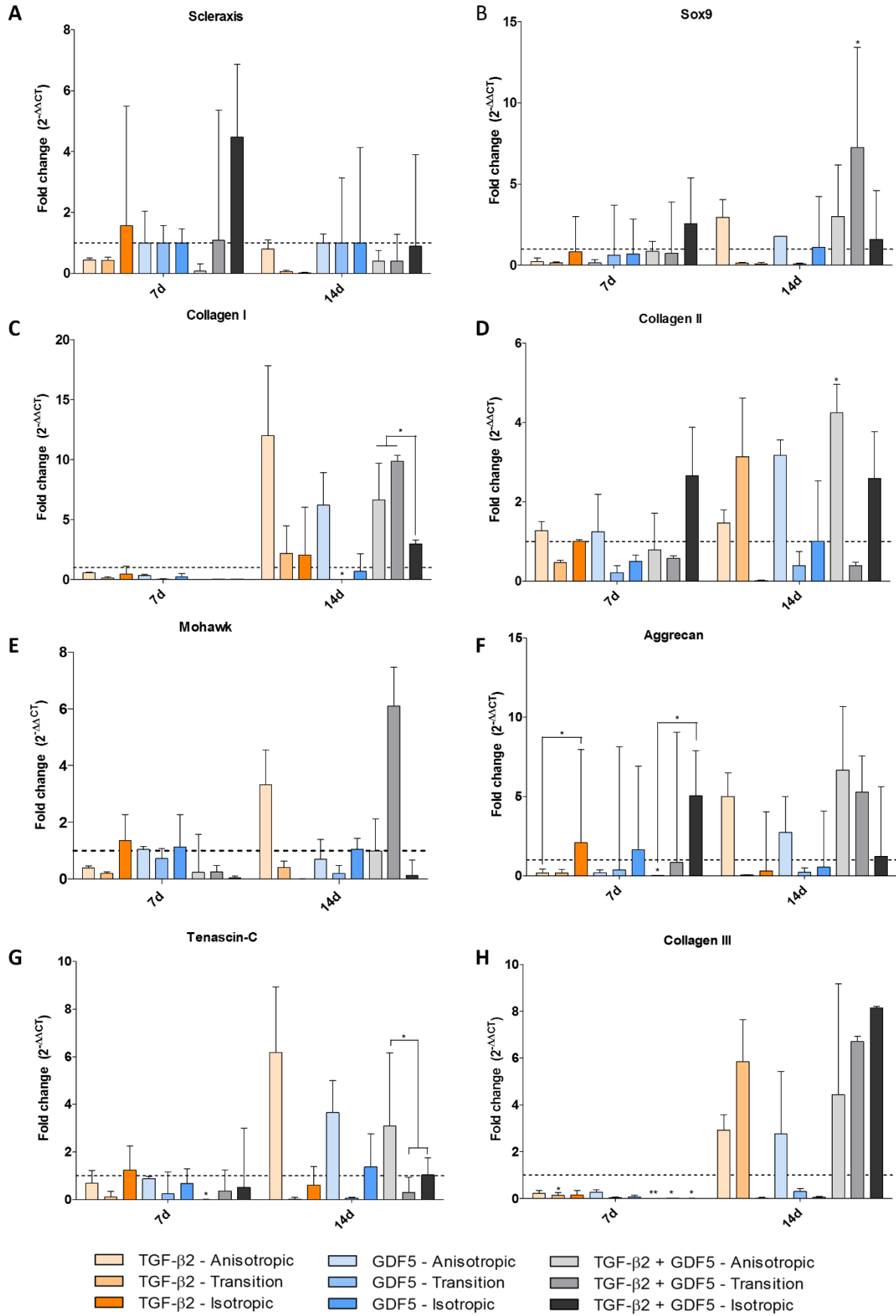
A — Scleraxis
B — Sox9
C — Collagen I
D — Collagen II
E — Mohawk
F — Aggrecan
G — Tenascin-C
H — Collagen III

Legend:
TGF-β2 - Anisotropic
TGF-β2 - Transition
TGF-β2 - Isotropic
GDF5 - Anisotropic
GDF5 - Transition
GDF5 - Isotropic
TGF-β2 + GDF5 - Anisotropic
TGF-β2 + GDF5 - Transition
TGF-β2 + GDF5 - Isotropic

Figure 22. Gene expression of tendon/ligament, enthesis and cartilage markers on heparin-functionalized type B biphasic scaffolds. AdMSCs gene expression of **A)** scx, **B)** SRY(sex-determining region Y)-box 9 (sox9), **C)** collagen I, **D)** collagen II, **E)** mohawk, **F)** aggrecan, **G)** tenascin-C and **H)** collagen III**.** Gene expression data of scaffolds loaded with TGF-β2, GDF5 or their combination is expressed as fold change ($2^{-\Delta\Delta CT}$) respect to the housekeeper (β-Tubulin) and to gene expression levels in unloaded scaffolds (dashed line). All scaffolds are heparin-crosslinked. Statistical significance is indicated with an asterisk *p<0.05, **p<0.01. Asterisks on top of a bar indicate statistical significance compared to the same scaffold region in unloaded scaffolds. N=3, n=9, mean ± SEM.

Aggrecan expression was upregulated in the isotropic region of scaffolds loaded with growth factors (all conditions) compared to the anisotropic and transition regions of the same scaffolds at 7 days (figure 22F). Differences were statistically significant when comparing the anisotropic and isotropic regions of scaffolds loaded with TGF-β2 or TGF-β2 and GDF5 (p<0.05). In addition, aggrecan expression in the anisotropic region of scaffolds loaded with TGF-β2 and GDF5 was significantly downregulated compared to the same region in unloaded scaffolds (p<0.05). On the contrary, aggrecan expression at 14 days tended to be upregulated in the anisotropic regions of growth factor-loaded scaffolds compared to unloaded scaffolds, although differences were not statistically significant.

Tenascin C expression followed a similar tendency to the other tendon/ligament markers, collagen I and mohawk. At 7 days, tenascin C expression levels in growth factor-loaded scaffolds were either similar or lower than in unloaded scaffolds (figure 22G). Tenascin C expression was significantly downregulated in the anisotropic part of scaffolds loaded with TGF-β2 and GDF5 compared to unloaded scaffolds (p<0.05). On the other hand, at 14 days tenascin C was upregulated in the anisotropic region of scaffolds loaded with growth factors (all conditions) compared to unloaded scaffolds. In addition, in scaffolds loaded with TGF-β2 and GDF5, tenascin C was significantly upregulated in the anisotropic compared to the transition and isotropic regions.

Collagen III expression was downregulated in growth factor-loaded scaffolds compared to unloaded scaffolds at 7 days (figure 22H). Differences were statistically significant at the transition region of scaffolds loaded with TGF-β2 (p<0.05) and in all regions of scaffolds loaded with TGF-β2 and GDF5 (p<0.05, p<0.01). At 14 days, collagen III expression was 3 to 5-fold upregulated in the anisotropic region of scaffolds loaded with growth factors (all conditions) compared to unloaded scaffolds. In addition, collagen III was also upregulated in the transition region of scaffolds containing TGF-β2 (6-fold) or TGF-β2 and GDF5 (7-fold) and in the isotropic region of scaffolds containing TGF-β2 and GDF5 (8-fold). Differences were not statistically significant.

4.16 Collagen I, II and III protein content on heparin-functionalized type B scaffolds

Figures 23, 24 and 25 show immunofluorescence staining of collagens type I, II and III, respectively, on heparin-crosslinked type B scaffolds. Collagen molecules are stained green, the scaffold matrix blue and the actin cytoskeleton red. The left panels show low magnification images of whole scaffold transversal sections. The middle and right panels show high magnification images of the anisotropic and isotropic regions of the scaffolds, where the cytoskeletal alignment of AdMSCs can be appreciated. Those images show how the cell cytoskeleton aligns in the direction of the scaffold's pores. Cells are elongated and aligned in the anisotropic region, whereas no alignment is apparent in the isotropic region (figures 23, 24 and 25).

Collagen I content is shown in figure 23. Looking at the scaffolds' transversal sections it can be appreciated that collagen I is more abundant in the scaffold containing TGF-β2 compared to the other groups. In that scaffold, collagen I is more abundant in the outer parts of the anisotropic and isotropic regions compared to the inner region (core). Collagen I protein clusters can be observed in the regions of higher protein content. These correspond to cell clusters, as it can be observed in the high magnification image of the anisotropic region of the TGF-β2 scaffold. Collagen I levels appeared similar in unloaded scaffolds and scaffolds containing GDF5 or TGF-β2 and GDF5.

Collagen II content is shown in figure 24. The scaffold containing GDF5 shows more abundant collagen II staining compared to the other groups. In that scaffold, collagen II concentrates at the anisotropic and isotropic regions. The scaffold containing TGF-β2 and GDF5 shows more abundant collagen II staining than the unloaded and TGF-β2 groups. In the TGF-β2 and GDF5 scaffold, collagen II is mostly localized at the transition and isotropic regions. Collagen II content seems to decrease from the transition to the anisotropic area, and can no longer be detected in the outer part of the anisotropic region. In the unloaded group, collagen II concentrates at the isotropic region. The scaffold containing TGF-β2 shows the lowest collagen II content among groups.

Collagen III content is shown in figure 25. Collagen III content appears to be the highest in the scaffold loaded with TGF-β2 and GDF5. Collagen III molecules were detected throughout the whole scaffold, but seem to be more abundant in the anisotropic and transition regions. Collagen III and cell clusters can be observed especially at the transition area and at the anisotropic area close to the transition. On the contrary, collagen III molecules in the unloaded, TGF-β2 and GDF5 groups were mostly localized in the isotropic region. Collagen III levels appeared to be similar in those three groups.
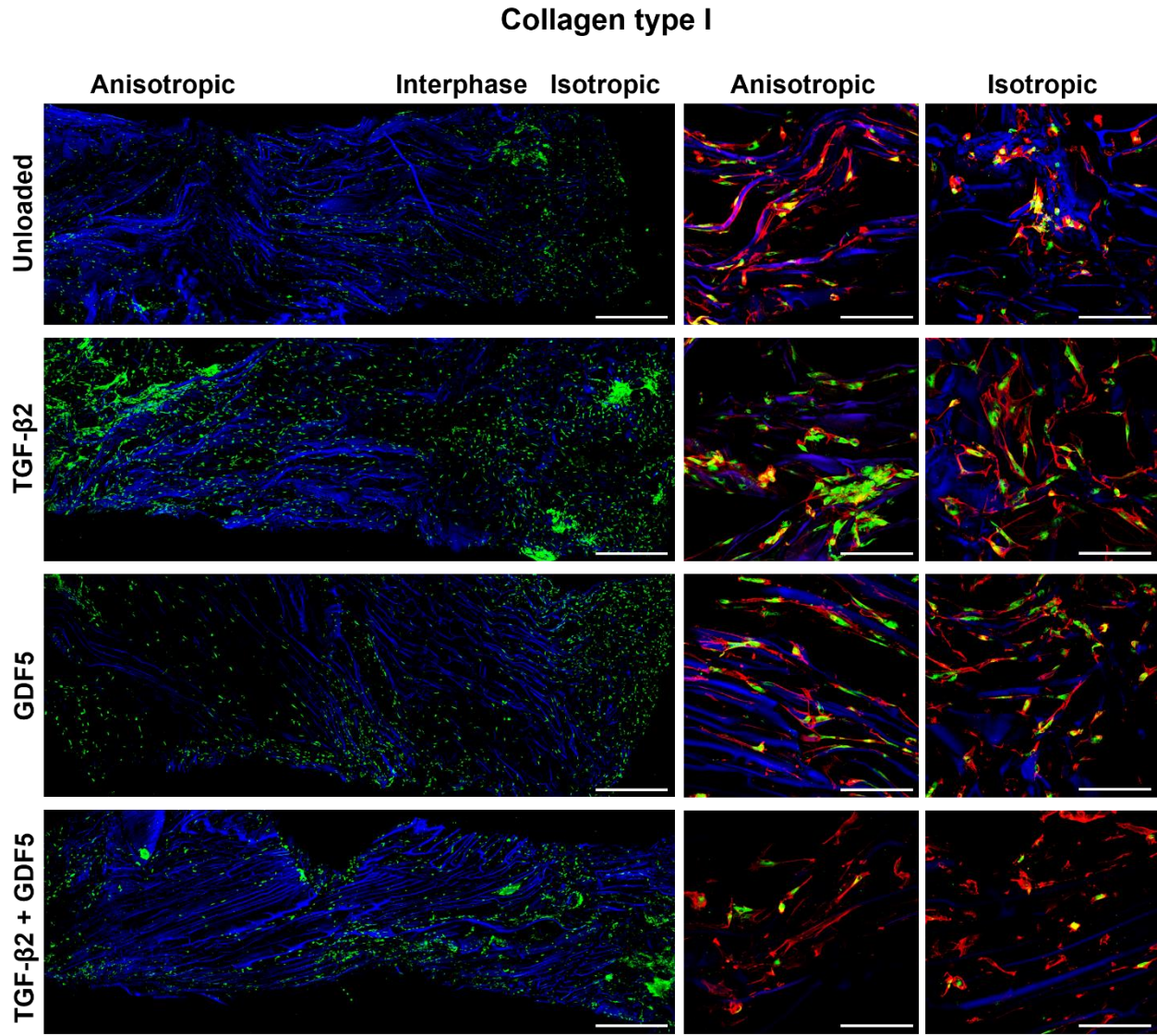
Collagen type I

Figure 23. AdMSCs cytoskeletal alignment and collagen I protein content on heparin-functionalized type B biphasic scaffolds. *Left panels:* Transversal sections of heparin-crosslinked type B biphasic scaffolds unloaded or loaded with TGF-β2, GDF5 or their combination (14 days of culture). Collagen I is stained green and the scaffold matrix is stained blue (DAPI). Scale bars = 1mm. *Middle and right panels:* Higher magnification images from the anisotropic and isotropic regions of the scaffolds shown in the corresponding left panels. Collagen I is stained green, the scaffold structure is stained blue (DAPI) and the actin cytoskeleton is stained red (phalloidin). Scale bars = 200µm. The images are 2D projections of 3D confocal images performed at different position in the Z-axis. For low magnification images, 10-15 stacks (50µm each) were taken. For high magnification images, 35 – 45 stacks (4.6µm each) were taken.
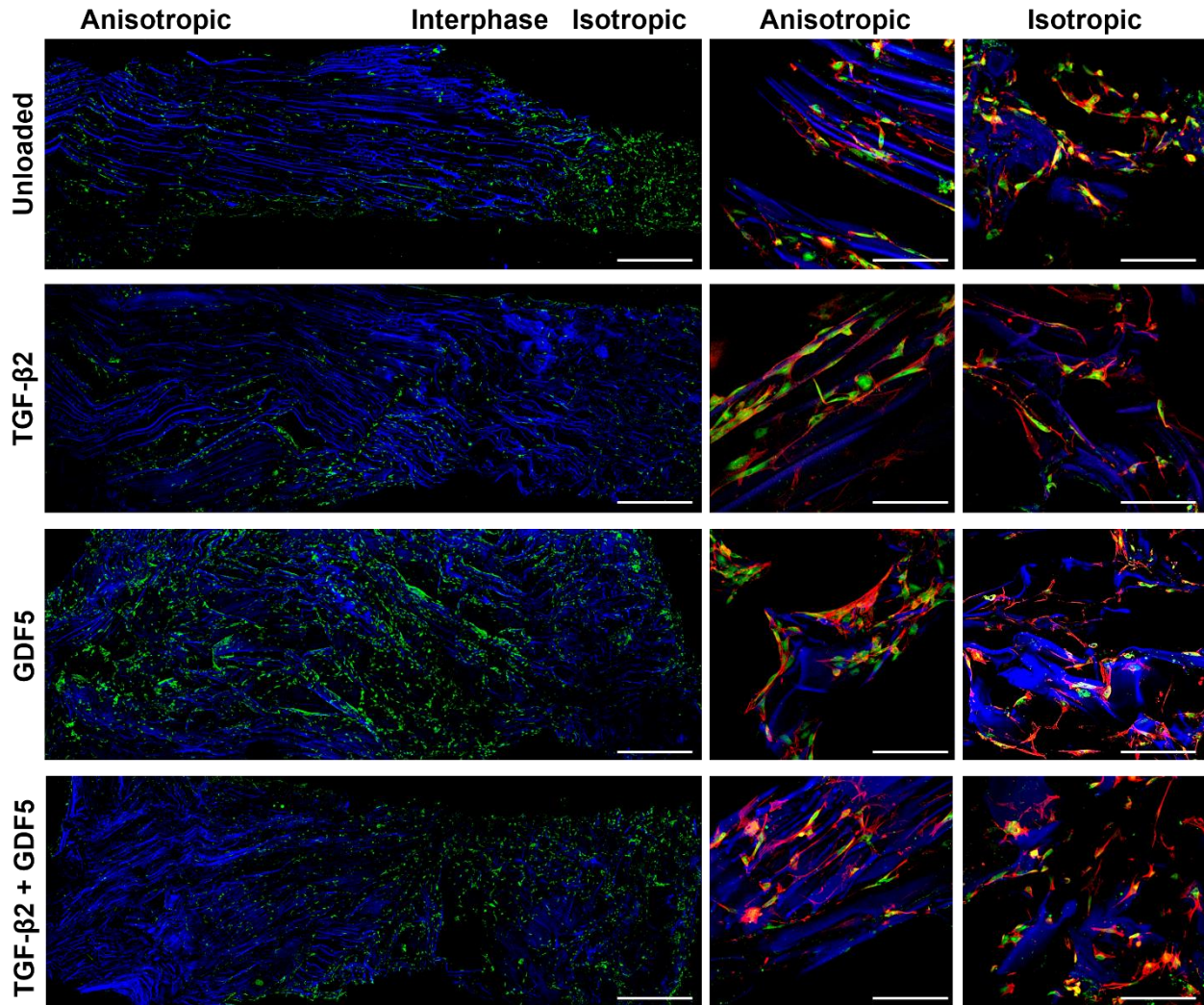
Collagen type II

Figure 24. AdMSCs cytoskeletal alignment and collagen II protein content on heparin-functionalized type B biphasic scaffolds. *Left panels:* Transversal sections of heparin-crosslinked type B biphasic scaffolds unloaded or loaded with TGF-β2, GDF5 or their combination (14 days of culture). Collagen II is stained green and the scaffold matrix is stained blue (DAPI). Scale bars = 1mm. *Middle and right panels:* Higher magnification images from the anisotropic and isotropic regions of the scaffolds shown in the corresponding left panels. Collagen II is stained green, the scaffold structure is stained blue (DAPI) and the actin cytoskeleton is stained red (phalloidin). Scale bars = 200µm. The images are 2D projections of 3D confocal images performed at different position in the Z-axis. For low magnification images, 10-15 stacks (50µm each) were taken. For high magnification images, 35 – 45 stacks (4.6µm each) were taken.
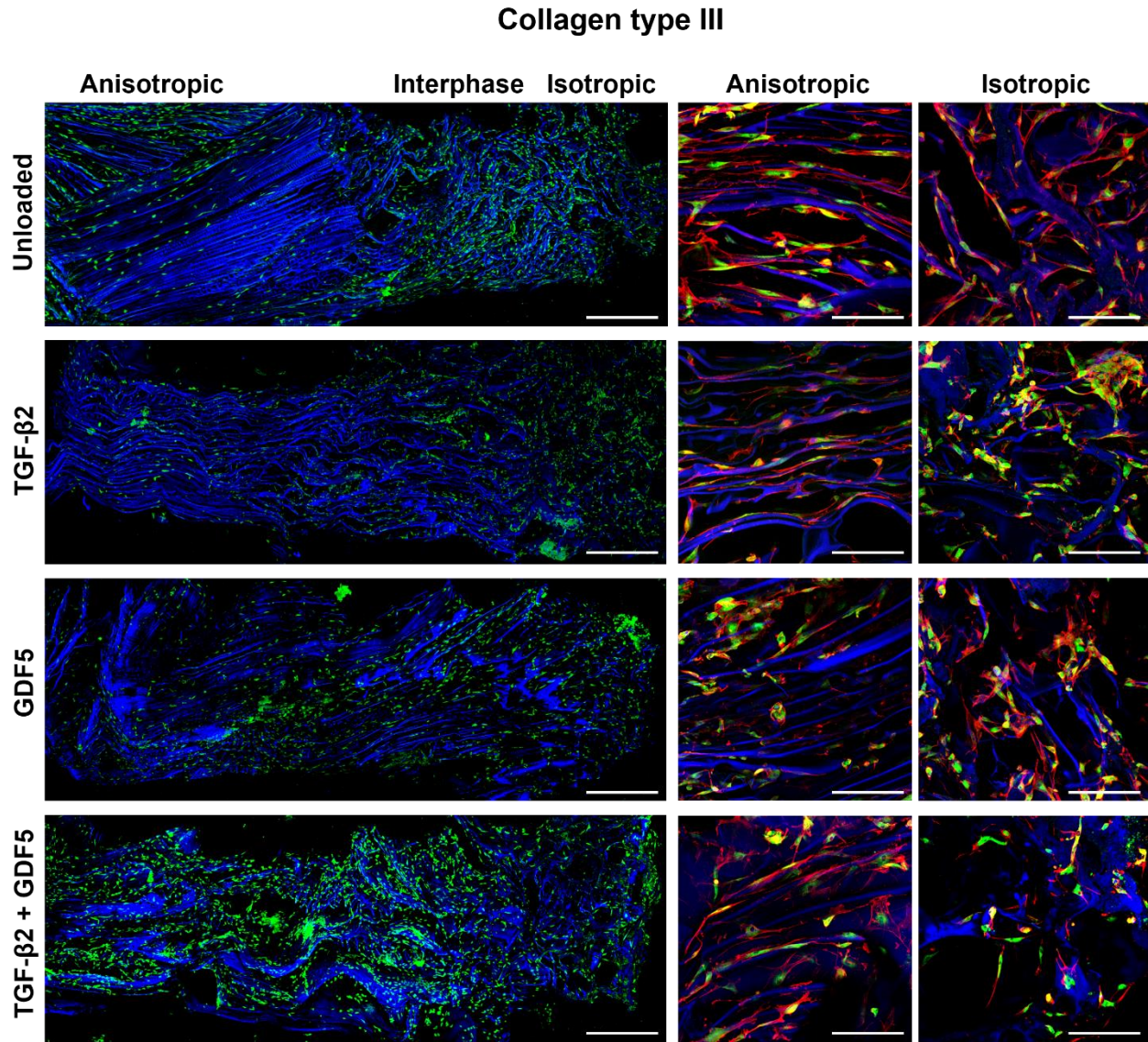
Collagen type III

Figure 25. AdMSCs cytoskeletal alignment and collagen III protein content on heparin-functionalized type B biphasic scaffolds. *Left panels:* Transversal sections of heparin-crosslinked type B biphasic scaffolds unloaded or loaded with TGF-β2, GDF5 or their combination (14 days of culture). Collagen III is stained green and the scaffold matrix is stained blue (DAPI). Scale bars = 1mm. *Middle and right panels:* Higher magnification images from the anisotropic and isotropic regions of the scaffolds shown in the corresponding left panels. Collagen III is stained green, the scaffold structure is stained blue (DAPI) and the actin cytoskeleton is stained red (phalloidin). Scale bars = 200µm. The images are 2D projections of 3D confocal images performed at different position in the Z-axis. For low magnification images, 10-15 stacks (50µm each) were taken. For high magnification images, 35 – 45 stacks (4.6µm each) were taken.

5 DISCUSSION

Integration between soft and hard tissues is of clinical importance for the repair of ruptured tendons or ligaments to bone. However, soft-to-hard tissue fixation remains a challenge in orthopedics. Current surgical treatments, based on autologous tendon transplantation, do not support the regeneration of the tendon/ligament-to-bone transition (enthesis). As a consequence, mechanical stresses accumulate at the fixation point between soft grafts and hard tissue. This increases re-rupture rates and compromises tissue functionality and long-term clinical outcome. Thus, there is a need to develop new treatments for tendon/ligament-to-bone regeneration.

This work proposes a new approach for soft-to-hard tissue repair based on the fabrication and *in vitro* culture of biomimetic and integrated tendon/ligament-to-bone tissue engineered constructs. The constructs consist of continuous and interconnected tendon/ligament-like, enthesis-like and cartilage/bone-like regions that mimic native tissue structural features. In particular, tendon/ligament-to-bone constructs were designed to mimic the change in collagen molecule alignment (from aligned in the tendon/ligament to non-aligned in the bone) of the native enthesis. The tendon/ligament part of the scaffolds had anisotropic (aligned) pores, whereas the cartilage/bone part had isotropic (non-aligned) pores. The interface consisted on a region of mixed porosity that integrated the anisotropic and isotropic regions.

Silk fibroin proved to be a suitable material for the fabrication of biocompatible and mechanically stable constructs using mild, aqueous conditions. Scaffold fabrication in aqueous conditions avoided solvent-related cytotoxicity and facilitated the incorporation of therapeutic molecules (Rockwood et al. 2011; Bessa, Balmayor, Azevedo, et al. 2010; Bessa, Balmayor, Hartinger, et al. 2010). The tendon/ligament-to-bone constructs were characterized and evaluated *in vitro* with human AdMSCs. Focus areas were the design, characterization and functionalization of biomimetic scaffolds and the evaluation of the effects of structural and biochemical cues delivered by the scaffolds on AdMSCs.

5.1 Effect of fabrication parameters on the structural properties of anisotropic and isotropic silk fibroin scaffolds

The structural characteristics of the scaffolds (pore size, pore morphology, pore alignment and matrix stiffness), were experimentally optimized by tailoring the fabrication conditions. Scaffold

features could be easily tailored but only to a certain extent, since different fabrication parameters influenced structural features simultaneously.

For the anisotropic part of the scaffolds, pore size and alignment were determined by the freezing kinetics, since pores are negative replica of the ice crystals formed during freezing. Lower freezing temperatures resulted in faster freezing and thus smaller pores. This can be explained by the physics of ice crystal formation. The ice tip radius is determined by the magnitude of supercooling ahead of the freezing front (Deville et al. 2006). The magnitude of supercooling is defined by the cooling rate. Faster cooling rates (at lower freezing temperatures) result in larger supercooling, smaller ice crystals and thus smaller pores (Deville, Saiz, and Tomsia 2006). This explains the presence of larger pores when freezing at -20 compared to -50°C. On the other hand, total porosity is independent of cooling rate but directly dependent on the concentration of the solution. Less concentrated solutions (with more water content) result in higher total porosity, but do not affect pore sizes (Deville, Saiz, and Tomsia 2006). This explains the similarity in pore sizes when comparing scaffolds produced using 5% or 8% silk fibroin solution. Furthermore, silk fibroin concentration and cooling rate also have a direct influence on the scaffold's mechanical properties, since both total porosity and pore morphology affect stiffness. More concentrated solutions (lower porosities) and faster cooling rates (smaller pores) result in stiffer matrices (Deville, Saiz, and Tomsia 2006). Taking that into account, samples were frozen at -20°C to maximize pore sizes and 8% fibroin solution was used to find a compromise between porosity and mechanical strength.

Pore anisotropy is a direct consequence of directional and dendritic ice crystal growth. A preferential growth direction of ice crystals was induced by the presence of a temperature gradient from the top to the bottom of the samples. The first ice crystal nuclei formed at the coldest region of the samples (the surface) and grew vertically in the direction of the temperature gradient. This resulted in ice crystals with homogeneous morphology and without any side branches (Oliveira et al. 2012), and explains the homogeneous pore alignment observed in the z-axis of the scaffolds. On the other hand, the presence of different orientations in the x-y-axis can be explained by the nucleation of ice crystals starting from more than one nuclei. Each group of lamellae oriented in a particular direction corresponds to a group of ice crystals derived from the same nucleus.

For the isotropic part of the scaffolds, pore morphology and size were determined by the size and type of the particles used as porogen. NaCl particles of size 400 - 800μm were used to obtain pores in the range of 200 - 400μm. Pore sizes were expected to be smaller than the particles used because of the partial dissolution of NaCl in an aqueous environment (Correia et al. 2012).

5.2 Structural properties of biphasic silk fibroin scaffolds in relation to fabrication protocol

Biphasic tendon/ligament-to-bone constructs were fabricated following two different protocols: A and B. The scaffolds resulting from both protocols were evaluated according to the integration between the anisotroic and isotropic parts, the structural characteristics of the transition region, the scaffold's mechanical properties and cell responses.

The transition region was clearly different in both scaffolds. In scaffolds type A, the anisotropic and isotropic regions were separated by a layer of solid fibroin. This can be explained by the fabrication protocol. Anisotropic scaffolds were placed on top of a mixture of silk fibroin solution and NaCl particles. At the point of contact between anisotropic scaffolds and fibroin solution, a thin fibroin layer formed as a consequence of fibroin gelation. On the contrary, the transition from anisotropic to isotropic pore alignment was more progressive in type B scaffolds and consisted of an extensive area of mixed porosity. This can be explained by the partial penetration of silk fibroin solution into the isotropic region during the fabrication of type B scaffolds. This type of structure is interesting for tendon/ligament-to-bone tissue engineering because the change in pore alignment is more gradual and keeps the two parts interconnected.

Both types of biphasic scaffolds had an interconnected pore architecture, as demonstrated by permeability analysis. The presence of an interface region in biphasic scaffolds slowed liquid flow in comparison to homogeneous (anisotropic) scaffolds, but did not compromise permeability. Total porosity and the distribution of pore sizes were different in both types of biphasic scaffolds. In type A scaffolds, pore size and porosity were the highest in the isotropic region due to its open and round pores. This can explain the higher permeability of type A compared to type B scaffolds. Of note, the μCT scans used to calculate pore sizes are perpendicular to the z axis of the scaffolds. Thus, pore sizes are measured on the x-y axis. For isotropic pores with round shape, pore sizes can be expected to be homogeneous in the x-y-z axes. However, for lamellar pores, the reported pore sizes correspond to the lamellar spaces in the x-y axis, but not to the lamellar length in the z-axis.

Interestingly, type A scaffolds showed two opposite porosity gradients along the z-axis: one decreasing from the isotropic region towards the transition and another one increasing from the transition towards the anisotropic region. This could be explained by the penetration of silk fibroin solution into the anisotropic region of type A scaffolds by capillarity during the production phase. The lamellar pores, especially at the region closer to the transition, were partially filled with fibroin

solution, generating a porosity gradient from the transition towards the anisotropic region. In addition, the formation of a solid fibroin layer in the transition contributed to reduce pore sizes and porosity in that area. In type B scaffolds, both porosity and pore size were similar in all scaffold regions and comparable to the anisotropic region of type A scaffolds. This can be explained by the penetration of lamellar pores (smaller in size) into the isotropic region of type B scaffolds. Porosity and pore size values were in the same range to the ones obtained by Correia et al. (2012), who fabricated silk fibroin scaffolds using the methodologies of directional freezing and solvent casting/particulate leaching.

Porosity and pore size gradients are interesting for tendon/ligament-to-bone tissue engineering. On the one hand, pore size has been shown to directly influence the gene and protein expression of MSCs (Di Luca et al. 2016; Oh et al. 2010; Woodfield et al. 2005). On the other hand, total porosity and pore size influence other important parameters such as the scaffold's mechanical properties and diffusion of oxygen and nutrients. Combined gradients of pore size, stiffness and oxygen/nutrient diffusion along the scaffolds could promote site-specific cell differentiation and recapitulate the gradual change in cell phenotype and matrix stiffness of the native enthesis.

5.3 Mechanical properties of biphasic silk fibroin scaffolds in relation to fabrication protocol

A key parameter for scaffold evaluation was mechanical stability, especially at the transition region. Tensile forces are predominant in tendons and ligaments. Thus, type A and B scaffolds were subjected to uniaxial tensile strain and compared to anisotropic scaffolds (with no transition region). The integrity of both type A and B scaffolds was maintained up to 15% of applied strain, indicating good integration between the anisotropic and isotropic parts. The levels of strain experienced by adult tendon/ligament tissue vary between 2-10% depending on anatomical location (Screen et al. 2015).

Structural features, in particular pore alignment, had a high impact on the mechanical properties of scaffolds. Constructs with a progressive change in pore alignment from the anisotropic to the isotropic region (type B) were mechanically more stable and better resembled the structure of the native enthesis compared to constructs with a sharp change in pore alignment (type A). The presence of a sharp transition between the anisotropic and isotropic regions in scaffolds type A could explain the decrease in mechanical strength (Moffat et al. 2008; Thomopoulos et al. 2003). On the contrary, in scaffolds type B, the gradual and interconnected change in pore alignment

facilitated a smooth transfer of mechanical stresses that resulted in a higher Young's modulus similar to that of homogeneous (anisotropic) scaffolds (Thomopoulos et al. 2003; Moffat et al. 2008; Qu et al. 2015). In addition, total porosity was ~5% lower in type B compared to type A scaffolds, which may contribute to increase Young's modulus. These results highlight the impact of fabrication method and structural features on mechanical properties.

Of note, the scaffold's Young's modulus was considerably lower than that of native tendon/ligament and enthesis tissues. In a recent study, Xu et al. (2017) measured the Young's modulus of healthy pig entheses using the same equipment as in the present study and found them to be in the range from 20 to 50 MPa. However, only unseeded scaffolds were tested. Softer scaffolds may be a suitable starting point to observe improvements in mechanical properties after cell culture (Correia et al. 2012). Furthermore, it is important to note that the biphasic scaffolds fabricated in this study (as well as the enthesis (Rossetti et al. 2017)) are structurally heterogeneous and composed of different geometries. This results in local variations of the Young's modulus that are not represented when characterizing the mechanical properties of whole constructs, making comparisons between scaffolds and native tissue only approximate (Rossetti et al. 2017). Future studies will benefit from the measurement of local strains on native enthesis and scaffolds as well as analyzing the change on scaffolds' mechanical properties after culture.

5.4 AdMSCs viability, proliferation and morphology on biphasic scaffolds

Biphasic silk fibroin scaffolds were biocompatible and supported cell attachment, viability and metabolic activity in all scaffold regions. Heparin functionalization and growth factor loading did not significantly affect cell seeding efficiency and metabolic activity on scaffolds. However, the scaffolds did not promote cell proliferation. Similar results were reported by Correia et al. (2012) with anisotropic scaffolds. One hypothesis is that cells did not proliferate because seeding density was high in relation to total porosity, so cells would quickly become confluent. Of note, proliferation between seeding and 3 days of culture was not assessed, so it can't be excluded that cells proliferated during that time until reaching confluence. In addition, limited proliferation could also be related to increased differentiation and metabolic activity (Kim et al. 2005; Correia et al. 2012).

The morphology of AdMSCs was dependent on the morphology and alignment of scaffold's pores. In the anisotropic part of the scaffolds, the cell cytoskeleton aligned in the direction of the scaffold's pores, whereas no alignment was evident in the isotropic region. Substrate anisotropy has been shown to promote cytoskeletal alignment in previous studies (Islam et al. 2016; Oliveira et al.

2012; Mozdzen et al. 2016; Xie et al. 2010). In scaffolds type B, AdMSCs populated the whole scaffold and a progressive change in cytoskeleton alignment could be observed at the transition. This is an interesting characteristic for tendon/ligament-to-bone tissue engineering given the progressive change in collagen molecule alignment and cell morphology at the native interface. In scaffolds type A the change in cell morphology could also be appreciated but was less evident. In addition, less cells populated the transition region of type A compare to type B scaffolds. This may be explained by the presence of a solid layer of fibroin at the transition region, which could difficult cell migration into that area.

5.5 Impact of structural features of biphasic scaffolds on AdMSCs gene expression

The effect of pore alignment on the expression of tendon/ligament, enthesis and cartilage gene markers in AdMSCs was analyzed in each of the scaffold's regions (anisotropic, transition and isotropic) individually. Interestingly, the genes analyzed showed a graded level of expression increasing either towards the anisotropic or isotropic regions, with intermediate levels at the transition. This is a very interesting feature for the regeneration of a gradually changing tissue such as the enthesis.

In both type A and B scaffolds, sox9 and aggrecan (chondrogenic markers) showed a graded level of expression increasing towards the isotropic (cartilage/bone-like) region. However, only in scaffolds type B the expression of the ligamentogenic/tenogenic transcription factor scx increased gradually towards the anisotropic (tendon/ligament-like) region. The expression of collagens type I and type III increased towards the isotropic region in both scaffolds. This may be explained by the higher proportion of big pores in the isotropic part of the scaffolds. In regions with small pores, the ECM produced by the cells fills the pore spaces faster than in regions with bigger pores, which may trigger regulatory mechanisms to slow down ECM synthesis. On the other hand, the expression of collagen II was negligible. Of note, the expression all chondrogenic markers (sox9, collagen II and aggrecan) was low, indicating a poor chondrogenic response. These results highlight the impact of structural and topographical features on gene expression.

In the present study, pore alignment seemed to have a greater influence on gene expression than pore size. Differences in gene expression were observed in the different regions of type B scaffolds despite having very similar total porosity and pore sizes. Furthermore, sox9 and aggrecan were upregulated in the isotropic region of both type A and B scaffolds despite the higher

proportion of bigger pores in type A scaffolds. On the other hand, previous studies have reported significant effects of pore sizes on stem cell behavior. Di Luca et al. (2016) and Oh et al. (2010) analyzed the effect of pore sizes on AdMSCs chondrogenesis. Di Luca et al. reported the upregulation of the chondrogenic markers sox9 and aggrecan on scaffolds with 50% total porosity and pore sizes of 237.7 ± 7.8µm. Conversely, Oh et al. observed higher expression of sox9 and collagen II in scaffolds with pore sizes of 300-400µm compared to smaller pores. In the present study, the focus was put on pore alignment rather than pore size, and scaffold regions were analyzed depending on pore alignment despite having a broad distribution of pore sizes (including <100µm and >500µm). Thus, an effect of pore sizes cannot be excluded. It is likely that the different results obtained in the present and aforementioned studies are related to the effects of other features such as pore morphology and matrix stiffness on gene expression. Of note, the different pore sizes found suitable for chondrogenesis by Di Luca et al. and Oh et al. are in the range of pore sizes present in the biphasic scaffolds of the current study.

5.6 Functionalization of biphasic scaffolds with heparin and its impact on growth factor retention and release

Because of their better mechanical properties, progressive change in pore alignment at the transition, higher cell population and presence of opposite scx/sox9 expression gradients, scaffolds type B were considered more suitable for tendon/ligament-to-bone tissue engineering. However, the scaffolds showed a low chondrogenic potential. Thus, it appears that, although structural cues can modulate cell behavior, they are not enough to promote mature cell differentiation and regeneration of complex tissue interfaces such as the enthesis (Font Tellado, Balmayor, and Van Griensven 2015). These results motivated the functionalization of type B scaffolds to incorporate growth factors.

Growth factors have proven to be potent tools to modulate cell behavior. Growth factors can be incorporated on scaffolds to trigger specific cell responses, such as proliferation or differentiation, directly at the injury site. However, the use of growth factors in tissue engineering applications has been hindered by the lack of suitable delivery systems. Scaffold functionalization can increase the affinity of growth factors for scaffolds and thereby reduce their diffusion out of the matrix, keep their local concentration higher and increase their bioactivity (Balmayor 2015; Silva et al. 2017). In the present work, type B silk fibroin scaffolds were functionalized with heparin to increase their

affinity for the growth factors TGF-β2 and GDF5, which present heparin binding domains in their protein sequences (Ayerst et al. 2017; Rider and Mulloy 2017).

Heparin was covalently bound to type B silk fibroin scaffolds by carbodiimide chemistry. To avoid fibroin crosslinking, which could affect scaffold's structural properties, crosslinkers were reacted with heparin in solution and quenched before adding to the scaffolds. Heparin binding efficiency could not be increased to more than 29% on average. A possible reason is the low availability of primary amines in fibroin able to interact with carboxyl groups in heparin during crosslinking (Vepari and Kaplan 2007). In addition, both heparin and fibroin are negatively charged, complicating electrostatic interactions (Rider and Mulloy 2017).

Functionalization of tendon/ligament-to-bone constructs with heparin showed that heparin is a suitable molecule to increase growth factor retention on scaffold matrices without affecting biocompatibility and growth factor activity. Heparin functionalization allowed to modulate cell behavior with a single administration of low doses of growth factors. This highlights the importance of developing better delivery platforms for growth factor therapies.

The influence of heparin functionalization on the binding and release of TGF-β2 and GDF5 was evaluated by comparing three groups: unmodified scaffolds, scaffolds non-crosslinked with heparin and scaffolds crosslinked with heparin. TGF-β2 and GDF5 incorporated with high efficiency on the three types of scaffolds. This can be explained by electrostatic interactions happening between positively charged TGF-β2/GDF5 and negatively charged fibroin. However, in the presence of an aqueous solution, growth factors rapidly diffused out of unmodified scaffolds or scaffolds non-crosslinked with heparin. This type of release kinetics (burst release) is characteristic from systems in which proteins are adsorbed to porous matrices (Leong et al. 2015; Jeon et al. 2007; Karageorgiou et al. 2006). On the other hand, a significantly lower amount of growth factors was released from scaffolds crosslinked with heparin, indicating that heparin functionalization increased growth factor retention on scaffolds. This can be explained by the more specific and stable electrostatic interactions between heparin binding domains in TGF-β2/GDF5 and heparin molecules (Silva et al. 2017; Rider and Mulloy 2017; Xu et al. 2011). This type of interactions increase growth factor retention on the scaffolds and may also increase protein stability and half-life (Jha et al. 2015; Jeon et al. 2007).

The release kinetics of TGF-β2 and GDF5 from silk fibroin scaffolds followed different patterns. A higher proportion of bound GDF5 was released from unmodified scaffolds and scaffolds non-crosslinked with heparin in comparison to TGF-β2. Conversely, more TGF-β2 was released from heparin-crosslinked scaffolds compared to GDF5. This suggests that TGF-β2 may have a higher

affinity for fibroin, whereas GDF5 appears to have a higher affinity for heparin. These differences can be explained because interactions of proteins with other molecules are influenced by multiple parameters including molecular weight, isoelectric point and the presence of hydrophobic moieties (Jha et al. 2015; Wenk, Merkle, and Meinel 2011). However, growth factor release kinetics were analyzed on whole scaffolds but not in its single parts. Future studies may benefit from the analysis of growth factor release from each scaffold region individually to better understand the effects of scaffold structure on release kinetics.

Interestingly, most of the growth factor released could be detected already after 24h in aqueous solution. This likely corresponds to the proportion of growth factors weakly bound to the matrix, which is higher in unmodified scaffolds and scaffolds non-crosslinked with heparin compared to heparin-crosslinked scaffolds. In addition, growth factor release from 3 days onwards was very low, and total growth factor released after 14 days in heparin-crosslinked scaffolds was ~20%. These results suggest that a high proportion of growth factors remained firmly bound to heparin and to the scaffold matrix and were not released during the observation time. A similar behavior was observed by Karageorgiou et al. (2006) when loading BMP2 on porous silk fibroin scaffolds and by Manning et al. (2013) when incorporating heparin into a nanofibrous scaffold for platelet-derived growth factor delivery. These data points to a possible interaction between matrix-bound growth factors and cell receptors, although further research will be necessary to contrast this hypothesis.

5.7 Synergistic effects of structural and biochemical cues on stem cell gene and protein expression

The effects of TGF-β2/GDF5 on gene and protein expression were tightly coupled to and influenced by the structural features of scaffolds. Pore alignment, morphology and size have direct effects on cell morphology and gene expression, and at the same time influence the diffusion and local concentration of growth factors in the scaffold matrix. Thus, each scaffold region represents a unique cellular microenvironment with specific structural features, local levels of growth factors and certain nutrient and oxygen diffusion rates. In addition, the combined supplementation of TGF-β2 and GDF5 had different effects on cell behavior that either growth factor alone. For that reason, understanding the combined effects of structural and biochemical cues on cell behavior is critical for the design and improvement of tissue engineering strategies.

Despite that, relatively few studies have focused on analyzing the combined effects of growth factor supplementation and scaffold structure on stem cell differentiation. Recently, Olvera et al. (2017) analyzed the effect of microfiber alignment and supplementation of TGF-β3 and/or connective tissue growth factor (CTGF) on the ligamentogenic and chondrogenic differentiation of BMSCs. In general, growth factor treatment had stronger effects on gene expression than microfiber alignment. This may be related to the fact that growth factors were directly supplemented to the cell culture medium, and thus local growth factor concentrations were less influenced by the structural features of scaffolds. However, the expression of collagen II, BMP2, aggrecan and tenomodulin was dependent on microfiber alignment.

To evaluate all the possible combinations of growth factor supplementation and pore alignment on cell behavior, TGF-β2 and GDF5 were incorporated on whole scaffolds but their effects on gene and protein expression were evaluated separately in each scaffold region (anisotropic, transition and isotropic). The analysis was performed in type B biphasic scaffolds crosslinked with heparin and without growth factors (unloaded) or loaded with TGF-β2, GDF5 or their combination. To identify synergistic interactions between TGF-β2/GDF5 and pore alignment, gene expression data from each scaffold region in growth factor-loaded scaffolds was expressed as fold change respect to the same region in unloaded scaffolds. The focus was put on identifying which growth factor or combination of growth factors would stimulate the expression of tenogenic/ligamentogenic markers in the anisotropic part of the scaffolds, fibrochondrogenic markers in the transition and chondrogenic markers in the isotropic part.

Incorporation of TGF-β2 had the best tenogenic/ligamentogenic promoting effects in the anisotropic region of type B scaffolds according to gene expression and qualitative protein expression data. Our data suggest that structural and biochemical cues can influence each other in a synergistic manner. However, growth factor treatment could not enhance scx expression on anisotropic substrates. A similar behavior was observed by Caliari and Harley (2014), who did not find positive interactions between scaffold anisotropy and treatment with GDF5 or GDF7 on scx expression.

The best chondrogenic effects at the isotropic region of type B scaffolds were observed by the combined supplementation of TGF-β2 and GDF5. Our results suggest that heparin-based incorporation of TGF-β2 and GDF5 improved the chondrogenic potential of type B silk fibroin scaffolds. Interestingly, a recent study by Ayerst et al. (2017) reported an inhibitory effect of heparin on the chondrogenic properties of GDF5. This could explain the weak effects of GDF5 on AdMSCs gene expression in comparison to TGF-β2. According to our data, GDF5 enhanced

collagen II protein expression and had pro-chondrogenic and pro-fibrochondrogenic effects when delivered in combination with TGF-β2. However, it cannot be concluded from this study if the observed effects happened because of released or heparin-bound GDF5. Thus, future studies will benefit from comparing the effect of free vs. matrix-bound growth factors on cell behavior.

The gene and protein markers that characterize fibrocartilage are not as well established as those for tendon/ligament and cartilage (see section 2.3.1). At the gene level, the expression of both scx and sox9 seems to be necessary for the specification of fibrochondrocyte progenitors and the formation of fibrocartilage. In addition, collagen II, collagen III and aggrecan are present in the ECM of NF and/or MF (see section 2.1). The combined supplementation of TGF-β2 and GDF5 promoted the expression of sox9, collagen II, collagen III and aggrecan at the transition region of type B scaffolds. In addition, mohawk and collagen I were also upregulated at late time points. These results suggest that the combined supplementation of TGF-β2 and GDF5 induced the expression of both chondrogenic and tenogenic/ligamentogenic markers in the transition region, which may be favorable for fibrochondrogenic differentiation. At the protein level, both GDF5 and TGF-β2 and GDF5 groups showed higher levels of collagen II at the transition compared to the other groups. Collagen III levels were the highest in the TGF-β2 and GDF5 group. Interestingly, a recent study reported the fibrochondrogenic effects of the sequential supplementation of TGF-β3 and CTGF on BMSCs, whereas TGF-β3 alone showed pro-chodrogenic effects and CTGF alone had pro-ligamentogenic effects (Olvera et al. 2017). These results provide new insights into the effects of pore alignment and growth factor treatment on AdMSCs fibrochondrogenesis. However, the markers used for characterization are not specific of enthesis fibrochondrocytes, but also common to tendon/ligament fibroblasts or chondrocytes. The lack of fibrochondrocyte-specific markers poses difficulties to the phenotypic evaluation of regenerated tissue. Thus, future studies will benefit from advances on fibrochondrocyte characterization at the molecular level.

Together, these data highlight the importance of analyzing the combined impact of molecular and structural cues for tissue engineering strategies, since the effects of single components may not be representative of the system.

5.8   Conclusions and outlook

This work provides new insights into the effects of cell-material and growth factor-material interactions on stem cell differentiation and highlights the importance of such interactions in tissue engineering applications. The data obtained in this study improves current knowledge on how

structural and biochemical cues provided by scaffolds can be tailored to induce site-specific multilineage differentiation of AdMSCs.

However, there is still room for improvement. On the one hand, the tendon/ligament-to-bone constructs fabricated in this study incorporated only one of the two structural gradients present at the native interface. Thus, the constructs may be further improved by the incorporation of a mineral gradient increasing towards the isotropic (cartilage/bone) region. Incorporation of a mineral phase could be of advantage to generate a stiffness gradient on the scaffolds and to improve their integration with bone tissue. In addition, mineral particles themselves and the ions they release could contribute to promote endochondral ossification in the cartilage/bone part of the constructs. Another interesting area of research would focus on targeting TGF-β2 to the anisotropic part of the scaffolds and TGF-β2 and GDF5 to the transition and anisotropic parts to induce site-specific stem cell differentiation in a single scaffold. In addition, testing other growth factors of the TGF-β family would be of interest to identify further synergistic cues to modulate cell behavior.

Finally, the present study gives preliminary data on the effects of structural and biochemical cues on enthesis regeneration. However, the system might behave differently *in vivo*. Thus, evaluation of the scaffolds in *in vivo* models for tendon/ligament-to-bone repair would be of interest to evaluate the actual degree of tissue regeneration obtained with scaffolds compared to the standard surgical treatment and to other commercially available scaffolds. For that, advances in the molecular characterization of native entheses will be of advantage for a better evaluation of tissue regeneration outcome.

6 REFERENCES

Augst, A., D. Marolt, L. E. Freed, C. Vepari, L. Meinel, M. Farley, R. Fajardo, N. Patel, M. Gray, D. L. Kaplan, and G. Vunjak-Novakovic. 2008. 'Effects of chondrogenic and osteogenic regulatory factors on composite constructs grown using human mesenchymal stem cells, silk scaffolds and bioreactors', *J R Soc Interface*, 5: 929-39.

Ayerst, B. I., R. A. Smith, V. Nurcombe, A. J. Day, C. L. Merry, and S. M. Cool. 2017. 'Growth Differentiation Factor 5-Mediated Enhancement of Chondrocyte Phenotype Is Inhibited by Heparin: Implications for the Use of Heparin in the Clinic and in Tissue Engineering Applications', *Tissue Eng Part A*, 23: 275-92.

Bais, M. V., N. Wigner, M. Young, R. Toholka, D. T. Graves, E. F. Morgan, L. C. Gerstenfeld, and T. A. Einhorn. 2009. 'BMP2 is essential for post natal osteogenesis but not for recruitment of osteogenic stem cells', *Bone*, 45: 254-66.

Balmayor, E. R. 2015. 'Targeted delivery as key for the success of small osteoinductive molecules', *Adv Drug Deliv Rev*, 94: 13-27.

Bandyopadhyay, A., K. Tsuji, K. Cox, B. D. Harfe, V. Rosen, and C. J. Tabin. 2006. 'Genetic analysis of the roles of BMP2, BMP4, and BMP7 in limb patterning and skeletogenesis', *PLoS Genet*, 2(12): e216.

Baykan, E., A. Koc, A. Eser Elcin, and Y. Murat Elcin. 2014. 'Evaluation of a biomimetic poly(epsilon-caprolactone)/beta-tricalcium phosphate multispiral scaffold for bone tissue engineering: in vitro and in vivo studies', *Biointerphases*, 9: 029011.

Beederman, M., J. D. Lamplot, G. Nan, J. Wang, X. Liu, L. Yin, R. Li, W. Shui, H. Zhang, S. H. Kim, W. Zhang, J. Zhang, Y. Kong, S. Denduluri, M. R. Rogers, A. Pratt, R. C. Haydon, H. H. Luu, J. Angeles, L. L. Shi, and T. C. He. 2013. 'BMP signaling in mesenchymal stem cell differentiation and bone formation', *J Biomed Sci Eng*, 6: 32-52.

Bei, K., Z. Du, Y. Xiong, J. Liao, B. Su, and L. Wu. 2012. 'BMP7 can promote osteogenic differentiation of human periosteal cells in vitro', *Mol Biol Rep*, 39: 8845-51.

Benjamin, M., H. Toumi, J. R. Ralphs, G. Bydder, T. M. Best, and S. Milz. 2006. 'Where tendons and ligaments meet bone: attachment sites ('entheses') in relation to exercise and/or mechanical load', *J Anat*, 208: 471-90.

Bessa, P. C., E. R. Balmayor, H. S. Azevedo, S. Nurnberger, M. Casal, M. van Griensven, R. L. Reis, and H. Redl. 2010. 'Silk fibroin microparticles as carriers for delivery of human recombinant BMPs. Physical characterization and drug release', *J Tissue Eng Regen Med*, 4: 349-55.

Bessa, P. C., E. R. Balmayor, J. Hartinger, G. Zanoni, D. Dopler, A. Meinl, A. Banerjee, M. Casal, H. Redl, R. L. Reis, and M. van Griensven. 2010. 'Silk fibroin microparticles as carriers for delivery of human recombinant bone morphogenetic protein-2: in vitro and in vivo bioactivity', *Tissue Eng Part C Methods*, 16: 937-45.

Bettinger, C. J., R. Langer, and J. T. Borenstein. 2009. 'Engineering substrate topography at the micro- and nanoscale to control cell function', *Angew Chem Int Ed Engl*, 48: 5406-15.

Bhattacharjee, M., S. Miot, A. Gorecka, K. Singha, M. Loparic, S. Dickinson, A. Das, N. S. Bhavesh, A. R. Ray, I. Martin, and S. Ghosh. 2012. 'Oriented lamellar silk fibrous scaffolds to drive cartilage matrix orientation: towards annulus fibrosus tissue engineering', *Acta Biomater*, 8: 3313-25.

Bi, F., Z. Shi, A. Liu, P. Guo, and S. Yan. 2015. 'Anterior cruciate ligament reconstruction in a rabbit model using silk-collagen scaffold and comparison with autograft', *PLoS One*, 10: e0125900.

Blitz, E., A. Sharir, H. Akiyama, and E. Zelzer. 2013. 'Tendon-bone attachment unit is formed modularly by a distinct pool of Scx- and Sox9-positive progenitors', *Development*, 140: 2680-90.

Blitz, E., S. Viukov, A. Sharir, Y. Shwartz, J. L. Galloway, B. A. Pryce, R. L. Johnson, C. J. Tabin, R. Schweitzer, and E. Zelzer. 2009. 'Bone ridge patterning during musculoskeletal assembly is mediated through SCX regulation of Bmp4 at the tendon-skeleton junction', *Dev Cell*, 17: 861-73.

Caliari, S. R., and B. A. Harley. 2014. 'Structural and biochemical modification of a collagen scaffold to selectively enhance MSC tenogenic, chondrogenic, and osteogenic differentiation', *Adv Healthc Mater*, 3: 1086-96.

Choi, J. W., E. J. Park, H. S. Shin, I. S. Shin, J. C. Ra, and K. S. Koh. 2014. 'In vivo differentiation of undifferentiated human adipose tissue-derived mesenchymal stem cells in critical-sized calvarial bone defects', *Ann Plast Surg*, 72: 225-33.

Cicione, C., E. Muinos-Lopez, T. Hermida-Gomez, I. Fuentes-Boquete, S. Diaz-Prado, and F. J. Blanco. 2015. 'Alternative protocols to induce chondrogenic differentiation: transforming growth factor-beta superfamily', *Cell Tissue Bank*, 16: 195-207.

Correia, C., S. Bhumiratana, L. P. Yan, A. L. Oliveira, J. M. Gimble, D. Rockwood, D. L. Kaplan, R. A. Sousa, R. L. Reis, and G. Vunjak-Novakovic. 2012. 'Development of silk-based scaffolds for tissue engineering of bone from human adipose-derived stem cells', *Acta Biomater*, 8: 2483-92.

Criscenti, G., A. Longoni, A. Di Luca, C. De Maria, C. A. van Blitterswijk, G. Vozzi, and L. Moroni. 2016. 'Triphasic scaffolds for the regeneration of the bone-ligament interface', *Biofabrication*, 8: 015009.

Della Porta, G., B. N. Nguyen, R. Campardelli, E. Reverchon, and J. P. Fisher. 2015. 'Synergistic effect of sustained release of growth factors and dynamic culture on osteoblastic differentiation of mesenchymal stem cells', *J Biomed Mater Res A*, 103: 2161-71.

Demoor, M., D. Ollitrault, T. Gomez-Leduc, M. Bouyoucef, M. Hervieu, H. Fabre, J. Lafont, J. M. Denoix, F. Audigie, F. Mallein-Gerin, F. Legendre, and P. Galera. 2014. 'Cartilage tissue engineering: molecular control of chondrocyte differentiation for proper cartilage matrix reconstruction', *Biochim Biophys Acta*, 1840: 2414-40.

Deville, S., E. Saiz, R. K. Nalla, and A. P. Tomsia. 2006. 'Freezing as a path to build complex composites', *Science*, 311: 515-8.

Deville, S., E. Saiz, and A. P. Tomsia. 2006. 'Freeze casting of hydroxyapatite scaffolds for bone tissue engineering', *Biomaterials*, 27: 5480-9.

Dhandayuthapani, B., Y. Yoshida, T. Maekawa, and D. S. Kumar. 2011. 'Polymeric Scaffolds in Tissue Engineering Application: A Review', *Int J Polym Sci*, 2011: 1-19.

Di Luca, A., K. Szlazak, I. Lorenzo-Moldero, C. A. Ghebes, A. Lepedda, W. Swieszkowski, C. Van Blitterswijk, and L. Moroni. 2016. 'Influencing chondrogenic differentiation of human mesenchymal stromal cells in scaffolds displaying a structural gradient in pore size', *Acta Biomater*, 36: 210-9.

Ding, X., M. Zhu, B. Xu, J. Zhang, Y. Zhao, S. Ji, L. Wang, L. Wang, X. Li, D. Kong, X. Ma, and Q. Yang. 2014. 'Integrated trilayered silk fibroin scaffold for osteochondral differentiation of adipose-derived stem cells', *ACS Appl Mater Interfaces*, 6: 16696-705.

Dyment, N. A., A. P. Breidenbach, A. G. Schwartz, R. P. Russell, L. Aschbacher-Smith, H. Liu, Y. Hagiwara, R. Jiang, S. Thomopoulos, D. L. Butler, and D. W. Rowe. 2015. 'Gdf5 progenitors give rise to fibrocartilage cells that mineralize via hedgehog signaling to form the zonal enthesis', *Dev Biol*, 405: 96-107.

Enochson, L., J. Stenberg, M. Brittberg, and A. Lindahl. 2014. 'GDF5 reduces MMP13 expression in human chondrocytes via DKK1 mediated canonical Wnt signaling inhibition', *Osteoarthr. Cartil*, 22: 566-77.

Fan, H., H. Liu, S. L. Toh, and J. C. Goh. 2009. 'Anterior cruciate ligament regeneration using mesenchymal stem cells and silk scaffold in large animal model', *Biomaterials*, 30: 4967-77.

Font Tellado, S., E. R. Balmayor, and M. Van Griensven. 2015. 'Strategies to engineer tendon/ligament-to-bone interface: Biomaterials, cells and growth factors', *Adv Drug Deliv Rev*, 94: 126-40.

Font Tellado, S., W. Bonani, E. R. Balmayor, P. Foehr, A. Motta, C. Migliaresi, and M. van Griensven. 2017. 'Fabrication and Characterization of Biphasic Silk Fibroin Scaffolds for Tendon/Ligament-to-Bone Tissue Engineering', *Tissue Eng Part A*, 23: 859-72.

Foss, C., E. Merzari, C. Migliaresi, and A. Motta. 2013. 'Silk fibroin/hyaluronic acid 3D matrices for cartilage tissue engineering', *Biomacromolecules*, 14: 38-47.

Foss, C., C. Migliaresi, and A. Motta. 2013. 'The optimization of a scaffold for cartilage regeneration', *Organogenesis*, 9: 19-21.

Genin, G. M., A. Kent, V. Birman, B. Wopenka, J. D. Pasteris, P. J. Marquez, and S. Thomopoulos. 2009. 'Functional grading of mineral and collagen in the attachment of tendon to bone', *Biophys J*, 97: 976-85.

Guo, X., and X. F. Wang. 2009. 'Signaling cross-talk between TGF-beta/BMP and other pathways', *Cell Res*, 19: 71-88.

Handorf, A. M., and W. J. Li. 2014. 'Induction of mesenchymal stem cell chondrogenesis through sequential administration of growth factors within specific temporal windows', *J Cell Physiol*, 229: 162-71.

He, P., K. S. Ng, S. L. Toh, and J. C. Goh. 2012. 'In vitro ligament-bone interface regeneration using a trilineage coculture system on a hybrid silk scaffold', *Biomacromolecules*, 13: 2692-703.

He, Y., Y. Dong, X. Chen, and R. Lin. 2014. 'Ectopic osteogenesis and scaffold biodegradation of tissue engineering bone composed of chitosan and osteo-induced bone marrow mesenchymal stem cells in vivo', *Chin Med J (Engl)*, 127: 322-8.

Hildner, F., A. Peterbauer, S. Wolbank, S. Nurnberger, S. Marlovits, H. Redl, M. van Griensven, and C. Gabriel. 2010. 'FGF-2 abolishes the chondrogenic effect of combined BMP-6 and TGF-beta in human adipose derived stem cells', *J Biomed Mater Res A*, 94: 978-87.

Hutton, D. L., E. M. Moore, J. M. Gimble, and W. L. Grayson. 2013. 'Platelet-derived growth factor and spatiotemporal cues induce development of vascularized bone tissue by adipose-derived stem cells', *Tissue Eng Part A*, 19: 2076-86.

Islam, A., M. Younesi, T. Mbimba, and O. Akkus. 2016. 'Collagen Substrate Stiffness Anisotropy Affects Cellular Elongation, Nuclear Shape, and Stem Cell Fate toward Anisotropic Tissue Lineage', *Adv Healthc Mater*, 5: 2237-47.

Ito, Y., N. Toriuchi, T. Yoshitaka, H. Ueno-Kudoh, T. Sato, S. Yokoyama, K. Nishida, T. Akimoto, M. Takahashi, S. Miyaki, and H. Asahara. 2010. 'The Mohawk homeobox gene is a critical regulator of tendon differentiation', *Proc Natl Acad Sci U S A*, 107: 10538-42.

Izadpanah, R., C. Trygg, B. Patel, C. Kriedt, J. Dufour, J. M. Gimble, and B. A. Bunnell. 2006. 'Biologic properties of mesenchymal stem cells derived from bone marrow and adipose tissue', *J Cell Biochem*, 99: 1285-97.

James, R., S. G. Kumbar, C. T. Laurencin, G. Balian, and A. B. Chhabra. 2011. 'Tendon tissue engineering: adipose-derived stem cell and GDF-5 mediated regeneration using electrospun matrix systems', *Biomed Mater*, 6: 025011.

Jeon, O., S. W. Kang, H. W. Lim, J. Hyung Chung, and B. S. Kim. 2006. 'Long-term and zero-order release of basic fibroblast growth factor from heparin-conjugated poly(L-lactide-co-glycolide) nanospheres and fibrin gel', *Biomaterials*, 27: 1598-607.

Jeon, O., S. J. Song, S. W. Kang, A. J. Putnam, and B. S. Kim. 2007. 'Enhancement of ectopic bone formation by bone morphogenetic protein-2 released from a heparin-conjugated poly(L-lactic-co-glycolic acid) scaffold', *Biomaterials*, 28: 2763-71.

Jha, A. K., A. Mathur, F. L. Svedlund, J. Ye, Y. Yeghiazarians, and K. E. Healy. 2015. 'Molecular weight and concentration of heparin in hyaluronic acid-based matrices modulates growth factor retention kinetics and stem cell fate', *J Control Release*, 209: 308-16.

Kane, R. J., H. E. Weiss-Bilka, M. J. Meagher, Y. Liu, J. A. Gargac, G. L. Niebur, D. R. Wagner, and R. K. Roeder. 2015. 'Hydroxyapatite reinforced collagen scaffolds with improved architecture and mechanical properties', *Acta Biomater*, 17: 16-25.

Karageorgiou, V., M. Tomkins, R. Fajardo, L. Meinel, B. Snyder, K. Wade, J. Chen, G. Vunjak-Novakovic, and D. L. Kaplan. 2006. 'Porous silk fibroin 3-D scaffolds for delivery of bone morphogenetic protein-2 in vitro and in vivo', *J Biomed Mater Res A*, 78: 324-34.

Kern, S., H. Eichler, J. Stoeve, H. Kluter, and K. Bieback. 2006. 'Comparative analysis of mesenchymal stem cells from bone marrow, umbilical cord blood, or adipose tissue', *Stem Cells*, 24: 1294-301.

Killian, M. L., and S. Thomopoulos. 2016. 'Scleraxis is required for the development of a functional tendon enthesis', *Faseb j*, 30: 301-11.

Kim, U. J., J. Park, H. J. Kim, M. Wada, and D. L. Kaplan. 2005. 'Three-dimensional aqueous-derived biomaterial scaffolds from silk fibroin', *Biomaterials*, 26: 2775-85.

King, W. J., and P. H. Krebsbach. 2012. 'Growth factor delivery: how surface interactions modulate release in vitro and in vivo', *Adv Drug Deliv Rev*, 64: 1239-56.

Koo, K. H., J. M. Lee, J. M. Ahn, B. S. Kim, W. G. La, C. S. Kim, and G. I. Im. 2013. 'Controlled delivery of low-dose bone morphogenetic protein-2 using heparin-conjugated fibrin in the posterolateral lumbar fusion of rabbits', *Artif Organs*, 37: 487-94.

Kronenberg, H. M. 2003. 'Developmental regulation of the growth plate', *Nature*, 423: 332-6.

Lee, K., E. A. Silva, and D. J. Mooney. 2011. 'Growth factor delivery-based tissue engineering: general approaches and a review of recent developments', *J R Soc Interface*, 8: 153-70.

Leong, N. L., A. Arshi, N. Kabir, A. Nazemi, F. A. Petrigliano, B. M. Wu, and D. R. McAllister. 2015. 'In vitro and in vivo evaluation of heparin mediated growth factor release from tissue-engineered constructs for anterior cruciate ligament reconstruction', *J Orthop Res*, 33: 229-36.

Leong, N. L., F. A. Petrigliano, and D. R. McAllister. 2014. 'Current tissue engineering strategies in anterior cruciate ligament reconstruction', *J Biomed Mater Res A*, 102: 1614-24.

Li, H., J. Fan, L. Sun, X. Liu, P. Cheng, and H. Fan. 2016. 'Functional regeneration of ligament-bone interface using a triphasic silk-based graft', *Biomaterials*, 106: 180-92.

Li, J. J., K. Kim, S. I. Roohani-Esfahani, J. Guo, D. L. Kaplan, and H. Zreiqat. 2015. 'A biphasic scaffold based on silk and bioactive ceramic with stratified properties for osteochondral tissue regeneration', *J Mater Chem B Mater Biol Med*, 3: 5361-76.

Lipner, J., H. Shen, L. Cavinatto, W. Liu, N. Havlioglu, Y. Xia, L. M. Galatz, and S. Thomopoulos. 2015. 'In Vivo Evaluation of Adipose-Derived Stromal Cells Delivered with a Nanofiber Scaffold for Tendon-to-Bone Repair', *Tissue Eng Part A*, 21: 2766-74.

Liu, C. F., L. Aschbacher-Smith, N. J. Barthelery, N. Dyment, D. Butler, and C. Wylie. 2012. 'Spatial and temporal expression of molecular markers and cell signals during normal development of the mouse patellar tendon', *Tissue Eng Part A*, 18: 598-608.

Liu, H., S. Zhu, C. Zhang, P. Lu, J. Hu, Z. Yin, Y. Ma, X. Chen, and H. OuYang. 2014. 'Crucial transcription factors in tendon development and differentiation: their potential for tendon regeneration', *Cell Tissue Res*, 356: 287-98.

Liu, W., J. Lipner, J. Xie, C. N. Manning, S. Thomopoulos, and Y. Xia. 2014. 'Nanofiber scaffolds with gradients in mineral content for spatial control of osteogenesis', *ACS Appl Mater Interfaces*, 6: 2842-9.

Liu, Y., V. Birman, C. Chen, S. Thomopoulos, and G. M. Genin. 2011. 'Mechanisms of Bimaterial Attachment at the Interface of Tendon to Bone', *J Eng Mater Technol*, 133: 011005-05-8.

Lorda-Diez, C. I., J. A. Montero, C. Martinez-Cue, J. A. Garcia-Porrero, and J. M. Hurle. 2009. 'Transforming growth factors beta coordinate cartilage and tendon differentiation in the developing limb mesenchyme', *J Biol Chem*, 284: 29988-96.

Lou, T., X. Wang, G. Song, Z. Gu, and Z. Yang. 2014. 'Fabrication of PLLA/beta-TCP nanocomposite scaffolds with hierarchical porosity for bone tissue engineering', *Int J Biol Macromol*, 69: 464-70.

Lu, H. H., and S. Thomopoulos. 2013. 'Functional attachment of soft tissues to bone: development, healing, and tissue engineering', *Annu Rev Biomed Eng*, 15: 201-26.

Lu, W., K. Ji, J. Kirkham, Y. Yan, A. R. Boccaccini, M. Kellett, Y. Jin, and X. B. Yang. 2014. 'Bone tissue engineering by using a combination of polymer/Bioglass composites with human adipose-derived stem cells', *Cell Tissue Res*, 356: 97-107.

Malafaya, B., A. J. Pedro, A. Peterbauer, C. Gabriel, H. Redl, and R. L. Reis. 2005. 'Chitosan particles agglomerated scaffolds for cartilage and osteochondral tissue engineering approaches with adipose tissue derived stem cells', *J Mater Sci Mater Med*, 16: 1077-85.

Manning, C. N., H. M. Kim, S. Sakiyama-Elbert, L. M. Galatz, N. Havlioglu, and S. Thomopoulos. 2011. 'Sustained delivery of transforming growth factor beta three enhances tendon-to-bone healing in a rat model', *J Orthop Res*, 29: 1099-105.

Manning, C. N., A. G. Schwartz, W. Liu, J. Xie, N. Havlioglu, S. E. Sakiyama-Elbert, M. J. Silva, Y. Xia, R. H. Gelberman, and S. Thomopoulos. 2013. 'Controlled delivery of mesenchymal stem cells and growth factors using a nanofiber scaffold for tendon repair', *Acta Biomater*, 9: 6905-14.

Martino, M. M., P. S. Briquez, K. Maruyama, and J. A. Hubbell. 2015. 'Extracellular matrix-inspired growth factor delivery systems for bone regeneration', *Adv Drug Deliv Rev*, 94: 41-52.

McCaffrey, T. A., D. J. Falcone, C. F. Brayton, L. A. Agarwal, F. G. Welt, and B. B. Weksler. 1989. 'Transforming growth factor-beta activity is potentiated by heparin via dissociation of the transforming growth factor-beta/alpha 2-macroglobulin inactive complex', *J Cell Biol*, 109: 441-8.

Mitchell, A. C., P. S. Briquez, J. A. Hubbell, and J. R. Cochran. 2016. 'Engineering growth factors for regenerative medicine applications', *Acta Biomater*, 30: 1-12.

Moffat, K. L., W. H. Sun, P. E. Pena, N. O. Chahine, S. B. Doty, G. A. Ateshian, C. T. Hung, and H. H. Lu. 2008. 'Characterization of the structure-function relationship at the ligament-to-bone interface', *Proc Natl Acad Sci U S A*, 105: 7947-52.

Moffat, K. L., I. N. Wang, S. A. Rodeo, and H. H. Lu. 2009. 'Orthopedic interface tissue engineering for the biological fixation of soft tissue grafts', *Clin Sports Med*, 28: 157-76.

Mohammadkhah, A., L. M. Marquardt, S. E. Sakiyama-Elbert, D. E. Day, and A. B. Harkins. 2015. 'Fabrication and characterization of poly-(epsilon)-caprolactone and bioactive glass composites for tissue engineering applications', *Mater Sci Eng C Mater Biol Appl*, 49: 632-9.

Mozdzen, L. C., S. D. Thorpe, H. R. Screen, and B. A. Harley. 2016. 'The Effect of Gradations in Mineral Content, Matrix Alignment, and Applied Strain on Human Mesenchymal Stem Cell Morphology within Collagen Biomaterials', *Adv Healthc Mater*, 5: 1731-9.

Nerurkar, N. L., S. Sen, B. M. Baker, D. M. Elliott, and R. L. Mauck. 2011. 'Dynamic culture enhances stem cell infiltration and modulates extracellular matrix production on aligned electrospun nanofibrous scaffolds', *Acta Biomater*, 7: 485-91.

Nguyen, D. T., J. Geel, M. Schulze, M. J. Raschke, S. L. Woo, C. N. van Dijk, and L. Blankevoort. 2013. 'Healing of the goat anterior cruciate ligament after a new suture repair technique and bioscaffold treatment', *Tissue Eng Part A*, 19: 2292-9.

Oh, S. H., T. H. Kim, G. I. Im, and J. H. Lee. 2010. 'Investigation of pore size effect on chondrogenic differentiation of adipose stem cells using a pore size gradient scaffold', *Biomacromolecules*, 11: 1948-55.

Oliveira, A. L., L. Sun, H. J. Kim, X. Hu, W. Rice, J. Kluge, R. L. Reis, and D. L. Kaplan. 2012. 'Aligned silk-based 3-D architectures for contact guidance in tissue engineering', *Acta Biomater*, 8: 1530-42.

Olvera, D., B. N. Sathy, S. F. Carroll, and D. J. Kelly. 2017. 'Modulating microfibrillar alignment and growth factor stimulation to regulate mesenchymal stem cell differentiation', *Acta Biomater*, 64: 148-60.

Park, Y. R., H. W. Ju, J. M. Lee, D. K. Kim, O. J. Lee, B. M. Moon, H. J. Park, J. Y. Jeong, Y. K. Yeon, and C. H. Park. 2016. 'Three-dimensional electrospun silk-fibroin nanofiber for skin tissue engineering', *Int J Biol Macromol*, 93: 1567-74.

Paschos, N. K., and S. M. Howell. 2016. 'Anterior cruciate ligament reconstruction: principles of treatment', *EFORT Open Rev*, 1: 398-408.

Poh, P. S., D. W. Hutmacher, B. M. Holzapfel, A. K. Solanki, M. M. Stevens, and M. A. Woodruff. 2016. 'In vitro and in vivo bone formation potential of surface calcium phosphate-coated polycaprolactone and polycaprolactone/bioactive glass composite scaffolds', *Acta Biomater*, 30: 319-33.

Poh, P. S., D. W. Hutmacher, M. M. Stevens, and M. A. Woodruff. 2013. 'Fabrication and in vitro characterization of bioactive glass composite scaffolds for bone regeneration', *Biofabrication*, 5: 045005.

Prosecka, E., M. Rampichova, A. Litvinec, Z. Tonar, M. Kralickova, L. Vojtova, P. Kochova, M. Plencner, M. Buzgo, A. Mickova, J. Jancar, and E. Amler. 2015. 'Collagen/hydroxyapatite scaffold enriched with polycaprolactone nanofibers, thrombocyte-rich solution and mesenchymal stem cells promotes regeneration in large bone defect in vivo', *J Biomed Mater Res A*, 103: 671-82.

Qu, D., C. Z. Mosher, M. K. Boushell, and H. H. Lu. 2015. 'Engineering complex orthopaedic tissues via strategic biomimicry', *Ann Biomed Eng*, 43: 697-717.

Quintana, L., N. I. zur Nieden, and C. E. Semino. 2009. 'Morphogenetic and regulatory mechanisms during developmental chondrogenesis: new paradigms for cartilage tissue engineering', *Tissue Eng Part B Rev*, 15: 29-41.

Rambhia, Kunal J., and Peter X. Ma. 2015. 'Controlled drug release for tissue engineering', *Journal of Controlled Release*, 219: 119-28.

Rehmann, M. S., J. I. Luna, E. Maverakis, and A. M. Kloxin. 2016. 'Tuning microenvironment modulus and biochemical composition promotes human mesenchymal stem cell tenogenic differentiation', *J Biomed Mater Res A*, 104: 1162-74.

Rider, C. C., and B. Mulloy. 2017. 'Heparin, Heparan Sulphate and the TGF-beta Cytokine Superfamily', *Molecules*, 22: 713-24.

Rockwood, D. N., R. C. Preda, T. Yucel, X. Wang, M. L. Lovett, and D. L. Kaplan. 2011. 'Materials fabrication from Bombyx mori silk fibroin', *Nat Protoc*, 6: 1612-31.

Rossetti, L., L. A. Kuntz, E. Kunold, J. Schock, K. W. Muller, H. Grabmayr, J. Stolberg-Stolberg, F. Pfeiffer, S. A. Sieber, R. Burgkart, and A. R. Bausch. 2017. 'The microstructure and micromechanics of the tendon-bone insertion', *Nat Mater*, 16: 664-70.

Rothrauff, B. B., and R. S. Tuan. 2014. 'Cellular therapy in bone-tendon interface regeneration', *Organogenesis*, 10: 13-28.

Satora, W., A. Krolikowska, A. Czamara, and P. Reichert. 2017. 'Synthetic grafts in the treatment of ruptured anterior cruciate ligament of the knee joint', *Polim Med*, 47: 55-59.

Schneider, S., M. Unger, M. van Griensven, and E. R. Balmayor. 2017. 'Adipose-derived mesenchymal stem cells from liposuction and resected fat are feasible sources for regenerative medicine', *Eur J Med Res*, 22: 17.

Schwartz, A. G., L. M. Galatz, and S. Thomopoulos. 2017. 'Enthesis regeneration: a role for Gli1+ progenitor cells', *Development*, 144: 1159-64.

Schwartz, A. G., J. H. Lipner, J. D. Pasteris, G. M. Genin, and S. Thomopoulos. 2013. 'Muscle loading is necessary for the formation of a functional tendon enthesis', *Bone*, 55: 44-51.

Schwartz, A. G., F. Long, and S. Thomopoulos. 2015. 'Enthesis fibrocartilage cells originate from a population of Hedgehog-responsive cells modulated by the loading environment', *Development*, 142: 196-206.

Screen, H. R., D. E. Berk, K. E. Kadler, F. Ramirez, and M. F. Young. 2015. 'Tendon functional extracellular matrix', *J Orthop Res*, 33: 793-9.

Shaw, H. M., and M. Benjamin. 2007. 'Structure-function relationships of entheses in relation to mechanical load and exercise', *Scand J Med Sci Sports*, 17: 303-15.

Silva, C., A. Carretero, D. Soares da Costa, R. L. Reis, R. Novoa-Carballal, and I. Pashkuleva. 2017. 'Design of protein delivery systems by mimicking extracellular mechanisms for protection of growth factors', *Acta Biomater*, 63: 283-93.

Smith, L., Y. Xia, L. M. Galatz, G. M. Genin, and S. Thomopoulos. 2012. 'Tissue-engineering strategies for the tendon/ligament-to-bone insertion', *Connect Tissue Res*, 53: 95-105.

Soo Kim, B., E. Ji Kim, J. Suk Choi, J. Hoon Jeong, C. Hyunchul Jo, and Y. Woo Cho. 2014. 'Human collagen-based multilayer scaffolds for tendon-to-bone interface tissue engineering', *J Biomed Mater Res A*, 102: 4044-54.

Spalazzi, J. P., E. Dagher, S. B. Doty, X. E. Guo, S. A. Rodeo, and H. H. Lu. 2008. 'In vivo evaluation of a multiphased scaffold designed for orthopaedic interface tissue engineering and soft tissue-to-bone integration', *J Biomed Mater Res A*, 86: 1-12.

Spalazzi, J. P., S. B. Doty, K. L. Moffat, W. N. Levine, and H. H. Lu. 2006. 'Development of controlled matrix heterogeneity on a triphasic scaffold for orthopedic interface tissue engineering', *Tissue Eng*, 12: 3497-508.

Spalazzi, J. P., J. Gallina, S. D. Fung-Kee-Fung, E. E. Konofagou, and H. H. Lu. 2006. 'Elastographic imaging of strain distribution in the anterior cruciate ligament and at the ligament-bone insertions', *J Orthop Res*, 24: 2001-10.

Subramanian, A., and T. F. Schilling. 2015. 'Tendon development and musculoskeletal assembly: emerging roles for the extracellular matrix', *Development*, 142: 4191-204.

Sugimoto, Y., A. Takimoto, H. Akiyama, R. Kist, G. Scherer, T. Nakamura, Y. Hiraki, and C. Shukunami. 2013. 'Scx+/Sox9+ progenitors contribute to the establishment of the junction between cartilage and tendon/ligament', *Development*, 140: 2280-8.

Teuschl, A. H., M. van Griensven, and H. Redl. 2014. 'Sericin removal from raw Bombyx mori silk scaffolds of high hierarchical order', *Tissue Eng Part C Methods*, 20: 431-9.

Teuschl, A., P. Heimel, S. Nurnberger, M. van Griensven, H. Redl, and T. Nau. 2016. 'A Novel Silk Fiber-Based Scaffold for Regeneration of the Anterior Cruciate Ligament: Histological Results From a Study in Sheep', *Am J Sports Med*, 44: 1547-57.

Thomopoulos, S., H. M. Kim, S. Y. Rothermich, C. Biederstadt, R. Das, and L. M. Galatz. 2007. 'Decreased muscle loading delays maturation of the tendon enthesis during postnatal development', *J Orthop Res*, 25: 1154-63.

Thomopoulos, S., G. R. Williams, J. A. Gimbel, M. Favata, and L. J. Soslowsky. 2003. 'Variation of biomechanical, structural, and compositional properties along the tendon to bone insertion site', *J Orthop Res*, 21: 413-9.

Thompson, E. M., A. Matsiko, E. Farrell, D. J. Kelly, and F. J. O'Brien. 2015. 'Recapitulating endochondral ossification: a promising route to in vivo bone regeneration', *J Tissue Eng Regen Med*, 9: 889-902.

van Donkelaar, C. C., and R. Huiskes. 2007. 'The PTHrP-Ihh feedback loop in the embryonic growth plate allows PTHrP to control hypertrophy and Ihh to regulate proliferation', *Biomech Model Mechanobiol*, 6: 55-62.

Vepari, C., and D. L. Kaplan. 2007. 'Silk as a Biomaterial', *Prog Polym Sci*, 32: 991-1007.

Wang, I. E., J. Shan, R. Choi, S. Oh, C. K. Kepler, F. H. Chen, and H. H. Lu. 2007. 'Role of osteoblast-fibroblast interactions in the formation of the ligament-to-bone interface', *J Orthop Res*, 25: 1609-20.

Wang, X., E. Wenk, X. Zhang, L. Meinel, G. Vunjak-Novakovic, and D. L. Kaplan. 2009. 'Growth factor gradients via microsphere delivery in biopolymer scaffolds for osteochondral tissue engineering', *J Control Release*, 134: 81-90.

Weiss, S., T. Hennig, R. Bock, E. Steck, and W. Richter. 2010. 'Impact of growth factors and PTHrP on early and late chondrogenic differentiation of human mesenchymal stem cells', *J Cell Physiol*, 223: 84-93.

Wenk, E., H. P. Merkle, and L. Meinel. 2011. 'Silk fibroin as a vehicle for drug delivery applications', *J Control Release*, 150: 128-41.

Woodfield, T. B., C. A. Van Blitterswijk, J. De Wijn, T. J. Sims, A. P. Hollander, and J. Riesle. 2005. 'Polymer scaffolds fabricated with pore-size gradients as a model for studying the zonal organization within tissue-engineered cartilage constructs', *Tissue Eng*, 11: 1297-311.

Wren, T. A., S. A. Yerby, G. S. Beaupre, and D. R. Carter. 2001. 'Mechanical properties of the human achilles tendon', *Clin Biomech (Bristol, Avon)*, 16: 245-51.

Xie, J., X. Li, J. Lipner, C. N. Manning, A. G. Schwartz, S. Thomopoulos, and Y. Xia. 2010. '"Aligned-to-random" nanofiber scaffolds for mimicking the structure of the tendon-to-bone insertion site', *Nanoscale*, 2: 923-6.

Xie, X. H., X. L. Wang, G. Zhang, Y. X. He, Y. Leng, T. T. Tang, X. Pan, and L. Qin. 2015. 'Biofabrication of a PLGA-TCP-based porous bioactive bone substitute with sustained release of icaritin', *J Tissue Eng Regen Med*, 9: 961-72.

Xu, K., L. A. Kuntz, P. Foehr, K. Kuempel, A. Wagner, J. Tuebel, C. V. Deimling, and R. H. Burgkart. 2017. 'Efficient decellularization for tissue engineering of the tendon-bone interface with preservation of biomechanics', *PLoS One*, 12: e0171577.

Xu, X., A. K. Jha, R. L. Duncan, and X. Jia. 2011. 'Heparin-decorated, hyaluronic acid-based hydrogel particles for the controlled release of bone morphogenetic protein 2', *Acta Biomater*, 7: 3050-9.

Yang, P. J., and J. S. Temenoff. 2009. 'Engineering orthopedic tissue interfaces', *Tissue Eng Part B Rev*, 15: 127-41.

Yilgor, P., K. Tuzlakoglu, R. L. Reis, N. Hasirci, and V. Hasirci. 2009. 'Incorporation of a sequential BMP-2/BMP-7 delivery system into chitosan-based scaffolds for bone tissue engineering', *Biomaterials*, 30: 3551-9.

Yin, F., J. Cai, W. Zen, Y. Wei, W. Zhou, F. Yuan, S. R. Singh, and Y. Wei. 2015. 'Cartilage Regeneration of Adipose-Derived Stem Cells in the TGF-beta1-Immobilized PLGA-Gelatin Scaffold', *Stem Cell Rev*, 11: 453-9.

Younesi, M., D.M. Knapik, J. Cumsky, B. Ozgur Donmez, P. He, A. Islam, G. Learn, P. McClellan, M. Bohl, R. J. Gillespie, and O. Akkus. 2017. 'Effects of PDGF-BB delivery from heparinized collagen sutures on the healing of lacerated chicken flexor tendon in vivo', *Acta Biomater*, 63: 200-09.

Zelzer, E., E. Blitz, M. L. Killian, and S. Thomopoulos. 2014. 'Tendon-to-bone attachment: from development to maturity', *Birth Defects Res C Embryo Today*, 102: 101-12.

Zhu, Y., T. Liu, K. Song, X. Fan, X. Ma, and Z. Cui. 2008. 'Adipose-derived stem cell: a better stem cell than BMSC', *Cell Biochem Funct*, 26: 664-75.

Zieris, A., K. Chwalek, S. Prokoph, K. R. Leventhal, P. B. Welzel, U. Freudenberg, and C. Werner. 2011. 'Dual independent delivery of pro-angiogenic growth factors from starPEG-heparin hydrogels', *Journal of Controlled Release*, 156: 28-36.

7 APPENDIX

7.1 List of figures

Figure 1. Schematic representation of fibrocartilaginous tendon/ligament-to-bone interfaces

Figure 2. Role of transforming growth factor beta II (TGF-βII) receptor, bone morphogenetic protein 4 (BMP4) and scx+/SRY(sex-determining region Y)-box 9 (sox9)+ fibrochondrocyte progenitors on enthesis development.

Figure 3. Silk fibroin extraction and processing.

Figure 4. Fabrication of anisotropic silk fibroin scaffolds

Figure 5. Fabrication of isotropic silk fibroin scaffolds

Figure 6. Fabrication of biphasic silk fibroin scaffolds

Figure 7. Mechanical testing setup

Figure 8. qPCR run protocol

Figure 9. Effect of freezing temperature and silk fibroin solution concentration on the pore sizes of anisotropic scaffolds.

Figure 10. Characterization of silk fibroin anisotropic and isotropic scaffolds.

Figure 11. Morphology of biphasic scaffolds.

Figure 12. Characterization of biphasic scaffolds.

Figure 13. Porosity and pore size distribution of biphasic silk fibroin scaffolds.

Figure 14. Flow rate and permeability of anisotropic and biphasic scaffolds.

Figure 15. Tensile testing of anisotropic and biphasic scaffolds.

Figure 16. Cytotoxicity/viability and proliferation of AdMSCs on biphasic scaffolds.

Figure 17. Morphology and cytoskeletal alignment of AdMSCs on biphasic scaffolds.

Figure 18. AdMSCs gene expression on biphasic scaffolds.

Figure 19. Heparin incorporation and release on type B biphasic scaffolds.

Figure 20. TGF-β2 and GDF5 incorporation and release on type B biphasic scaffolds. A), C)

Figure 21. AdMSCs seeding efficiency and metabolic activity on heparin-functionalized and non-functionalized type B biphasic scaffolds.

Figure 22. Gene expression of tendon/ligament, enthesis and cartilage markers on heparin-functionalized type B biphasic scaffolds.

Figure 23. AdMSCs cytoskeletal alignment and collagen I protein content on heparin-functionalized type B biphasic scaffolds.

Figure 24. AdMSCs cytoskeletal alignment and collagen II protein content on heparin-functionalized type B biphasic scaffolds.

Figure 25. AdMSCs cytoskeletal alignment and collagen III protein content on heparin-functionalized type B biphasic scaffolds.

7.2 List of tables

Table 1. Primers used for qPCR.

7.3 List of publications

- Font Tellado S, Chiera S, Bonani W, Poh P. S. P, Migliaresi C, Motta A, Balmayor E.R, van Griensven M. Heparin functionalization increases retention of TGF-β2 and GDF5 on biphasic silk fibroin scaffolds for tendon/ligament-to-bone tissue engineering. Acta Biomater. 2018 May;72:150-166

- Font Tellado S, Bonani W, Balmayor ER, Foehr P, Motta A, Migliaresi C, van Griensven M. Fabrication and characterization of biphasic silk fibroin scaffolds for tendon/ligament-to-bone tissue engineering. Tissue Eng Part A. 2017 Aug;23(15-16):859-872.

- Balmayor ER, Font Tellado S, van Griensven M. MicroRNA-Biomaterial systems in Bone Repair. In book: Comprehensive Biomaterials II, Edition: 2nd, Chapter: 83, Publisher: Elsevier, Editors: Paul Ducheyne, Kevin Healy, Dietmar W. Hutmacher, David W. Grainger, James Kirkpatrick

- Font Tellado S, Balmayor ER, van Griensven M. Strategies to engineer tendon/ligament-to-bone interface: Biomaterials, cells and growth factors. Adv Drug Deliv Rev. 2015 Nov 1;94:126-40

7.4 Permission to include published work in the PhD thesis

8 ACKNOWLEDGEMENTS